Cognitive RF Front-end Control

Eyosias Yoseph Imana

Dissertation submitted to the faculty of

Virginia Polytechnic Institute and State University

in the partial fulfillment of the requirements for the degree of

Doctor of Philosophy

In

Electrical Engineering

Jeffery H. Reed, Chair

Robert W. McGwier

Peter M. Athanas

Kwang-Jin Koh

Barbara M.P. Fraticelli

November 21, 2014

Blacksburg, Virginia

Keywords: Cognitive radio, spectrum sensing, receiver non-linearity

Cognitive RF Front-end Control

Eyosias Yoseph Imana

Abstract

This research addresses the performance degradation in receivers due to poor selectivity. Poor selectivity is expected to be a primary limitation on the performance of Dynamic-Spectrum-Access (DSA) and millimeter wave (mmWave) technologies. Both DSA and mmWave are highly desired technologies because they can address the spectrum-deficit problem that is currently challenging the wireless industry. Accordingly, addressing poor receiver selectivity is necessary to expedite the adoption of these technologies into the main street of wireless. This research develops two receiver design concepts to enhance the performance of poorly-selective receivers.

The first concept is called cognitive RF front-end control (CogRF). CogRF operates by cognitively controlling the local-oscillator and sampling frequencies in receivers. This research shows that CogRF can fulfil the objective of pre-selectors by minimizing the effects of weak and moderately-powered neighboring-channel signals on the desired signal. This research shows that CogRF can be an alternative to high-performance pre-selectors, and hence, CogRF is a viable architecture to implement reliable DSA and mmWave receivers. The theoretical design and hardware implementation of a cognitive engine and a spectrum sensor of CogRF are reported in this dissertation. Measurement results show that CogRF significantly reduces the rate of communication outage due to interference from

neighboring-channel signals in poorly-selective receivers. The results also indicate that CogRF can enable a poorly-selective receiver to behave like a highly-selective receiver.

The second receiver design concept addresses very strong neighboring-channel signals. The performance of poorly selective receivers can easily suffer due to a strong, unfiltered neighboring-channel signal. A strong neighboring-channel signal is likely for a DSA radio that is operating in military radar bands. Traditionally, strong neighboring signals are addressed using an Automatic-Gain-Control (AGC) that attempt to accommodate the strong received signal into the dynamic range of the receiver. However, this technique potentially desensitizes the receiver because it sacrifices the Signal-to-Noise-Ratio (SNR) of the desired signal. This research proposes the use of auxiliary-receive path to address strong neighboring-channel signals with minimal penalty on the SNR of the desired signal. Through simulation based analysis, and hardware-based measurement, this research shows that the proposed technique can provide significant improvement in the neighboring-channel-interference handling capability of the receiver.

To :

My parents, Mami and Babi,

My brothers, Geme and Amuti

My sister, Tutu

and

My soon-to-be wife, Kiya.

May God bless you for being a blessing to me!!!

Acknowledgment

By the help of God, here I am placing one more milestone of this life. And, this is how I sum it up - God is truly faithful. It was nine years ago when He promised to educate me in the best wireless program. He has faithfully followed through His promise. Thank you, Lord. All is by you, and all is for you.

I am so grateful for the opportunity of doing my Ph.D. under the supervision of Dr. Reed. I want to thank him for taking me as his student, and for all the opportunities he created for me during my stay at Virginia Tech. I thank him for carefully reading my papers and scrutinizing them in detail. It was a privilege to listen to and learn from Dr.Reed's insightful comments during our weekly students' meeting. Thank you so much.

I also want to thank Dr. Yang for being my mentor. Thank you so much for pressing me to become a better engineer and scholar. Dr. Yang taught me how to write, and how to think. And I know those lessons will be valuable for me throughout my career. Thank you so much.

If I now know anything about RF, I learned it from Randall. I want to thank Randall for relentlessly sharing his expertise and his ideas with me. This dissertation would be much more difficult without Randall's help. Thank you so much.

I also want to thank my Ph.D. committee members; Dr. McGwier, Dr. Athanas, Dr. Koh and Dr. Fraticelli for their interest in my work, and the valuable comments I have been receiving from them. Thank you so much.

Table of Contents

List of Figures

List of Tables

Abbreviations

ADC: Analog-to-digital convertor

AGC: Automatic gain control

AI: Artificial intelligence

API: Application programming interface

APA-DC: Auxiliary-path assisted digital correction

APA-SD: Auxiliary-path assisted soft-decoding

BER: Bit-error rate

BPSK: Binary phase shift keying

BST: Barium-Strontium-Titanate

CE: Cognitive engine

CogRF: Cognitive RF front-end

CMOS: Complementary metal-oxide-semiconductor

CRC: Cyclic redundancy check

CS: Channelized spectrum

CSR: Channelized spectrum representation

DAC: Digital-to-analog convertor

DC: Direct current

DMA: Direct memory access

DSA: Dynamic spectrum access

DSP: Digital-signal processor/processing

FDD: Frequency domain duplexing

FFT: Fast Fourier transform

FPGA: Field-programmable gate array

GPS: Global positioning system

IF: Intermediate frequency

IIP3: Third-order input intercept point

IIP2: Second-order input intercept point

IoT: Internet-of-Things

IRR: Image rejection ratio

LNA: Low-noise amplifier

LO: Local oscillator

MAC: Medium access control

MEMS: Microelectromechanical sensors

mmWave: Millimeter wave

MSS: Multiband spectrum sensing

PCIe: Peripheral component interconnect-Express

PSD: Power spectral density

QPSK: Quadrature-phased shift keying

QAM: Quadrature amplitude modulation

RS-MSS: Robust serial multiband spectrum sensing

RF: Radio frequency

RFIC: Radio frequency integrated circuit

RX: Receiver

S-MSS: Serial multiband spectrum sensing

SAW: Surface acoustic wave

SNR: Signal-to-noise ratio

TDD: Time domain duplexing

TX: Transmitter

Chapter 1

Introduction

1.1 Motivation

The popularity of smart-phones and tablets lead to an exponential increase in demand for wireless services [1]. However, the increase in demand has not been matched by increase in spectrum for commercial wireless systems. This has resulted in what the Federal Communication Corporation (FCC) calls the "spectrum deficit" [2]. To address this challenge, different technologies are under consideration. Two of these technologies are the Dynamic Spectrum Access (DSA) and Millimeter Wave (mmWave) technologies.

DSA technology addresses the spectrum deficit problem by allowing shared use of spectrum [3, 4]. In DSA, unlicensed secondary users (SUs) can operate in a frequency band if the licensed primary user (PU) is not using the band. Hence, DSA is contrary to the traditional fixed-allocation scheme that leads to spectrum underutilization [5-7].

The other alternative is the use of mmWave bands for cellular applications. Particularly, the 28 GHz, 38 GHz and 60 GHz bands are being considered for use in urban environments [8, 9]. These frequency bands have not been favored for cellular applications because of undesirable propagation properties. The wireless industry is now attracted to mmWaves due to the abundance of spectrum in those frequency bands, and because lower-frequency bands are already crowded.

Therefore, the DSA and the mmWave technologies are promising for addressing the current spectrum deficit problem. It can be noted that the performances of both of these technologies are likely to be limited by poor receiver selectivity because they are expected to employ poorly-selective receivers.

A DSA radio is likely to use tunable pre-selectors because it has to be operational over multiple frequency bands. As shown in Section 1.4.1, the selectivity of tunable filters is often very low compared to that of fixed filters. Hence, poor receiver selectivity can be expected to be the norm of DSA radios [10]. On the other hand, mmWave radios may not be using tunable filters. However, selectivity levels that would be considered to be good in lower frequency bands easily become unsatisfactory at mmWave range due to frequency scaling. For example, a loaded-Q = 100 filter, which is considered to be very good filter in lower frequency bands, has a 300 MHz reception bandwidth at 30 GHz frequency. However, the signal bandwidth in cellular systems is typically less than

20 MHz. Hence, the reception bandwidth of mmWave radios is expected to be much larger compared to the signal bandwidth. The other alternative is expanding the signal bandwidth by an order of magnitude for mmWave-based wireless standards. However, such approach leads to significant increase in the power consumption of the analog-to-digital converter of the receiver.

In summary, both DSA and mmWave are expected to suffer from poor receiver selectivity. Considering the future potential of these technologies, it is timely and important to develop a suitable architecture that can enhance the performance of poorly-selective receivers. This research develops a new receiver architecture called *Cognitive RF front-end* (CogRF) to enhance the performance of poorly-selective receivers by using intelligent control over RF front-end parameters.

The problems in poorly-selective receivers, and the solutions that are developed in this research are discussed in the following sections.

1.2 Problems of Poorly-Selective Receivers

Figure 1.1 shows the block diagram of a traditional direct-conversion receiver [11, 12]. After the signal is captured by the antenna, the pre-selector filter passes only the section of the input spectrum that contains the desired signal, and it attenuates the rest of the spectrum. The next element is the low-noise amplifier (LNA). The LNA ideally amplifies the signal with minimal addition of noise. After the LNA, the signal is supplied to the mixer where it is multiplied by a periodic signal at frequency f_{LO} originating from a local oscillator (LO). The multiplication process in the mixer shifts the frequency of the received signal down to very low frequency ranges. The multiplication process in the mixer

produces other undesired signals in addition to the frequency shifted version of the received signal. A low-pass filter is placed after the mixer to reject some of the mixer's undesired outputs. Then, the signal is digitized by the analog-to-digital-convertor (ADC) at sampling-rate f_s and is processed in a (DSP based) modem. The low-pass filter after the mixer also serves as anti-aliasing filter for the ADC.

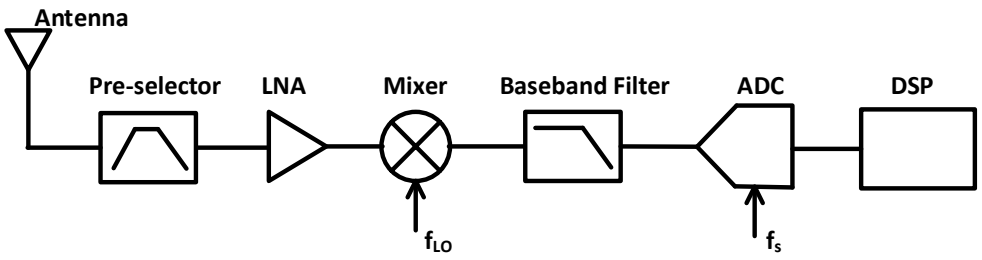

Figure 1.1 Traditional receiver RF front-end architecture.

A poorly-selective receiver is hereby defined as a receiver whose reception bandwidth is much greater than the desired signal's bandwidth. The term "reception bandwidth" basically denotes the bandwidth of the pre-selector filter. Figure 1.2 shows the frequency characteristics of a poorly-selective receiver that is passing in multiple neighboring-channel signals along with the desired signal. In contrast, the reception bandwidth of a highly-selective (or simply a selective) receiver is comparable to the signal bandwidth. That means, a highly-selective receiver lets only the desired signal into the receiver and rejects neighboring-channel signals.

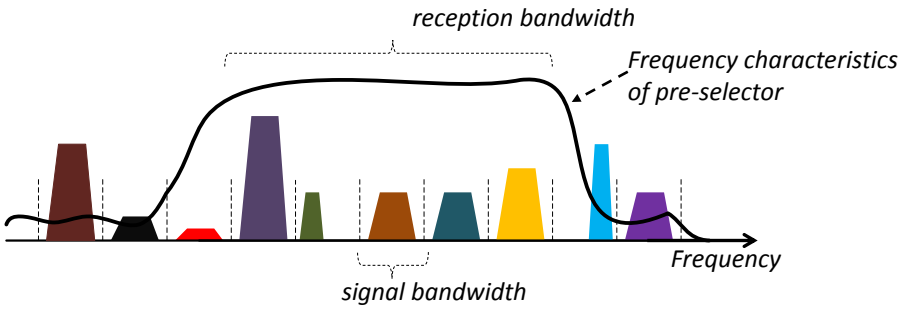

Figure 1.2 Illustration of an example poorly-selective receiver.

The pre-selector filter defines the selectivity of the receiver. Through the effects of non-linearity, IQ imbalance and aliasing, neighboring-channel signals that are not rejected at the pre-selector can desensitize the receiver to the desired signal [12, 13]. As shown in Figure 1.3, these effects re-distribute the energy of the overall received signal after it enters the receiver. Thus, a signal which is originally received at a neighboring-channel can actually become a co-channel interferer after entering the receiver. Therefore, the desired signal is subject to higher level of interference in poorly-selective receivers.

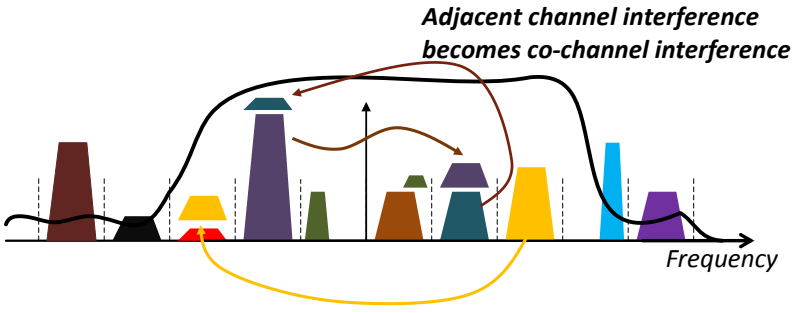

Figure 1.3 Energy is re-distributed inside the receiver due to receiver impairments.

However, the “energy re-distribution” in the receiver is not completely random - it is actually controllable. As it will be detailed in the next section, the LO and sampling frequency in the receiver determine the band in which image and aliased signals appear during down-conversion and sampling. Therefore, one can minimize the level of interference in the desired band by adaptively adjusting the LO and sampling frequencies based on the frequency location of neighboring-channel signals. This mechanism improves the sensitivity of the poorly-selective receivers because it minimizes the effects of unfiltered neighboring-channel signals on the desired signal.

1.3 Obtaining Receiver Selectivity using CogRF

1.3.1 CogRF Concept

As it is asserted in the previous section, energy re-distribution in poorly selective receivers can be restrained by intelligently controlling the LO and sampling frequencies. This research shows that the sensitivity of a poorly-selective receiver can be greatly improved by cognitively controlling the Local Oscillator (LO) and sampling frequencies of the receiver. *In this dissertation, a receiver whose LO and sampling frequencies are controlled by artificial intelligence is referred as CogRF*. This research shows that CogRF improves the tolerance to neighboring-channel interference in poorly-selective receivers. CogRF also allows receivers to be cheaper by reducing the need for high-performance analog components.

The conceptual diagram of CogRF is shown in Figure 1.4. It is shown that CogRF contains three major elements. These are the cognitive engine, the spectrum sensor and the receiver RF front-end. These are briefly described below.

Cognitive engine: The cognitive engine is the brain of CogRF. The artificial intelligence algorithms that establish the "cognitive-ness" of CogRF are housed in the cognitive engine. The cognitive engine selects the LO and sampling frequencies (or the frequency-plan[1]) of the receiver RF front-end based on the power level of neighboring-channel signals.

Spectrum sensor: CogRF incorporates spectrum sensing to measure the occupancy of the received spectrum at the input of the receiver. The output of the spectrum sensing is used by the cognitive engine to make informed decisions. The cognitive engine selects the LO and sampling frequencies that minimize the interference caused by neighboring channel signals on the desired signal.

Receiver RF front-end: After making a decision, the cognitive engine configures the LO and sampling frequencies of the receiver RF front-end. The cognitive engine applies the spectrum sensing data on mathematical models of the RF front-end to predict the level of interference on the desired signal, and determine whether a candidate RF front-end setting "works" or not. For this purpose, the cognitive engine contains a repository of mathematical models representing the RF front-end at different settings.

[1] The phrase "frequency-plan" is used to collectively refer to the LO and sampling frequency

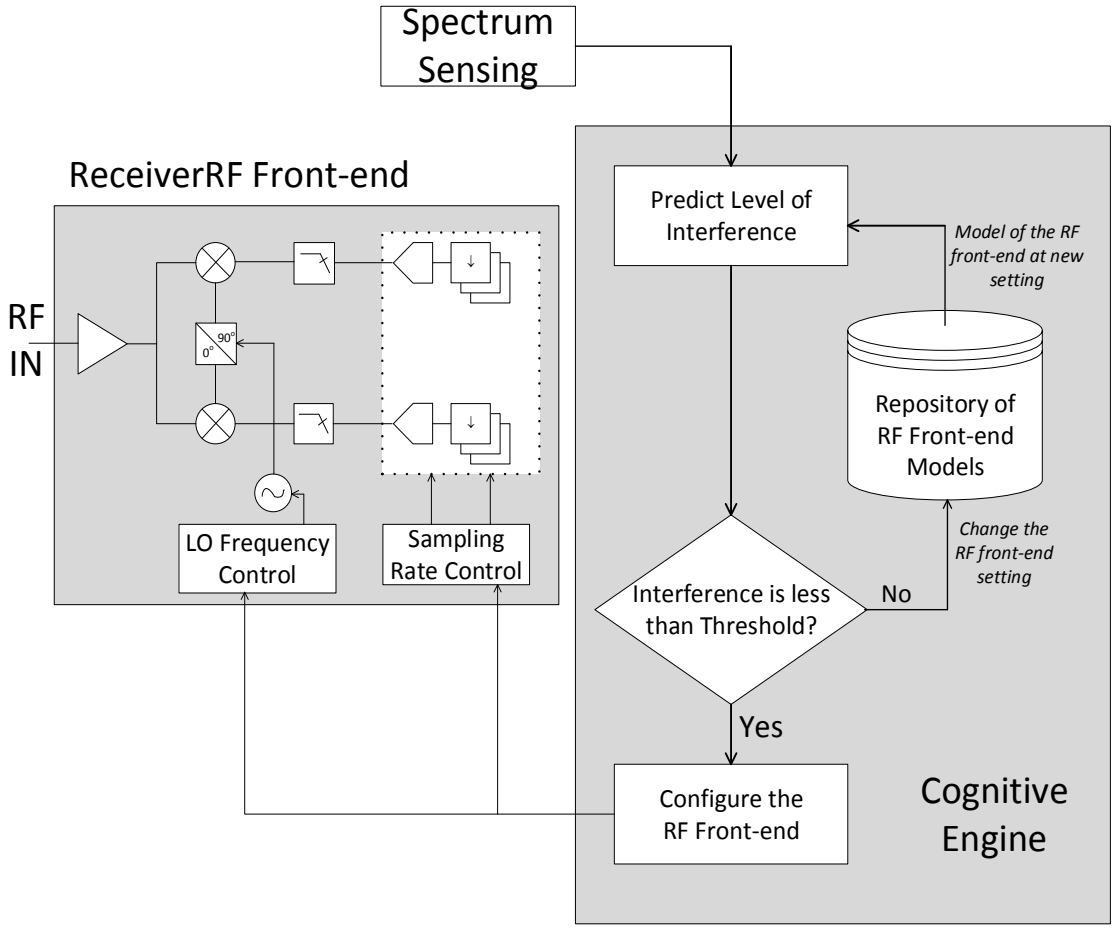

Figure 1.4 Conceptual block diagram of CogRF.

1.3.2 Obtaining Receiver Selectivity without using Pre-selectors

This section describes how CogRF can restrain the energy re-distribution process in receiver RF front-ends. The description illustrates that CogRF can fulfill the objectives of pre-selectors by diminishing the effects of neighboring-channel signals on the desired signal. Based on this claim, it is argued that CogRF is a viable alternative to a sophisticated pre-selector-based receiver architecture. Subsequent chapters provide a rigorous analysis of the technique.

Figure 1.5 shows the spectrum of a signal at different stages of a receiver. At the receiver input, the spectrum contains two signals (shown as orange and red bars). Assume the receiver does not contain a pre-selector for now. After the two signals enter the LNA, its non-linearity causes the signals to produce inter-modulation products [11, 12]. Then, the signals enter a complex mixer that is assumed to contain imaginary and real paths. Because of the IQ imbalance between the real and imaginary paths of the receiver, the input signals are mirrored in the mixer. The signals appear with their images at the output of the mixer.

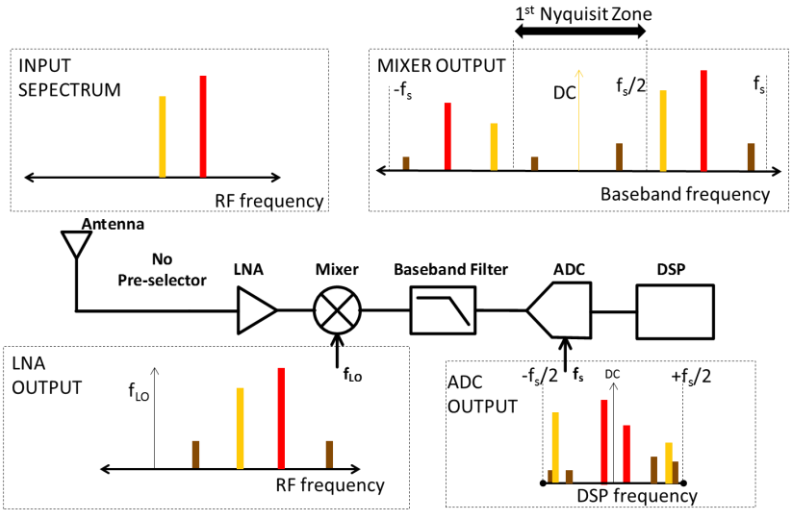

Figure 1.5 Received signals at different stages of the receiver in frequency domain (assuming there is no pre-selector filter).

The border of the ADC's first Nyquist zone is denoted by $f_s/2$ in the figure. At the input of the ADC, the first Nyquist zone contains only two signals. Hence, the other signals output from the mixer will first be attenuated by the anti-aliasing/baseband filter, and then alias into the first Nyquist zone during sampling in the ADC.

Due to energy re-distribution inside the receiver, a spectrum that appears to be sparsely occupied at the receiver input becomes very crowded at the ADC output. In Figure 1.6, the desired signal represented by a blue triangle. Even though the signal does not contain interference at the input spectrum, it has interference at the output of the ADC. Neighboring-channel signals appear as co-channel interferers after they enter into the receiver.

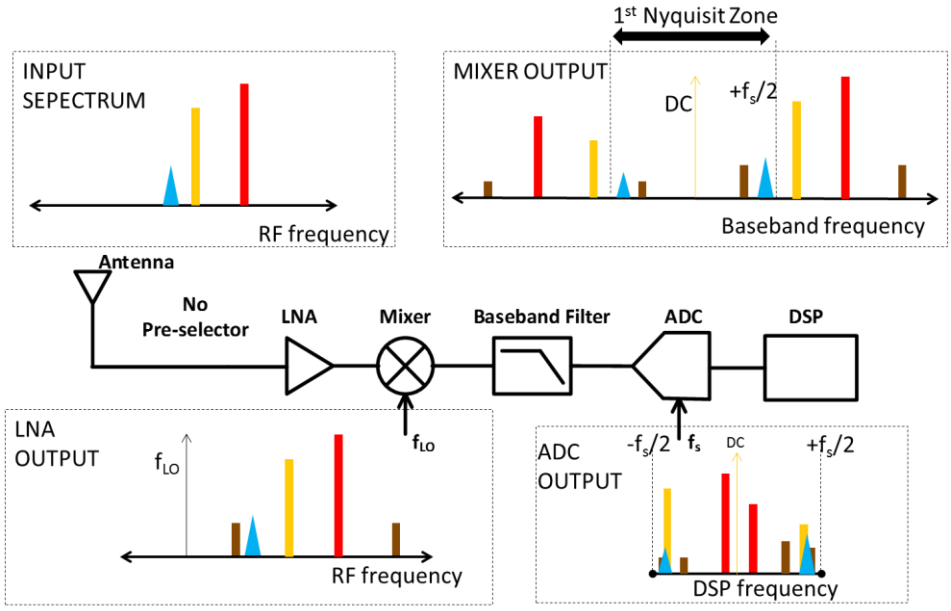

Figure 1.6 Frequency domain of the received signal at different stages in the receiver with a desired signal (assuming there is no pre-selector filter).

Pre-selector minimizes the effects of the energy re-distribution in the receiver. As shown in Figure 1.7, a pre-selector filter is often used to attenuate neighboring-channel signals and diminish their effect on the desired signal. The pre-selector filter allowed the desired signal to reach the output of the ADC with minimal interference.

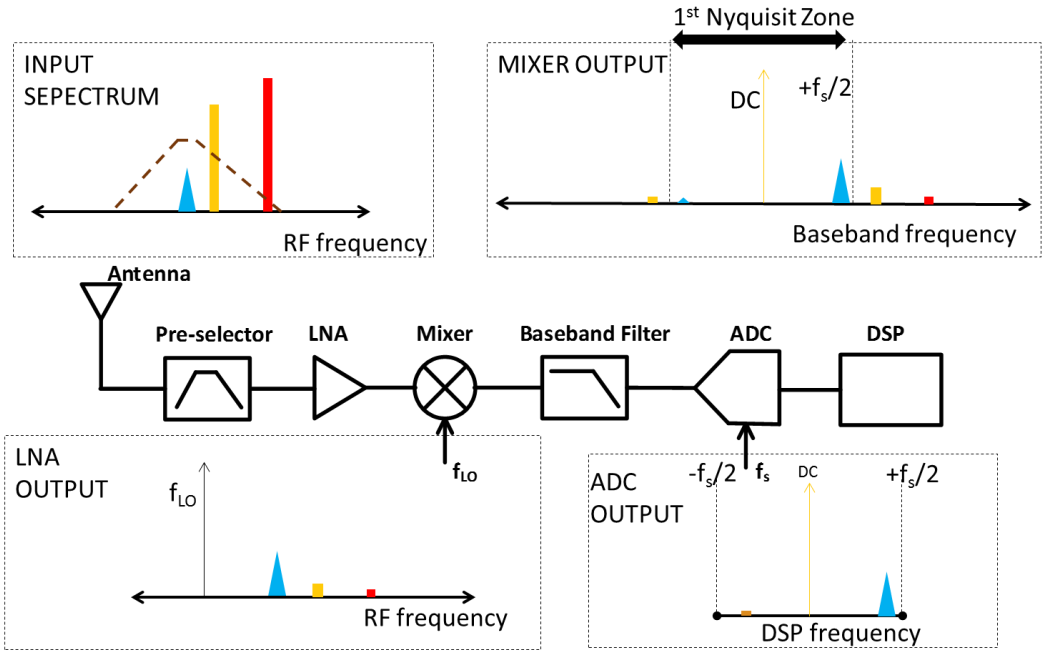

Figure 1.7 Using pre-selectors to minimize the effects of energy re-distribution.

The energy re-distribution challenge is inevitable without a sufficiently selective pre-selector inside a receiver. As discussed in Section 1.1, DSA and mmWave are examples where filter technology is not advanced enough to provide low-cost selective pre-selectors. Since DSA and mmWave are expected to be integral part of the future wireless industry, it is becoming apparent that there is a need for a receiver architecture that is not reliant on expensive pre-selectors filters to obtain selectivity.

This research asserts that CogRF can be an alternative to pre-selectors. It can be noted that the energy re-distribution inside a receiver can be restrained through the LO and sampling frequencies of the receiver. Therefore, it is possible to position the neighboring-channel signals and their artifacts away from the desired signal during down-conversion and sampling. In this manner, one can obtain a clean

desired signal at the output of the ADC, and improve the sensitivity of the receiver.

Figure 1.8 can be compared with Figure 1.7 to illustrate the CogRF mechanism. Even though the input spectrum is the same in Figure 1.8 and Figure 1.7, the spectrums at the output of the ADCs are different in the two figures. This is because different sampling rates are used in the two figures. The sampling-rate used in Figure 1.8 places the desired signal away from potential interferences. After sampling, a highly-selective DSP filter is used to extract the desired signal.

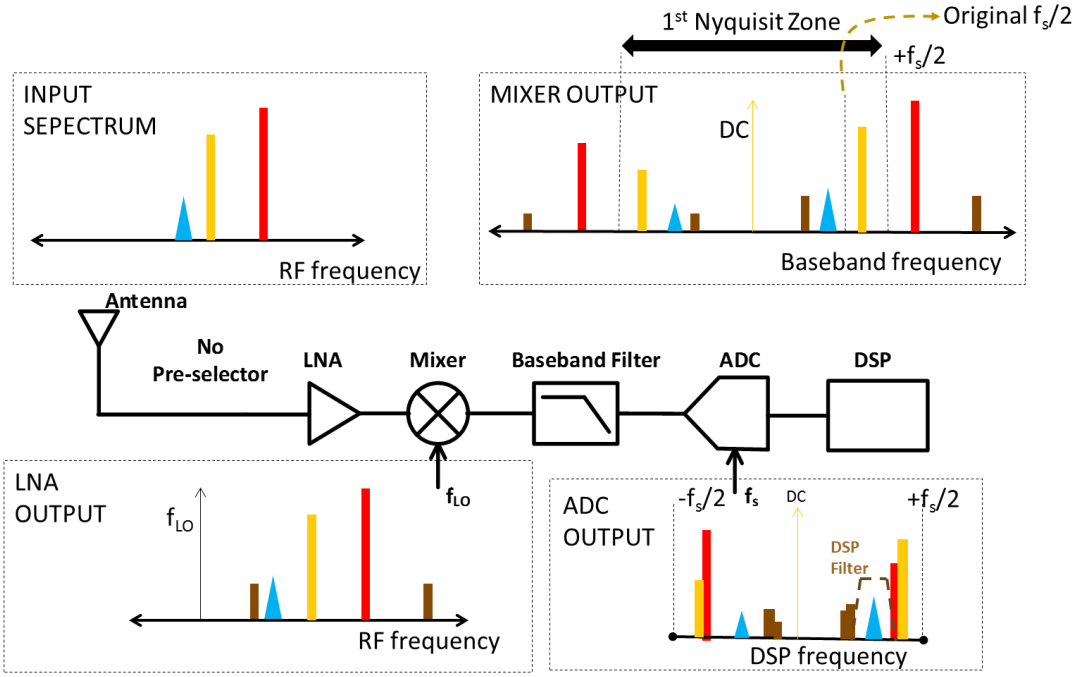

Figure 1.8 Cognitive adjustment of the sampling rate can protect the desired signal from interference in poorly selective receivers.

By transforming an RF pre-selector problem to a DSP problem, CogRF enables a poorly-selective receiver to behave similar to highly-selective receiver. Hence, it is highly desirable to implement CogRF within poorly-selective receivers that are

found in DSA and mmWave radio systems. In addition, CogRF can be used to simply reduce the cost of an RF front-end by allowing a reliable operation using cheaper (and less selective) pre-selectors in any receiver. During receiver design, CogRF can also be used to relax the image-rejection and selectivity requirements of the mixer and baseband filters, respectively.

1.4 Related Works and Current Practices

The impact of this research relates to addressing the poor selectivity problem in DSA and mmWave radio receivers. This section reviews related works that attempt to address the same problem. Furthermore, this section also discusses existing adaptive RF front-end control mechanism and outlines the differentiation of CogRF.

1.4.1 Selectivity of Frequency-Flexible Receivers

The benefits of DSA technology cannot be fully appreciated without using flexible radios. However, small-sized RF front-end cannot be both frequency-flexible and selective at the same time [14].

Frequency-flexible RF front-ends could be built by using array of single-band pre-selector filters. However, such architecture can quickly become too complex as the number of supported frequency bands increases. For example, the recently introduced Qualcomm RF360^{TM} chip can support up to 40 bands in the same chip using 3D-packaging of SAW filters [15], but the chip still requires separate pre-selector for each band.

The other alternative is the use of tunable filters. There are various types of tunable RF filter technologies. The most common ones are highlighted in this classic paper [16]. Generally, tunable filters can be categorized as, mechanically tunable, magnetically tunable and electronically tunable filters. Mechanically tunable filters change their characteristics by changing their physical structure. The bulkiness and slow tuning speed of mechanically tunable filters makes them inapplicable for handheld mobile radios. The YIG filter technology is a prime example of magnetically tuned filters [16]. YIG filters are known to give multi-octave tuning range and low-percentage bandwidth [16]. They are used in testing equipment such as spectrum analyzers. However, their power consumption is significantly greater than that of electronically tunable filters [17]. YIG filters also have relatively large size and weight. These characteristics make YIG filters unfavorable for handheld radio applications.

The remaining choice is the use of electronically tunable filters. They generally have smaller tuning range and lower quality factor compared to mechanically and magnetically tunable filters [16]. Their easiness for monolithic integration makes them favorable for handheld radio applications.

There are three prevalent technologies that are used to build electronically tunable filters. These are semiconductor technology, Barium-Strontium-Titanate (BST) and microelectromechanical systems (MEMS). Table 2.1 presents a sample of recently published electronically tunable filters operating between 100 MHz and 6 GHz - the frequency range in which most commercial and public safety wireless services operate. Most of the listed filters have relatively small size and a tuning range of about one octave. Therefore, it can be stated that electronically tunable filter technology is already capable of achieving high tuning range using small-sized filters. The major pitfall of electronically tunable filters is their poor

selectivity. For example, the percentage bandwidth of fixed SAW filters can easily be made less than 5 % [18], while for the tunable filters listed in Table 1.1 the bandwidth is more than 20%, on average. MEMS technology is the most promising for fabricating selective and tunable pre-selector filters. It is projected that the unloaded quality factor of this technology is going double in the next decade [19]. Even if MEMS selectivity improves, however, MEMS technology still suffers from other limitations such as poor power handling capability [19].

Table 1.1. Sample tunable pre-selector filters.

Reference	Technology	Frequency Range (GHz)	10 dB Bandwidth[2] (%)	Size (cm^2)
[20]	BST	0.49 – 0.79	≈ 40	≈20
[21]	BST	0.18 – 0.28	≈ 50	≈15
[22]	BST	0.23 – 0.40	≈ 25	≈ 2
[23]	Semiconductor	0.70 – 1.33	≈ 30	≈10
[24]	MEMS	1.50 - 2.50	≈ 12	≈0.5
[25]	Semiconductor	0.50 – 0.90	≈ 28	0.16
[26]	Semiconductor	1.40 – 2.00	≈ 10	0.64
[27]	MEMS	3.55 – 4.71	≈ 3	≈8
[28]	MEMS	4.30 – 5.50	≈ 10	1.0
[29]	MEMS	0.70 – 2.26	≈ 50	0.6
[30]	MEMS	1.50 – 2.50	≈ 20	0.7
[30]	MEMS	2.60 - 3.60	≈ 15	0.7
[30]	MEMS	3.70 - 5.40	≈ 15	1.2
[31]	Semiconductor	0.95 – 1.48	≈ 13	1.87

In summary, it is likely that tunable RF front-ends will remain poorly-selective for foreseeable future. This assertion is also implied in [32].

[2] The term "10 dB bandwidth" refers to the pass-band bandwidth of the filter in which the insertion-loss is less than 10 dB.

Non-conventional methods have also been proposed to address poor selectivity in DSA receivers. Marshal [33, 34] proposed a network level technique in which transmission frequencies are selected such that the expected non-linearity distortion in the receiver is minimized. Marshal showed that this technique has a potential of relaxing the selectivity and linearity specifications of the receiver. However, because Marshal's technique relies on dynamic adjustments of transmission frequencies, it is applicable only in DSA based networks. In contrast, CogRF relies on controlling receiver parameters, and thus, it can be applied both to DSA and non-DSA based wireless networks.

Similar to Marshall's approach [33, 34], this research address poor selectivity by relaxing the selectivity requirement of receivers. This is in contrast to an approach that attempts to improve the actual selectivity of receivers. One potential benefit of CogRF is that it can expedite their adoption into commercial radios by relaxing the selectivity requirement of receivers. This is because CogRF enhances the performances of existing, poorly-selective tunable pre-selectors and allows them to behave like highly-selective receivers. In multi-band filters based flexible receivers like Qualcomm RF360, CogRF can be used to reduce the number of integrated filters. This reduces the cost, and size of the RF front-end. It may also reduce the insertion-loss of the RF front-end by reducing the complexity of the switching network of the filters.

1.4.2 Selectivity of mmWave Filters

Examples of miniaturized mmWave filters are presented in [35, 36]. Even though percentage bandwidth of these filters is low, the actual bandwidth (> 300 MHz) is large compared to the signal bandwidth in typical cellular systems (< 20 MHz). The signal bandwidth can be increased in the standards to make it comparable to the reception bandwidth of mmWave receivers. However,

increasing the signal bandwidth requires the incorporation of high performance, and power-hungry ADCs in the receiver.

The other alternative is to relax the selectivity requirement of mmWave receivers. For example, Rappaport *et. al.* proposed the use of beamforming-assisted Time-Duplex-Multiple-Access (TDMA) to relax the selectivity requirement of mmWave receivers [9]. However, this technique is a network-level solution because it inherently requires the interaction between the receiver and the transmitter through a separate control link. The receiver architecture that is developed in this research also attempts to relax the selectivity requirement of receivers. However, because the proposed technique relies entirely on controlling local receiver parameters it does not need any network-level interactions and does not need to be standardized.

1.4.1 Past Work on Adaptive RF front-end control

Adaptive RF front-end control can be traced back to the inception of Automatic-Gain Control (AGC) systems in the early days of radio [37]. And recently, IMEC's researchers published a book on the topic of adaptive RF front-end control [38]. They reported design, implementation, and testing of adaptive antenna tuning and adaptive power amplifier control mechanisms. They used a directional-coupler to sense the mismatch between the antenna and the power amplifier; and a temperature sensor to measure the die-temperature of the power amplifier. By comparing the output of these sensors with a reference value, a feedback correction circuit adjusts the settings of the antenna matching circuit and the power amplifier. The major pitfall of such type of mechanisms is that control circuits are individualized to each RF front-end parameter. This approach is impractical when the number of controllable parameters is large.

In contrast, digital-based control mechanism is developed in this research. This mechanism can control large number of RF front-end parameters at the same time. Accordingly, the developed mechanism allows the controlled RF front-end to attain a globally optimal operational state.

There has been some research on digital-based control systems as well [39-44]. Most of these works have been focused on reducing the power consumption of the RF front-end using adaptive control. For example, Hueber *et. al.* in [44] and Tasic *et. al.* in [43] showed that significant amount of power can be saved by disabling some receiver features when adjacent-channel blocker is not present in the received spectrum. In contrast, the objective of the control mechanism in this research is maximizing the desired Signal-to-Interference (SIR) ratio at the output of the ADC. Furthermore, the control mechanism presented in this research involves not only adaptive features, but also cognitive features such as awareness, reasoning and learning.

1.5 A Note on Selectivity of Transmitters

RF filters are employed both in receivers and transmitters [45] (also see Figure 2.2). However, the focus of this research is only on issues related to poor-selective receiver RF filters. This is because poor selectivity is not as serious of an issue for transmitters as it is for receivers.

A transmitter is required to emit a desired spectral characteristics within the designated channel, and with minimal interference on other channels. The undesired transmissions on other channels can be due to spectral splattering caused by the power amplifier's non-linearity, the power amplifier's noise and

harmonics. However, off-channel emissions of the transmitter can be effectively addressed using techniques other than the use of selective RF filters.

Backing-off the power amplifier is a common technique that is used to reduce spectral splattering at the expense of the power amplifier's efficiency [46]. The power consumption penalty of backing-off can be reduced by applying digital peak-to-average-ratio-reduction [47] and pre-distortion techniques [48]. In other words, even if the transmitter is poorly-selective to reject off-band emissions, the interference level on neighboring channels can be adequately reduced by applying sufficient back-off at the power amplifier, and by pre-processing of the transmitted signal inside the modem.

Moreover, in poorly-selective transceivers, the noise generated by the power amplifier can easily desensitizes the receiver. This issue is detrimental in full-duplex systems where receiver and transmitters operate simultaneously. In poorly-selective receiver, the transmitter has to be muted in receive time-slots. For this reason, in DSA and mmWave systems, where poorly selective receivers and transmitters are expected, only half-duplex operation is likely to be standardized. Accordingly, half-duplex-based operation can relax the selectivity requirement of the transmitter. The receiver, however, can be desensitized by signals originating from other nearby transmitters in half-duplex-based networks as well (see Section 1.3.2). Hence, half-duplex-based-operation provides minimal level of improvement in terms of relaxing the selectivity requirement of receivers.

The other issue in poorly-selective transmitters relates to harmonics. Harmonics at the output of a transmitter are often due to the non-linearity of the power amplifier [46]. In half-duplex radios, rejecting the second or third harmonics may be the main purpose of the RF filter in the transmitter. Because harmonics are relatively far-off in frequency, a fixed low-pass RF filter may be sufficient to

reject harmonics - and such RF filter can be constructed using existing filter technologies.

In summary, poor selectivity is not a serious challenge for transmitters. Existing network and radio-level techniques are sufficient to address issues related to poor selectivity in transmitters. However, the same is not true for receivers. This research addresses this gap by developing a new receiver architecture for poorly-selective receivers.

1.6 Research Contributions

The contributions of this research are the following;

1. During the past decade, there have been several researches in the cognitive radio community studying the application of artificial intelligence to control radio parameters. However, artificial intelligence has been applied to control only the digital parameters of radios. Motivated by the advent of highly flexible and digitally-controllable analog RF front-ends, this research expands the scope of cognitive control into the analog realm of radios.

2. As shown in Figure 2.1, the CogRF framework contains the mathematical model of the RF front-end instead of the actual RF front-end within the decision-making cycle. It is argued in Section 3.1 that existing RF front-end models cannot be used in the proposed cognitive engine. This research develops a new receiver modeling technique called channelized spectrum representation (CSR) and uses it to design the cognitive engine in Chapter 4 and the spectrum sensing mechanism in Chapter 5. The theoretical

development of this model is presented in Chapter 3 and the practical validity of the model is verified using hardware experiments in Section 6.4.1 and 6.4.2.

3. The United State President's Council of Advisors for Science and Engineering (PCAST) recently indicated the need for receiver performance standardization and regulation to ensure a flexible and efficient utilization of spectrum. This is in contrast to the customary practice in which only transmitters are standardized and regulated. However, any form of receiver performance specification requires a simple, measurable, and exhaustive receiver performance metric. Section 3.4 shows that the CSR receiver modeling technique can also be used to develop a single-valued receiver performance metric. The metric can be used by regulatory institutions such as the Federal Communication Commission (FCC) to explicitly state the minimum performance requirements of interference-protectable receivers. The metric is exhaustive in terms of accounting for various attributes of receivers. The practical validity of the developed metric is also verified using hardware-based experiment in Section 6.4.1.

4. This research also presents the design and implementation of a cognitive engine that controls the local-oscillator and sampling frequencies in receiver RF front-ends. Chapter 4 presents the theoretical development and simulation based evaluation of the cognitive engine. The experimentation of the cognitive engine on hardware is presented in Section 6.4.3 and 6.4.4. This research shows that this cognitive engine can be applied in poorly-selective receivers to minimize the effect of neighboring-channel signals on the desired signal and

improve the sensitivity of the receiver. In other words, the cognitive engine virtually creates a good pre-selector without incorporation of an actual filter[3].

5. The cognitive engine relies on spectrum sensing to know the frequency location and power level of neighboring-channel signals. However, implementing the spectrum sensing system in this research presented two unique challenges. First, unlike other cognitive radios which employ detection-based spectrum sensing to determine just the absence or presence of a signal, the cognitive engine in this research requires an estimation of the actual power level in all the neighboring-channels. Second, because the cognitive engine is applied in poorly-selective receivers, the accuracy of the spectrum sensing is degraded by receiver impairments (see Section 5.1). This research presents an estimation-based multi-band spectrum sensing mechanism that is robust against the effects of receiver impairments. The theoretical development of this mechanism is presented in Chapter 5. The mechanism is experimented on hardware and the results are presented in Section 6.4.2. Furthermore, Section 5.5 shows the application of the developed spectrum sensing mechanism in dynamic spectrum access networks.

6. The customary approach uses automatic-gain-control (AGC) to address strong received signals. In this research, it is shown that a receiver architecture that relies on an auxiliary receive path and digital-filters performs better than AGC in handling of strong signals, and expands the dynamic range of the receiver. The theoretical development, simulation-based analysis, and hardware experimentation of this mechanism are presented in Chapter 7.

[3] Note that some pre-selection is inherent in a receiver due to the antenna and matching circuit.

1.7 Dissertation Outline

This research introduces the concept of Cognitive RF front-end control (CogRF). The particular cognitive RF front-end developed in this research controls the local oscillator and sampling frequencies of receiver RF front-ends. Chapter 2 presents background material, including a discussion on other types of cognitive RF front-end control mechanisms.

Chapter 3 establishes the system model for this dissertation. It introduces the channelized spectrum representation model. This model is used to design the cognitive engine in Chapter 4 and the spectrum sensing module in chapter 5. Chapter 6 presents a hardware implementation that is used to verify the theoretical assertions in this research. CogRF is applicable mainly when the received signals is weak, or moderately strong. Another approach that addresses very strong neighboring-channel signal is discussed in Chapter 7. Finally, Chapter 8 concludes the dissertation by summarizing the major findings and core contributions.

Chapter 2

Benefits of Cognitively Controlling RF Front-end Parameters

The previous chapter defined CogRF as an RF front-end that controls the Local-Oscillator (LO) and sampling frequencies in receivers. In broad sense, however, the concept of CogRF applies to controlling any analog RF front-end parameters. This chapter identifies different RF front-end parameters that can be cognitively controlled and the resulting benefits. The chapter starts by showing how the concept of CogRF evolved from the cognitive radio concept.

2.1 From Cognitive Radio to Cognitive RF Front-end

In his seminal dissertation, Mitola proposed the use of artificial intelligence to control the parameters of wireless devices. He named this concept Cognitive Radio [4, 49]. Until recently, however, the cognitive radio concept was applied to control only the digital parameters of wireless devices or radios (for example [50-53]). This is because the analog section of radios (the RF front-end), was not flexible enough to motivate or allow a software-based cognitive control.

The value of digital electronics lies on its flexibility where CMOS is the technology behind. Due to recent technological advancements, it is now becoming possible to also implement flexible RF front-ends using CMOS [54, 55]. Until recently, it was not possible to implement RF front-ends using CMOS because of its low cut-off frequency [55]. Furthermore, simulation and design models of CMOS were not optimized for radio-frequency-ranges. Process technologies are now advanced enough to fabricate deep sub-micron CMOS transistors with cut-off frequency in excess of 100 GHz [55]. Moreover, the properties of CMOS in the radio-frequency-ranges are now well understood [54].

For these reasons, digital and RF circuits can now be co-designed and implemented in the same die using CMOS technology. For example, it is now possible to incorporate a digitally-controlled switch inside an RF circuit [56]. Accordingly, parameters of the RF front-end are not off-limit from cognitive control anymore.

This research is motivated by the new engineering opportunity that became available due to the advancements in RF CMOS and the advent of highly flexible RF front-ends. The maturity of RF CMOS is now evident by the introduction of

highly reconfigurable RF CMOS based radio frequency integrated circuits (RFICs) [57-61].

The application of a cognitive radio is determined by the type of "knobs" it controls and the type of "meters" it observes [50, 51]. The term "knob" refers to the radio parameter that is controlled by the cognitive mechanism. The cognitive mechanisms observes the states of the signal, the radio and/or the environment before adjusting the settings of the knobs. The observed parameters are referred as "meters." In link-adapting cognitive radios [51, 53], for example, parameters such as modulation index and coding-rate are the knobs, while packet-error-rate and signal-to-noise-ratio are the meters.

CogRF differs from traditional cognitive radios because it controls RF front-end knobs, only. Figure 2.1 shows the evolution of CogRF from a traditional radio and a traditional cognitive radio. The knobs in CogRF are located inside the RF front-end. On the other hand, the knobs in traditional cognitive radios are contained inside the digital-processor.

Both CogRF and traditional cognitive radio contain four major elements; which are the cognitive engine, the spectrum sensor, the digital processor and the RF front-end. The description of these elements are presented below.

RF Front-end: Before the 1970s, radio devices were made using analog circuits only. After the advent of digital electronics, however, it became possible to digitally implement significant portions of the radio. Nevertheless, the physics of the electromagnetic spectrum remains to be analog. For this reason, an analog circuitry called RF front-end is used to interface the digital sections of a radio with the electromagnetic spectrum.

Digital processor: In contemporary radios (for example, cellphones), most of the radio signal processing is carried out digitally. Elements of digital wireless communication such as modulation and demodulation, coding and decoding, frame assembly and disassembly, channel estimation and equalization are invariably implemented in the digital processor.

Cognitive engine: The cognitive engine is the brain of CogRF and cognitive radio. The artificial intelligence algorithms that establish the "cognitive-ness" of these mechanisms are housed in the cognitive engine. In traditional cognitive radios, the cognitive engine controls the elements of the digital processor[4], and it can be implemented at the network-level [63]. In contrast, CogRF's cognitive engine controls the elements of the RF front-end and it is implemented locally in the radio. In both cases, the cognitive engine makes its control decisions based on the observations it obtains from the spectrum sensor, or performance metrics such as packet-error-rate.

Spectrum sensor: CogRF and traditional cognitive radio incorporate spectrum sensing to measure the occupancy of the received spectrum. The output of the spectrum sensing is used by the cognitive engine to make informed decisions. In Time-Domain-Duplexed (TDD) based systems, the spectrum sensor can share the same RF front-end with the digital processor. In FDD systems, however, two separate RF front-ends need to be employed by the spectrum sensor and the digital processor.

[4] The exception here is that in traditional DSA-based cognitive radios, the transmission frequency, which can be an analog parameter, is controlled by a cognitive engine.

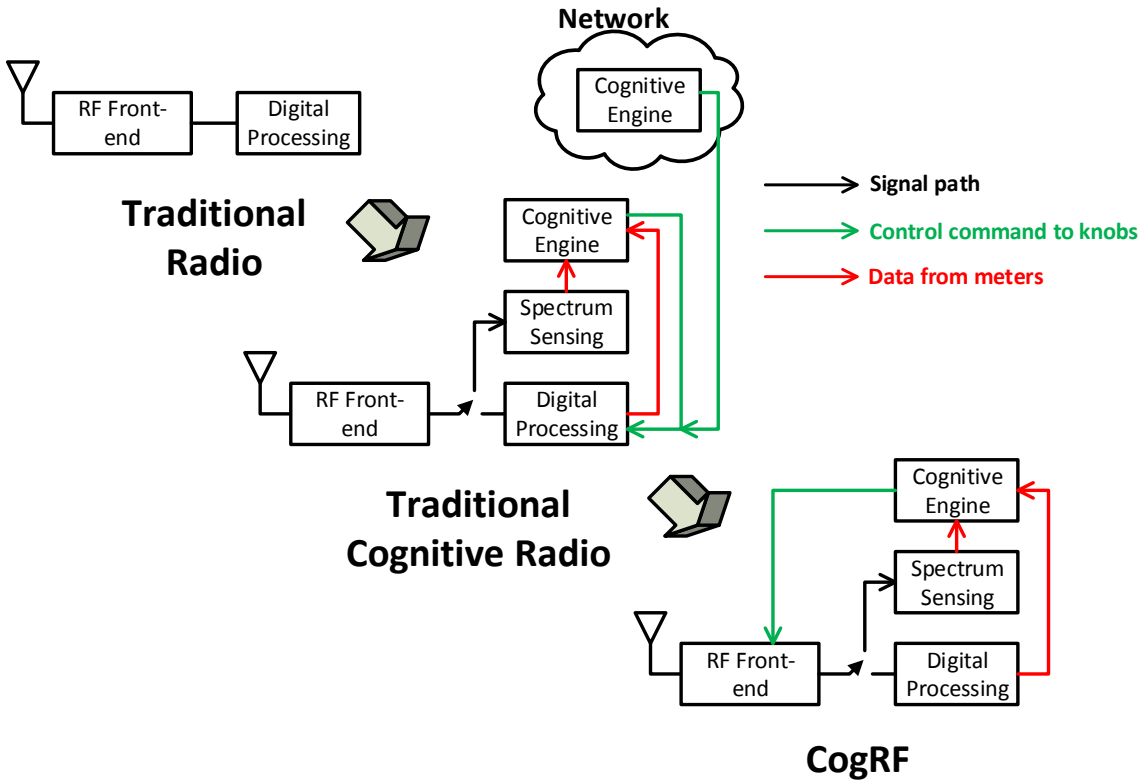

Figure 2.1 Comparing traditional cognitive radio and CogRF

2.2 Review on Flexible RF Front-ends

As it was mentioned previously, CogRF is motivated by the advent of highly flexible RF front-ends. For example, IMEC's [57] RFIC is implemented on 130 nm CMOS technology. This RFIC contains a digital-to-analog convertor and analog-to-digital converter on the same chip. It operates from 100 MHz to 6 GHz and uses a combination of tunable voltage controllable oscillator (VCO) and divide-and-multiply circuits to implement a flexible local oscillator. Other RF parameters such as bandwidth of baseband filters, gains of amplifiers, current bias

of amplifiers and many more are all controllable through digital ports provided on the RFIC.

Similar RFICs are also released by LIME microsystems[60], Analog Devices [61] and Motorola [59]. In [56] and [64], IMEC researchers present various techniques that can be used to implement highly flexible baseband radio circuits. Other research efforts are also attempting to further increase the flexibility of RF front-ends. The Defense Advances Research Projects Agency (DARPA) is now funding researches on RF FPGAs [65].

The block diagram of a flexible direct-conversion type RF front-end transceiver is shown in Figure 2.2. The RF front-end contains components such as pre-selector filter, power amplifier (PA), Low-Noise Amplifier (LNA), mixer, local oscillator (LO), baseband amplifier, baseband filter, analog-to-digital convertor (ADC) and digital-to-analog convertor (DAC). From these components, LNA, mixer, baseband filter, baseband amplifiers, ADC and DAC are often integrated in an RFIC. On the other hand the power amplifier, the pre-selector and the antenna system (not shown in the figure) are often placed off-chip, or within a specialized front-end module (FEM) that can handle higher power levels.

The figure also shows that some elements of the RF front-end are reconfigurable. Notable reconfigurable parameters of flexible RF front-ends are outlined in Table 2.1. These parameters are the knobs that are controlled by the cognitive engine in CogRF.

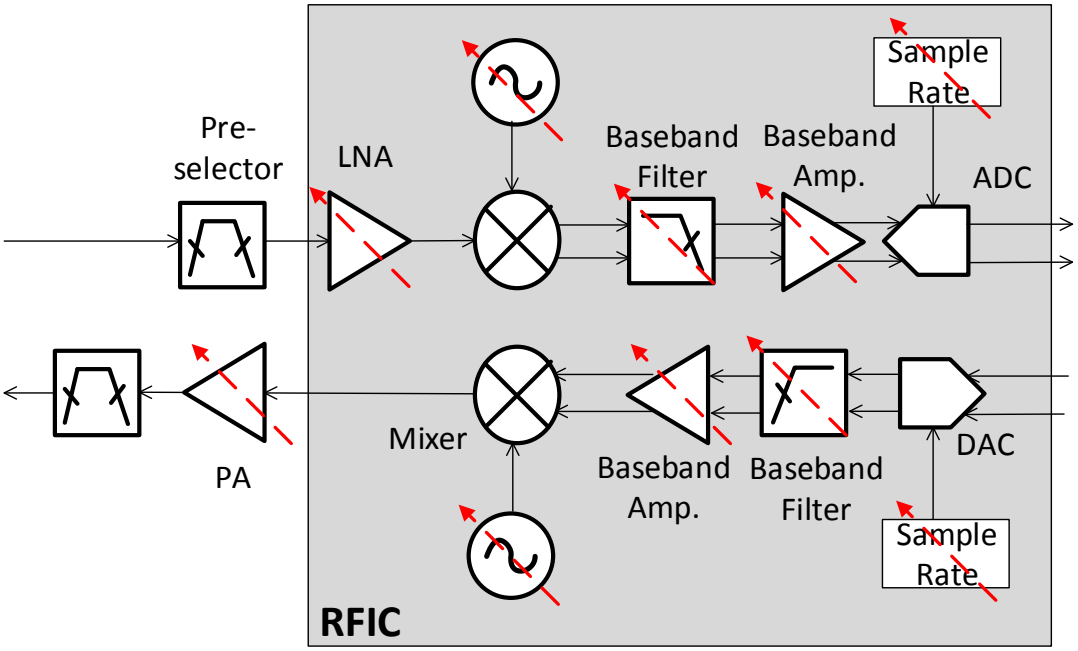

Figure 2.2 Reconfigurable direct-conversion type RF front-end transceiver.

Table 2.1 Reconfigurable parameters in flexible RF front-ends.

RF Front-end element	**Reconfigurable parameters**
Power amplifier	• Voltage or/and current bias [38, 66] • Antenna loading (elements of the matching circuit) [38, 67]
LO	• LO frequency [57-61]
Baseband	• Selectivity [57-61] • Gain[57-61]
DAC/ADC	• Sampling rate • Number-of-bits-per-sample
LNA	• Gain [57-61] • Current bias [59, 61]

2.3 Example CogRF Mechanisms

This section describes different types of CogRF mechanisms. CogRF mechanisms can be profiled using three attributes; the knobs, the meters, and the objective of the mechanism. The knobs in CogRF can be any of the parameters listed under Table 2.1. Examples of meters are spectrum sensing and signal-to-interference (SIR) ratio.

The objectives of CogRF on transmitters and receivers can be different. In transmitters, the objective may be either minimizing the power consumption of the transmitter or minimizing off-band emissions. To attain these objectives, CogRF adapts the transmitter to the characteristics and requirements of the transmitted waveform.

In receivers, the objective may be maximizing the Signal-to-Noise Ratio (SNR) at the output of the ADC, maximizing the Signal-to-Interference-and-Noise-Ratio (SINR) at the output of the ADC, or minimizing the power consumption of the receiver. To attain these objectives, CogRF dynamically adapts the receiver to the occupancy state of the spectrum.

Example CogRF mechanisms are described below:

1. *Knobs:* LNA gain and LNA bias
   Meter: Spectrum sensing
   Objective: Maximizing SINR at the output of the ADC
   Concept: By varying the gain of the LNA, it is possible to obtain up to 2 dB improvement in its noise figure [68-71]. Furthermore, according to the RF-cascade noise figure formula [45], increasing the gain of LNA also improves the overall noise figure of the receiver. However, LNA's gain should not be

increased if there is a strong adjacent-channel signal in the spectrum. This is because non-linearity performance of the receiver quickly degrades as gain increases in the presence of strong signals. However, if no strong signal is in the received spectrum, the gain of the LNA can be aggressively increased to improve the noise performance of the receiver. This mechanism needs to employ spectrum sensing to determine the power levels of adjacent-channel signals. Similarly, the bias of the LNA can be increased to improve its non-linearity performance at the expense of increasing the power consumption.

2. *Knob:* receiver's LO frequency

   Meter: Spectrum sensing

   Objective: Maximizing SINR at the output of the ADC, and minimizing power consumption

   Concept: The LO frequency of a direct-conversion receiver can be set such that the receiver operates either in zero-IF mode or low-IF mode [72]. Zero-IF receivers are susceptible to impairments such as DC offset, flicker noise and second-order intermodulation. For this reason, zero-IF receivers often need additional circuitry such as DC-offset correction and chopper stabilization [73] to minimize the distortion on the desired signal. In low-IF receivers, however, engaging a correction and stabilization circuits may not be necessary; and thus, power consumption can be reduced. However, low-IF receivers suffer from interference from image signals [12] and increase in the power consumption of the ADC due to the increase in the sampling frequency. With the objective of globally minimizing the receivers power consumption and maximizing the Signal-to-Interference Ratio (SIR) of the desired signal at the output of the ADC, a cognitive control can employ spectrum sensing to determine the frequency location of potential image signals and optimally adjust the LO frequency.

3. *Knob*: Bandwidth of baseband filters

   Meter: Spectrum sensing

   Objective: Minimizing power consumption

   Concept: In gm-C type baseband filters, the power consumption the filters increases with cube of its selectivity (*Q*). Accordingly, significant power can be saved by reducing the selectivity of such filters [74]. Hence, a cognitive control can be used to reduce the selectivity of a receiver's baseband filters when no powerful neighboring-channel signal is detected in the spectrum. Similarly, the selectivity of a transmitter's baseband filter can be reduced when a waveform with "less-splattering" windowing is being transmitted; or when the off-band-emission requirement of the network is relaxed[5].

4. *Knob:* Number-of-bits-per-sample

   Meter: Signal-to-quantization-ratio (SQNR)

   Objective: Minimizing power consumption

   Concept: Increasing the number-of-bits-per-sample potentially increases SQNR of the signal at the input of the digital processor (or the output of the ADC) [72]. If the digital-processor and the RF front-end are implemented in two separate chips, increasing the number-bits-per-sample also increases the power consumption of the digital-bus that interfaces the two chips. If the SQNR of the desired signal is well above the minimum level, the number-of-bits-per-sample can be reduced after sampling (i.e. by simply discarding least-significant bits) to decrease the power consumption of the receiver. This mechanism needs to employ "meters" in the digital processor to measure the SQNR of the desired signal.

[5] This assertion implicitly assumes a highly flexible, liquid-protocol-network. In such network, almost all aspects of the network, including the protocol of the waveform can be changed dynamically. Liquid-protocol- network can be considered as the ultimate vision of cognitive radio research [2].

5. *Knob:* Receiver's sampling rate

   Meter: Spectrum sensing

   Objective: Maximizing SINR at the output of the ADC, and minimizing power consumption

   Concept: Typically, anti-aliasing filter is employed to reject signals beyond the first-Nyquist zone of the ADC. However, this filters will not be perfectly selective, and some level of aliasing will always occur. Aliasing causes signals from higher-order-Nyquist zones to fold into the desired channel [72, 75]. The frequency of aliased signals is determined by the sampling frequency. Hence, the sampling frequency can be adjusted such that the alias of strong neighboring-channel signals will not interfere with the desired signal. It can be noted that this can be achieved without requiring the sampling frequency to be twice the frequency of neighboring-channel signals. The mechanism needs to adjust the sampling frequency such that the aliases occur outside the frequency range of the desired signal. This mechanism needs to employ spectrum sensing to determine the power levels and frequency location of neighboring-channel signals.

6. *Knob:* The bias, back-off and operation mode of power amplifiers

   Meter: Peak-to-average ratio of transmitted waveform

   Objective: Minimizing power consumption

   Concept: Power amplifiers (PAs) generally become more non-linear when their power consumption is reduced [46]. The bias (or the signal's back-off) and the operation mode of a PA can be made to be adaptive to the characteristics of the waveform. Various operation modes of PA's are reviewed in [46]. In reconfigurable, and multi-purpose PAs, the bias of the PA can be reduced, or the operation mode of the PA can be changed to class-AB when the transmitted waveform is non-linearity tolerant (for example, an FM signal). For non-

linearity sensitive (high peak-to-average-ratio) signals like OFDM, class-A mode PA has to be used; and the level of the PA biasing (or the signals back-off) has to be increased.

The above list of CogRF mechanisms is obviously not exhaustive. Other types of CogRF mechanisms are expected to emerge as the flexibility of RF front-ends increases.

As it is stated previously, a particular type of CogRF is investigated in this research. The profile of the particular CogRF that is developed in this research is as follows;

Knobs: Receiver's LO and sampling frequencies
Meter: Spectrum sensing
Objective: Maximizing SIR at the output of the ADC or maximizing the sensitivity of the receiver

This dissertation presents the design, theoretical development and hardware evaluation of this CogRF.

2.4 Chapter Summary

In this research, CogRF refers to a mechanism that intelligently controls only the LO and sampling frequencies of receivers. This chapter shows that CogRF can be used to adjust a variety of knobs, using a variety of observation "meters". Examples of CogRF mechanisms that control various knobs including LNA gain, LNA bias, sampling frequency, LO frequency, and power amplifier bias, are discussed in this chapter.

This chapter also differentiates traditional cognitive radio systems from CogRF. Traditional cognitive radios control digital knobs only. Cognitive control had not been considered for RF front-end knobs because analog RF front-ends were inflexible, and RF front-end knobs commonly did not exist. The CogRF idea was motivated by the advent of highly flexible, and digitally-controllable RF front-ends. This chapter indicates that CogRF in general can provide various benefits including a reduction of power consumption, and an increase in Signal-to-Interference-and-Noise-Ratio (SINR) of the desired signal.

Chapter 3

Channelized Spectrum Representation

This chapter presents a new receiver RF front-end modeling technique. This model is an integral component of both the cognitive engine and the spectrum sensing algorithms presented in Chapter 4 and Chapter 5, respectively. The chapter starts by briefly reviewing existing RF front-end models and showing why they cannot be used to develop CogRF.

3.1 Existing models: Why are they Lacking?

Various RF front-end modeling techniques are found in the technical literature, but they are incapable of modeling the energy re-distribution in poorly-selective

receivers. Examples of commonly used linear and a non-linear RF front-end models are discussed below.

One of the most common RF front-end model is the baseband-representation which is commonly used by digital communication engineers [76]. In baseband-representation, the transmitter and the receiver RF front-ends are modeled as a noise-adding linear amplifiers/attenuators. This model represents the reality only when both the transmitter and the receiver RF front-ends are highly linear, and the receiver is highly selective. Baseband-representation cannot characterize how the desired signal is distorted by neighboring-channel signals in poorly-selective receivers.

Power-series [11] and Voltera series [77] models can represent the input-to-output non-linearity characteristics of individual RF front-end elements, and (perhaps) the overall RF front-end. However, these models fail to capture the down-conversion and sampling operations[6], which are the causes of the energy re-distribution in the receiver.

This research develops an RF front-end model that can naturally capture the energy re-distribution process in poorly-selective receivers. The model is called Channelized Spectrum Representation (CSR).

[6] These effects are referred as inherent non-linearity. The description is given in Appendix E.

3.2 Channelized Spectrum Representation (CSR)

3.2.1 Receiver Architecture

A direct-conversion [12] type receiver, which is shown in Figure 3.1, is assumed in the theoretical development of the CSR model. The objective of this assumption is merely for illustration purpose. The results can be extended to the super-heterodyne receiver architecture [12] as well.

After passing through the pre-selector filter, the received signal is amplified by a low noise amplifier (LNA). In the development of CogRF, the undesired non-linearity (see Appendix E for description) of the LNA and other receiver elements is neglected. Consideration for the effects of receiver non-linearities are discussed in Chapter 7.

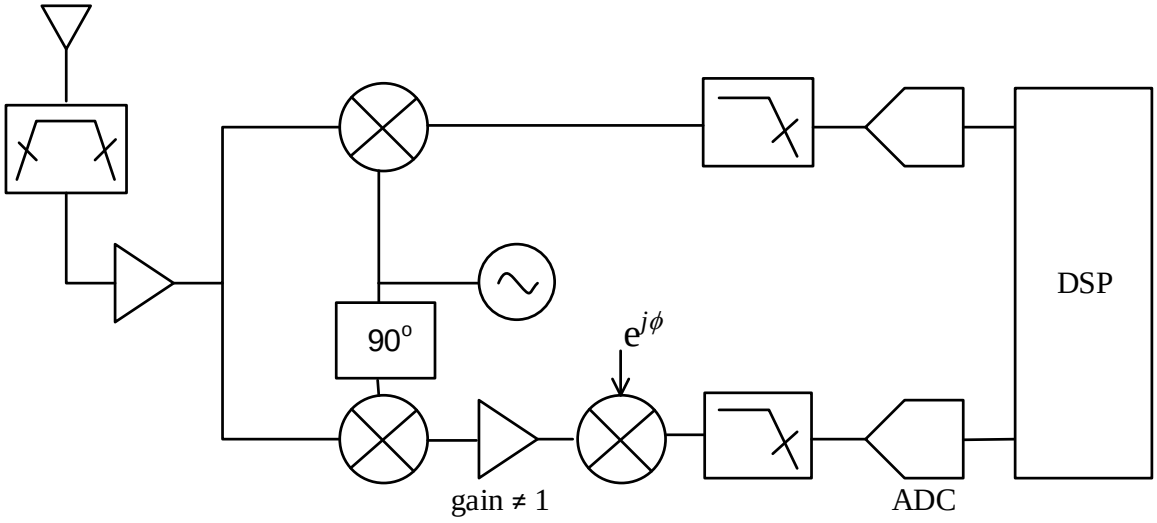

Figure 3.1 Receiver RF front-end architecture.

The output of the LNA is down-converted using quadrature mixers. Ideally, the two branches of the quadrature mixer are perfectly balanced in both amplitude and phase such that image signals are perfectly rejected. However, the two branches will always be mismatched [12, 78]. This mismatch is commonly referred as IQ imbalance. The mismatch results in a finite image rejection that ranges between 25 and 60 dB in typical direct-conversion receivers.

After the down-conversion, the baseband signal is passed through anti-aliasing filters before it is sampled by the ADCs. The sampled signal is processed in the digital signal processor (DSP). Ideally, the anti-aliasing filter is a brick-wall filter that rejects all signals outside the first Nyquist zone. However, practical filters are limited with a finite rejection level in their stop-band. Thus, some level of aliasing will always occur during sampling.

The effects of IQ imbalance and imperfect anti-aliasing filter are illustrated in Figure 3.2. The figure shows how down-conversion and sampling re-shuffle the energies of RF signals (and their mirrors) in the frequency domain.

The original RF signal in Figure 3.2 contains three active signals and their mirrors. Ideally, the down-conversion mixer shifts the positive frequency signals to baseband and eliminates their mirrors. However, attenuated version of the mirrored signals appears at baseband due to IQ imbalance.

In addition, it can be observed that the strongest RF signal and its mirror map to a baseband frequency outside the first Nyquist zone (from $-F_s/2$ to $F_s/2$) of the ADC. Ideally, these signals would be perfectly rejected by the anti-aliasing filter. In a non-ideal receiver, however, the finite rejection at the anti-aliasing filter's stop-band allows strong signals from higher order Nyquist zones to fold into the first Nyquist zone.

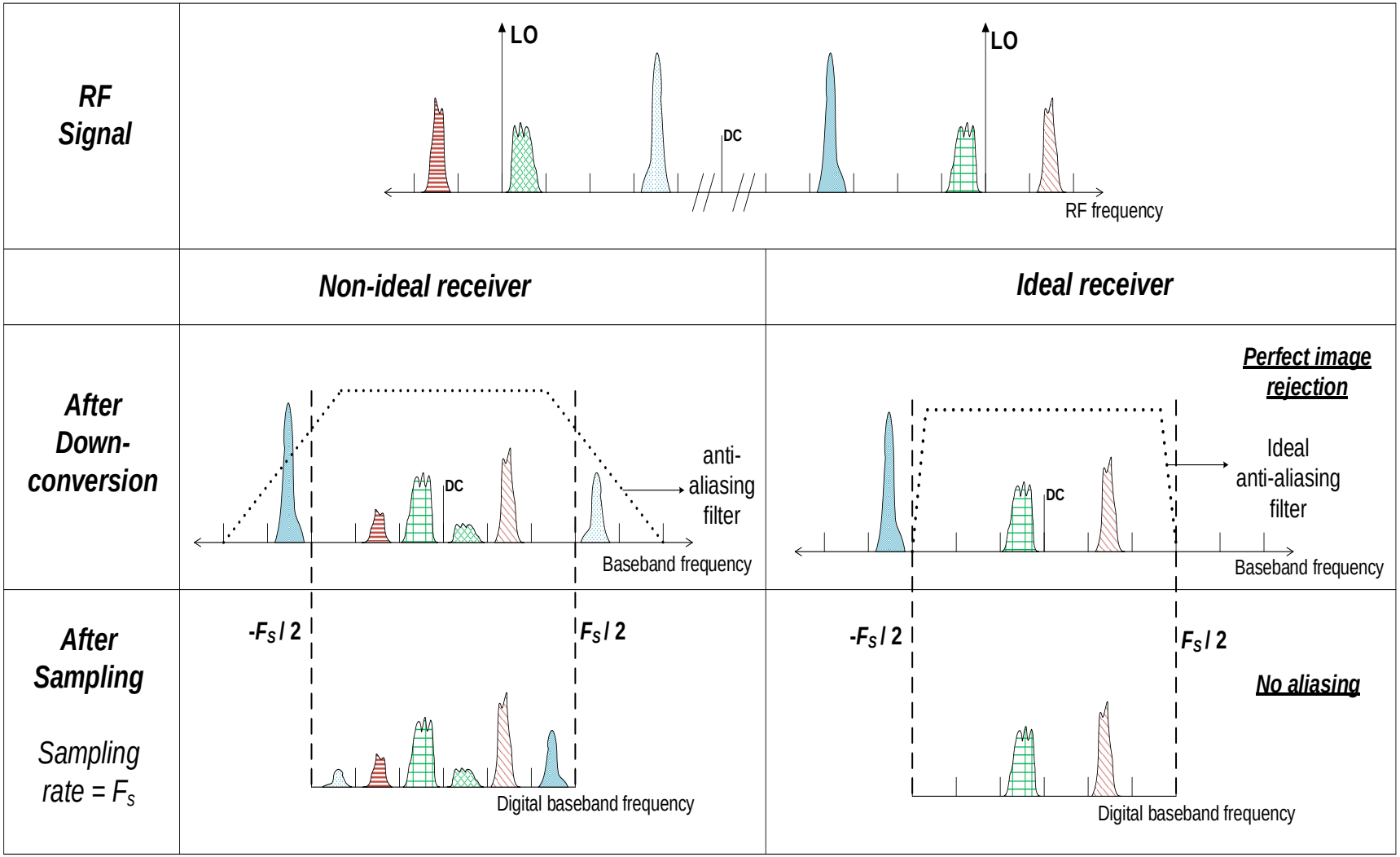

Figure 3.2 Comparison of ideal and non-ideal direct conversion receiver.

3.2.2 Signal Model

As it can be inferred from its name, the CSR model channelizes a signal into multiple equal-bandwidth channels. The overall signal is the sum of the signals contained within each channel. A signal $x(t)$ is given by,

$$x(t) = \sum_{i=-\infty}^{\infty} \tilde{x}_i(t) \tag{3.1}$$

and,

$$\tilde{x}_i(t) = x(t) * \Im^{-1}\left\{\Pi\left(\frac{f - f_i}{\Delta}\right)\right\} \tag{3.2}$$

where, $\tilde{x}_i(t)$ represents the signal contained in the i^{th} channel and Δ represents the bandwidth of each channel. The term $f_i = i\Delta - \Delta/2$ represents the center frequency of the i^{th} channel, where $i = ..., -2, -1, 0, 1, 2, ...$. The operators $*$ and $\Im^{-1}$ represent convolution and inverse Fourier transform, respectively. The frequency domain function $\Pi\left(\frac{f - f_i}{\Delta}\right)$ represents a brick-wall filter centered at f_i, with bandwidth Δ.

The average power contained in the i^{th} channel is computed as,

$$p_X[i] = E\left\{\left|\tilde{x}_i(t)\right|^2\right\} \tag{3.3}$$

where, $E\{\ \}$ is an expectation operator.

Finally, CSR of $x(t)$ is given by an infinite length vector,

$$\boldsymbol{P_X} = \begin{bmatrix} ... & p_X[i-1] & p_X[i] & p_X[i+1] & ... \end{bmatrix}^T \tag{3.4}$$

CSR can be computed for the signals obtained at different stages in the receiver. For example, CSR can be computed for the input RF signal, the output of the mixer, the output of anti-aliasing filter, and the output of the ADC. CSR model can also be defined for receiver elements, such as a mixer, a filter or ADC. CSR model of a receiver element is defined as the transformation between the input CSR and the output CSR of the element.

The following sub-sections derive CSR models of the mixer, the anti-aliasing filter, and the ADC. Finally, the CSR model of the overall receiver is derived.

3.2.3 Modeling the Down-conversion Mixer

A block diagram of a quadrature down-conversion mixer is shown in Figure 3.3. The mixer down-converts a real-valued input signal $w(t)$ to a complex-valued output signal $v(t)$. The mixer uses a periodic signal with frequency f_{LO} to down-convert $w(t)$ to $v(t)$.

Without a loss of generality, assume $f_{LO} = l\Delta - \Delta'$, where l is a positive integer, and Δ' is a fraction of Δ. Typically $l >> 0$. Also assume that f_{LO} is at the edge of the l^{th} channel.

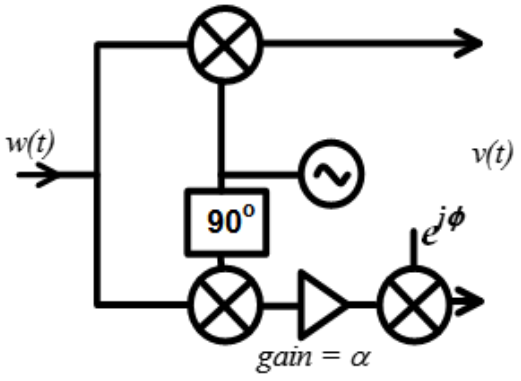

Figure 3.3 Model of quadrature mixer.

The time domain model of a quadrature mixer is given by,

$$v(t) = w(t)\cos(2\pi f_{LO}t) + j(1+\alpha)e^{j\phi}w(t)\sin(2\pi f_{LO}t) \tag{3.5}$$

where α and ϕ represent the amplitude and phase mismatches, respectively.

Using (3.1), (3.2) and (3.3), and assuming that the signals contained in different channels are uncorrelated to each other, it can be shown that (see Appendix A for detailed proof):

$$p_V[i] = p_W[l+i] + \beta p_W[l-i] \ , \tag{3.6}$$

where

$$\beta = \left|\frac{1-(1+\alpha)e^{j\phi}}{1+(1+\alpha)e^{j\phi}}\right|^2 \tag{3.7}$$

and the image rejection ratio is given in dB as $\text{IIR} = -10\log(\beta)$.

The pre-selector filter shown in Figure 3.1 limits the reception bandwidth of the received signal. Hence, it is reasonable to assume finite-length CSR vectors. For example, the number of channels in CSR of the mixer input can be computed as the ratio of the reception bandwidth of the pre-selector filter to the channel bandwidth. In addition, it is sufficient to consider only positive frequency channels of an RF signal because it is real-valued. At baseband, however, both negative and positive frequencies are considered because the signal is complex valued.

Thus, (3.4) is modified to be finite dimension by letting $\boldsymbol{P}_w = \left[\, p_w[1] \;\; p_w[2] \;\; \ldots \;\; p_w[N] \,\right]^T$ where N is the number of RF channels (in positive

frequency). The number of baseband channels will also be equal to N. Accordingly, $\boldsymbol{P}_v = \left[p_v[1] \quad p_v[2] \quad \ldots \quad p_v[N] \right]^T$.

Example: Assume the RF signal contains four channels and the LO frequency is at the middle of the reception bandwidth as shown in Figure 3.4.

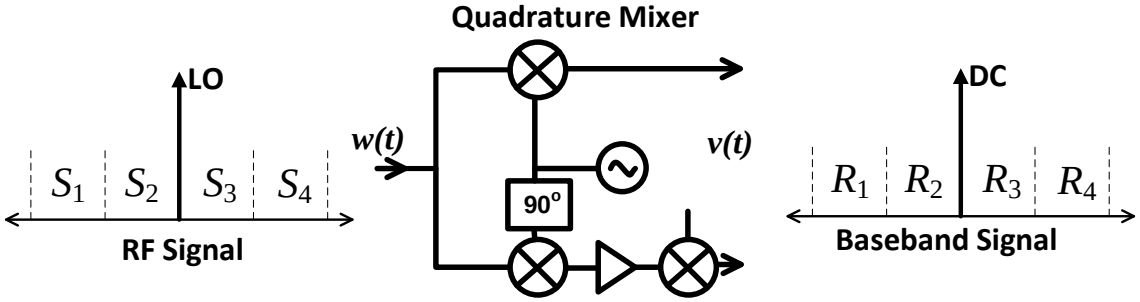

Figure 3.4 Example quadrature mixer down-conversion.

The average powers in the RF sub-bands are given by S_1, S_2, S_3, and S_4. Similarly, the average powers in baseband sub-bands are given by R_1, R_2, R_3, and R_4. From (3.6) $R_1 = S_1 + \beta S_4$, $R_2 = S_2 + \beta S_3$, $R_3 = S_3 + \beta S_2$, and $R_4 = S_4 + \beta S_1$. This can be written in matrix form as,

$$\begin{bmatrix} R_1 \\ R_2 \\ R_3 \\ R_4 \end{bmatrix} = \begin{bmatrix} 1 & 0 & 0 & \beta \\ 0 & 1 & \beta & 0 \\ 0 & \beta & 1 & 0 \\ \beta & 0 & 0 & 1 \end{bmatrix} \begin{bmatrix} S_1 \\ S_2 \\ S_3 \\ S_4 \end{bmatrix} \tag{3.8}$$

Hence, the CSR model of the quadrature mixer in Figure 3.3 is given by the matrix,

$$\boldsymbol{A}_{\boldsymbol{mix}} = \begin{bmatrix} 1 & 0 & 0 & \beta \\ 0 & 1 & \beta & 0 \\ 0 & \beta & 1 & 0 \\ \beta & 0 & 0 & 1 \end{bmatrix} \tag{3.9}$$

Note that the elements of $\boldsymbol{A}_{\boldsymbol{mix}}$ are function of the LO frequency because the level of imbalance between the two paths varies with frequency [79]. For this reason, the matrix is referred as $\boldsymbol{A}_{\boldsymbol{mix}}(f_{LO})$ in this study.

3.2.4 Modeling Baseband Filter

As shown in Figure 3.5, the input of the baseband filter is a complex-valued signal $w(t)$ and the output is a complex-valued signal $z(t)$.

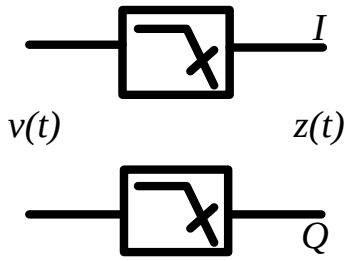

Figure 3.5 Model of quadrature baseband filter.

The time domain characteristics of a complex filter is given by,

$$z(t) = v(t) * h(t) \tag{3.10}$$

where $h(t)$ is the impulse response of the filter. Approximating the frequency response of the baseband filter in the i^{th} channel by a constant H_i, CSR model of the baseband filter becomes,

$$p_Z[i] \approx p_V[i]\left|H_i\right|^2 \tag{3.11}$$

Example: Assume the input of the baseband filter contains four channels. The frequency response of the filter at the center of each channel is given by, H_1, H_2, H_3, and H_4, respectively. As shown in Figure 3.6, the average power in the input channels are given by S_1, S_2, S_3, and S_4. Similarly, the average powers in the output channels are given by R_1, R_2, R_3, and R_4.

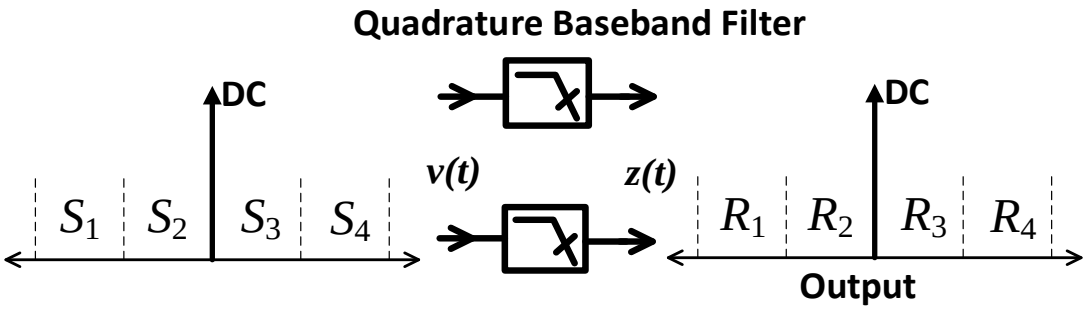

Figure 3.6 Example quadrature baseband filtering.

From (3.11), $R_1 = S_1 |H_1|^2$, $R_2 = S_2 |H_2|^2$, $R_3 = S_3 |H_3|^2$, and $R_4 = S_4 |H_4|^2$. This can be written in matrix form as,

$$\begin{bmatrix} R_1 \\ R_2 \\ R_3 \\ R_4 \end{bmatrix} = \begin{bmatrix} |H_1|^2 & 0 & 0 & 0 \\ 0 & |H_2|^2 & 0 & 0 \\ 0 & 0 & |H_3|^2 & 0 \\ 0 & 0 & 0 & |H_4|^2 \end{bmatrix} \begin{bmatrix} S_1 \\ S_2 \\ S_3 \\ S_4 \end{bmatrix} \tag{3.12}$$

Hence, CSR model of the quadrature filter in is given by the matrix,

$$\boldsymbol{A}_{\boldsymbol{fil}} = \begin{bmatrix} |H_1|^2 & 0 & 0 & 0 \\ 0 & |H_2|^2 & 0 & 0 \\ 0 & 0 & |H_3|^2 & 0 \\ 0 & 0 & 0 & |H_4|^2 \end{bmatrix} \tag{3.13}$$

3.2.5 Modeling Analog-to-digital Converters

In this study, a quadrature ADC is assumed. The block diagram of this ADC is shown in Figure 3.7.

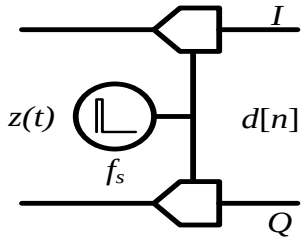

Figure 3.7 Model of ADC.

The time domain model of the ADC is,

$$d[n] = z(t)\big|_{t=nT_S} \tag{3.14}$$

where $T_S = 1/f_S$ and f_S is the sampling rate. In this study, we assume f_S is a positive-integer multiple of channel bandwidth, Δ. Thus, $f_S = s\Delta$ for $s = 1, 2, \ldots$. Hence, s represents the number of channels at the output of the ADC (in the first Nyquist zone).

Using (3.1), (3.2), and (3.3), and assuming that the signals contained in different channels are independent to each other, the ADC is impulsively sampling[7], it can be shown that (see Appendix B for detailed proof);

$$p_d[i] = (s\Delta)^2 \sum_{k=-\infty}^{\infty} p_Z[i - ks] \tag{3.15}$$

[7] Note that the filtering effects of non-impulsive filters can be incorporated in the characteristics of the baseband filter.

Example: As shown in Figure 3.8, assume the input of the ADC contains six active channels and the output contains only two channels; that is, $s = 2$.

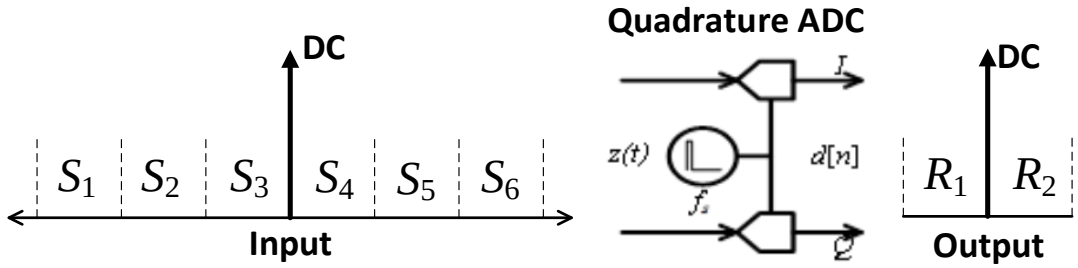

Figure 3.8 Example ADC sampling.

The average power in the input channels is given by S_1, S_2, S_3, S_4, S_5 and S_6. Similarly, the average power in the output channels is given by R_1 and R_2. From (3.15), $R_1 = S_1 + S_3 + S_5$ and $R_2 = S_2 + S_4 + S_6$.

This can be written in matrix form as,

$$\begin{bmatrix} R_1 \\ R_2 \end{bmatrix} = \begin{bmatrix} 1 & 0 & 1 & 0 & 1 & 0 \\ 0 & 1 & 0 & 1 & 0 & 1 \end{bmatrix} \begin{bmatrix} S_1 \\ S_2 \\ S_3 \\ S_4 \\ S_5 \\ S_6 \end{bmatrix} \tag{3.16}$$

Hence, the CSR model of the ADC in Figure 3.7 is given by the matrix,

$$\boldsymbol{A}_{\boldsymbol{ADC}} = \begin{bmatrix} 1 & 0 & 1 & 0 & 1 & 0 \\ 0 & 1 & 0 & 1 & 0 & 1 \end{bmatrix} \tag{3.17}$$

Note that the elements of $\boldsymbol{A}_{\boldsymbol{ADC}}$ and its dimensions are a function of the sampling rate. For this reason, the matrix is referred as $\boldsymbol{A}_{\boldsymbol{ADC}}(f_s)$ in this study.

3.2.6 Modeling the whole Receiver

The matrix models of the mixer, the baseband filter, and the ADC can be multiplied as shown in (3.18) to obtain CSR model of the receiver between the pre-selector filter and the DSP. That is,

$$\boldsymbol{A}\left(f_{LO}, f_S\right) = \boldsymbol{A_{ADC}}\left(f_S\right) \cdot \boldsymbol{A_{fil}} \cdot \boldsymbol{A_{mix}}\left(f_{LO}\right) \tag{3.18}$$

where $\boldsymbol{A}\left(f_{LO}, f_S\right)$ is the *channelized spectrum (CS) transform* of the receiver.

The CS transform of the receiver transforms CSR of the mixer input to CSR of the ADC output. That is,

$$\boldsymbol{P_d}\left(f_{LO}, f_S\right) = \boldsymbol{A}\left(f_{LO}, f_S\right)\boldsymbol{P_w} + \boldsymbol{V}\left(f_{LO}, f_S\right) \tag{3.19}$$

where the vector $\boldsymbol{V}$ accounts for the power of internally generated signals such as additive noise and spurs. In this research, the vector $\boldsymbol{V}$ is referred as the *zero-input CS response* of the receiver. The vectors $\boldsymbol{P_d}$ and $\boldsymbol{P_w}$ are CSR of the mixer input and the ADC output, respectively.

The following observations can be stated about the CSR domain matrix model of the receiver:

- The values of the $\boldsymbol{P_d}$ and $\boldsymbol{P_w}$ vectors are non-negative.
- Both $\boldsymbol{A}$ and $\boldsymbol{V}$ change when either the LO or sampling frequency changes
- Note that all the elements of the matrix are non-negative numbers.
- In perfectly selective receivers, no neighboring-channel signal folds into the desired signal's channel. Without loss of generality, the receiver can be assumed to present a unity gain on the desired signal. Hence, in perfectly selective receivers,

$$a_{ij} = \begin{cases} 1, i = j \\ 0, i \neq j \end{cases} \tag{3.20}$$

where a_{ij} is the element of matrix $\boldsymbol{A}$ in (3.19).

- A matrix with a large number of non-zero elements corresponds to a poorly-selective receiver.
- The elements of $\boldsymbol{V}$ denote the level of noise and spurs in the receiver. The elements of the vector have small values in a spectrally pure receiver.
- The CSR modeling technique is developed by channelizing the signal into equal-bandwidth sub-bands. However, there can be scenarios in which the spectrum is fragmented into unequal bandwidth sub-bands. Such scenarios can be fitted into the CSR model by using very small channel bandwidths. In such cases, some signals may span over one or more adjacent channels in the CSR model.
- Some signals may span more than one channel in the CSR model. This may be because non-linearity distortions and phase noise cause the signal to splatter into adjacent channels, or the channel bandwidth is set to be smaller than the signal's bandwidth (due to the reason described in the previous bullet). In such cases, the "uncorrelated channels" assumption that is used to develop the CSR model of mixers and ADCs (see Appendix A and C) will be violated for those channels that carry signals coming from the same source. This violation may not cause significant perturbation on the CSR model because adjacent channels rarely become aliases or images to each other. However, it should be noted that the power level predicted by CSR computations may not be accurate in few of the channels due to this violation.

3.3 Measuring the CSR Matrix of a Receiver

This section discusses the CSR measurement mechanism for a receiver at a given LO and sampling frequency settings. Dropping the reference to LO and sampling frequencies in (3.19), it can be re-written as,

$$\boldsymbol{P_d} = \boldsymbol{A}\boldsymbol{P_w} + \boldsymbol{V} \tag{3.21}$$

where $\boldsymbol{A}$ is an $N \times M$ matrix (there are M channels in the received spectrum, within the reception bandwidth of the receiver, and N channels at the output of the ADC).

As it can be readily observed from (3.21), $\boldsymbol{V}$ can be obtained by measuring the power in each channel at the output of the ADC while no RF signal is being injected into the receiver. This is equivalent to estimating the noise-floor of the receiver. The measured zero-input CSR response of the receiver is denoted by $\hat{\boldsymbol{V}}$.

A column of $\boldsymbol{A}$, can be obtained by measuring the CSR of the ADC output and subtracting $\hat{\boldsymbol{V}}$ while only one channel is active at the receiver input. Thus, only one channel contains a signal with non-zero input power. The other columns of the CSR transform can be obtained by sequentially activating the corresponding input channels one at a time.

To mathematically formulate this measurement scheme, consider $\boldsymbol{x}_{in}^{j}$ be an $M \times 1$ vector, and the j^{th} element of the vector is equal to p_{meas} while the other elements are all equal to zero. Then, the estimate of the element in the i^{th} row and the j^{th} column of $\boldsymbol{A}$ is given by,

$$\hat{a}_{i,j} = \frac{\left(p^{i}_{d,\boldsymbol{X}^{j}_{in}} - \hat{v}^{i}\right)}{\left(p_{meas} - \hat{v}^{i}\right)} u\left(p^{i}_{d,\boldsymbol{X}^{j}_{in}} - \hat{v}^{i} - \Delta_{margin}\right) \tag{3.22}$$

where $u(\ )$ denotes a unit-step function; $p^{i}_{d,\boldsymbol{X}^{j}_{in}}$ is the power contained in the i^{th} channel at the output of the ADC while a signal with power equal to p_m is injected into the receiver in the j^{th} channel, and the other received channels are left inactive. Note that $i = 1,2,3,\ldots,N$. The term $\hat{v}^{i}$ denotes the measured zero-input power level in the i^{th} channel at the output of the ADC. Note that $\hat{a}_{i,j}$ is set to zero if $p^{i}_{d,\boldsymbol{X}^{j}_{in}} < \hat{v}^{i} + \Delta_{margin}$. This is because a CSR response at the output of the ADC can be detected only if it is reliably above the noise floor. The margin term Δ_{margin} is introduced to minimize the possibility that measurement errors cause negative $\hat{a}_{i,j}$ readings. The measured CSR transform of a receiver is denoted by $\hat{A}$.

Without any loss of generality for the discussion of this section, we assume that the gain from a sub-band at the receiver input to the corresponding channel at the ADC output is equal to 1. This is achieved by row-by-row normalization of the $\hat{\boldsymbol{A}}$.

3.4 CSR Based Receiver Performance Metric

Fueled by the LightSquared-versus-GPS (Global Positioning System) controversy [80], there has been a push for receiver standardization [81]. The controversy erupted after it was learned that LightSquared was planning to deploy an LTE network in the frequency band that is adjacent to what is currently used by consumer-GPS. Because GPS receivers had not been designed to handle adjacent-

channel interference [80], LightSquared could not get the permission to deploy its LTE network as planned.

This controversy indicated the need of regulating and standardizing receivers. The FCC has been considering whether to include receiver interference immunity performance specifications in its rules. Such rule would discourage, and eventually eliminate, the selling of poorly selective receivers.

Existence of a metric that can fully characterize a receiver is crucial for receiver standardizations and regulations [82]. Such metric can be used by regulatory bodies to define the minimum receiver performance requirements as a baseline criteria to the privilege of obtaining regulatory protection from interference [81]. Such metrics can also be used to inform a consumer about the performance of a receiver he/she is buying.

A receiver performance metric should fulfill the following criteria. First, following the practice in existing FCC rules, the metric should be single-valued and it should be simple to measure. Second, the metric should capture the impacts of multiple, if possible all, attributes of a receiver RF front-end such as pre-selector selectivity, non-linearity, IQ imbalance, noise, aliasing, spurs and etc.

Note that (3.21) can be re-written using partitioned-matrix form as,

$$\boldsymbol{P_d} = \left[\begin{array}{c|c} \boldsymbol{A} & \dfrac{1}{p_{meas}}\boldsymbol{V} \end{array}\right]\left[\begin{array}{c} \dfrac{\boldsymbol{P_w}}{p_{meas}} \end{array}\right] = \boldsymbol{B}\left[\begin{array}{c} \dfrac{\boldsymbol{P_w}}{p_{meas}} \end{array}\right] \tag{3.23}$$

The measured form of $\boldsymbol{B}$ can be used to develop a single-value metric for the receiver. The measured form of $\boldsymbol{B}$ is given by,

$$\hat{\boldsymbol{B}} = \left[\hat{\boldsymbol{A}} \middle| \frac{1}{p_m} \hat{\boldsymbol{V}} \right] \tag{3.24}$$

A single-value metric of the receiver can be defined in terms of $\hat{\boldsymbol{B}}$ as,

$$\rho = -10 \log_{10} \left(\left\| \hat{\boldsymbol{B}} \right\|_{\infty} - 1 \right) \tag{3.25}$$

where $\| \ \|_{\infty}$ denotes a matrix norm which is equal to the maximum row sum in the matrix. The following observations can be drawn about ρ,

- Note that ρ is large for good receivers ($\rho = \infty$ for an ideal, noise-less receiver), and ρ is small for bad receiver. A receiver with $\rho = \infty$ is expected to always malfunction unless the received spectrum is sparsely occupied.
- This metric quantifies the worst possible signal-to-noise-and-interference-ratio considering the scenario in which signals, with power levels of p_{meas}, are received in each of the *M* sub-bands in the received spectrum.
- However, such type of energetic spectrum scenario is likely to be rare. Hence, the metric should not be used to predict the performance of a receiver in absolute terms. Rather, the metric should be used to compare the performance of two receivers relatively.
- A receiver is *not* guaranteed to perform better than another receiver with a smaller ρ for any given received spectrum scenario. However, if the two receivers are tested in a large number of different received spectrum scenarios, the receiver with higher ρ is going to perform better in average.

- If it is desired to measure the best possible performance of a receiver, ρ should be computed as $\rho = -10\log_{10}\left(\left\|\hat{\boldsymbol{B}}\right\|_0 - 1\right)$, where $\|\ \|_0$ is a matrix norm which is equal to the minimum row-sum in the matrix.

3.5 CSR Signatures for Different Receiver Impairments

CSR based receiver modeling is powerful enough to capture the effects of various receiver impairments. This section presents the signatures of these impairments in the $\boldsymbol{B}$ CSR matrix that is defined in (3.23).

Table 3.1. CSR signatures of Receiver impairments

Impairment	**Description**	**CSR Signature**
No receiver impairment	This receiver exhibits no neighboring-channel interference. The noise floor is also flat.	$\boldsymbol{B} = \begin{bmatrix} 0 & 0 & 0 & 0 & 1 & 0 & 0 & 0 & 0 & 0 & 0 & 0 & 0 & v \\ 0 & 0 & 0 & 0 & 0 & 1 & 0 & 0 & 0 & 0 & 0 & 0 & 0 & v \\ 0 & 0 & 0 & 0 & 0 & 0 & 1 & 0 & 0 & 0 & 0 & 0 & 0 & v \\ 0 & 0 & 0 & 0 & 0 & 0 & 0 & 1 & 0 & 0 & 0 & 0 & 0 & v \\ 0 & 0 & 0 & 0 & 0 & 0 & 0 & 0 & 1 & 0 & 0 & 0 & 0 & v \end{bmatrix}$
IQ imbalance	This receiver exhibits IQ imbalance and a flat noise-floor. The terms α and β denote the image-rejection-ratio at the corresponding sub-bands. Note that $1 > \alpha > v$ and $1 > \beta > v$.	$\boldsymbol{B} = \begin{bmatrix} 0 & 0 & 0 & 0 & 1 & 0 & 0 & 0 & \beta & 0 & 0 & 0 & 0 & v \\ 0 & 0 & 0 & 0 & 0 & 1 & 0 & \alpha & 0 & 0 & 0 & 0 & 0 & v \\ 0 & 0 & 0 & 0 & 0 & 0 & 1 & 0 & 0 & 0 & 0 & 0 & 0 & v \\ 0 & 0 & 0 & 0 & 0 & \alpha & 0 & 1 & 0 & 0 & 0 & 0 & 0 & v \\ 0 & 0 & 0 & 0 & \beta & 0 & 0 & 0 & 1 & 0 & 0 & 0 & 0 & v \end{bmatrix}$

Impairment	Description	CSR Signature
DC offset	This receiver exhibits the same level of IQ imbalance, and aliasing as the previous receiver. However, it also exhibits DC offset in the middle sub-band/middle row. The DC offset is also shown to overshadow the effects of aliasing in the middle sub-band (i.e. the effects of aliasing in the middle sub-band cannot be measured due to the DC offset).	$\boldsymbol{B} = \begin{bmatrix} 0 & 0 & 0 & 0 & 1 & 0 & 0 & 0 & \beta & w & 0 & 0 & 0 & v \\ 0 & 0 & 0 & 0 & 0 & 1 & 0 & \alpha & 0 & 0 & x & 0 & 0 & v \\ 0 & 0 & 0 & 0 & 0 & 0 & 1 & 0 & 0 & 0 & 0 & 0 & 0 & \chi \\ 0 & 0 & x & 0 & 0 & \alpha & 0 & 1 & 0 & 0 & 0 & 0 & 0 & v \\ 0 & 0 & 0 & w & \beta & 0 & 0 & 0 & 1 & 0 & 0 & 0 & 0 & v \end{bmatrix}$
Phase Noise	This is an ideal receiver that exhibits a significant phase noise. The receiver also exhibits a flat noise-floor. Due to phase noise, power is shown to leak between adjacent channels. Generally, $1 > \lambda > \kappa > v$.	$\boldsymbol{B} = \begin{bmatrix} 0 & 0 & 0 & \kappa & 1 & \lambda & 0 & 0 & \lambda & 0 & 0 & 0 & 0 & v \\ 0 & 0 & 0 & 0 & \lambda & 1 & \lambda & 0 & 0 & 0 & 0 & 0 & 0 & v \\ 0 & 0 & 0 & 0 & 0 & \lambda & 1 & \lambda & 0 & 0 & 0 & 0 & 0 & v \\ 0 & 0 & 0 & 0 & 0 & 0 & \lambda & 1 & \lambda & 0 & 0 & 0 & 0 & v \\ 0 & 0 & 0 & 0 & \lambda & 0 & 0 & \lambda & 1 & \kappa & 0 & 0 & 0 & v \end{bmatrix}$
Non-linearity	Receiver overloading is implied if most elements of the CSR matrix are non-zero. Such situation indicates that the power of the signal that is used to measure the CSR matrix, p_{meas}, exceeds the saturation level of the receiver. Such signature may also be used to indicate low-dynamic range.	

3.6 Spectrum Occupancy Model

The last part of this chapter is not regarding the CSR model, but about the spectrum occupancy model that is used to analyze the performance of the cognitive engine and the spectrum sensing mechanisms that are developed in this research (see Section 4.3 and 5.4). This section presents the details of this occupancy model.

This occupancy model applies to dynamic-frequency-allocation based networks. Dynamic-frequency-allocation networks can be defined as those in which frequency allocation for users varies with time. That is, a frequency band that is allocated to one user can be assigned to another user at a later time. DSA and cellular type networks fit well into the definition of dynamic-frequency-allocation networks.

Existing spectrum occupancy models (for example [83, 84]) represent the temporal power level within a given frequency band using a binary value; a value which tells whether the power level is above or below a certain threshold. Such models provide enough information in DSA networks where it generally suffices to know if the primary user is active or not. However, binary representation of spectrum occupancy is not sufficient to capture how energy of the received signal is redistributed in the RF front-end – information crucial in analyses presented in Chapter 3 and 4. Another model [85] assumed that the received power at a given band follows the Gaussian distribution. However, the basis of this assumption is not justified in terms of the physical characteristics of the environment or the attributes of the network.

The model that is developed here is designed to capture the distribution of received power considering the time varying frequency allocation in DSA and cellular networks. If a channel is occupied, the average power of the received signal within the channel is a function of the distance separating the receiver and the transmitter. Therefore, the probability distribution of the average power of received signal is directly related to the probability distribution of the possible positions of different transmitters relative to the receiver.

In this model, the transmission power is assumed to be the same for all transmitters. Networks with flexible transmission power can be fitted to this model by assuming all transmitters use the maximum power at all times. For such cases, the average received power that is estimated by the forthcoming analysis will always be over-estimating the true value.

Assuming log-normal path-loss model [86], it can be shown that the probability distribution of received average power per channel follows truncated-Pareto distribution [87], which is given by the relation in (3.26). It can also be shown that the distribution is exponential in the logarithmic domain. The proof of (3.26) is presented in the dissertation under Appendix C. The probability density function of channel power, p, is given by,

$$pdf_p(x) = \begin{cases} \left(\dfrac{p_m^{2/n_{pl}}}{1 - \left(\frac{p_m}{p_{TX}}\right)^{2/n_{pl}}} \right) \dfrac{2q_{oc}}{n_{pl} x^{1+\frac{2}{n_{pl}}}}, & p_m < x \le p_{TX} \\ 1 - q_{oc}, & p_m = x \\ 0, & otherwise \end{cases} \tag{3.26}$$

where n_{pl} is the path-loss exponent of the propagation environment, p_{TX} is the transmission power, q_{oc} is the probability of channel occupancy, and p_m represents the input referred power level of noise per channel. The plot of the

Cumulative Distributed Function (CDF) which is obtained by setting p_m= -100 dBm, p_{TX} = 23 dBm, n_{pl} = 4, q_{oc} = 1 in (3.26) and integrating it is shown in Figure 3.9.

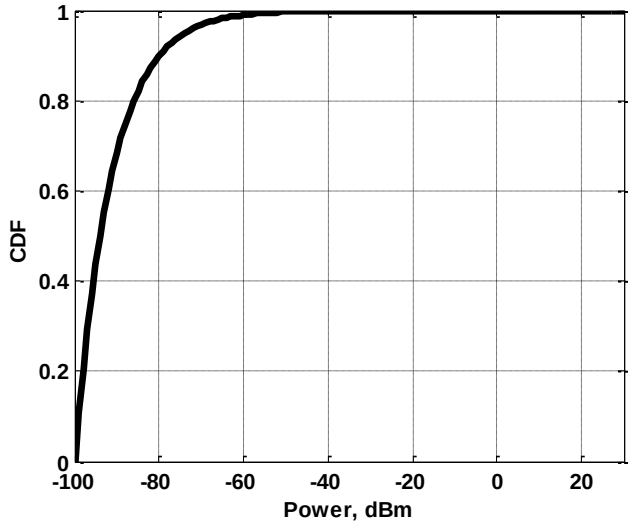

Figure 3.9. CDF of average received power in dynamic frequency allocation network.

This spectrum occupancy model is repeatedly used to measure the performances of the methods that are presented in this dissertation.

3.7 Chapter Summary

This chapter presents a theoretical development of a receiver RF front-end modeling technique called Channelized Spectrum Representation. This model is developed because existing RF front-end models fail to capture the energy re-distribution process in receivers. The chapter shows that mixers, filters, and ADC can be represented linearly using a CSR matrix. These CSR matrix can be used to track the frequency and power-level of signals that are propagating through poorly-selective receivers.

The model is extensively used in this research to design a cognitive engine in Chapter 4, and a spectrum sensing mechanism in Chapter 5. This chapter also showed that CSR can be used to develop a single-value receiver performance metric. Regulatory bodies can use this metric to specify the minimum performance requirement for an interference-protectable receiver. This metric can also be used to easily inform consumers the quality class of the radio receivers they are buying.

The chapter also presented a new stochastic spectrum occupancy model. This model is used in this research to measure the performance of CogRF.

Chapter 4

Cognitive Engine Design for CogRF

CogRF uses Artificial Intelligence (AI) to control the parameters of a flexible RF front-end. CogRF's AI algorithm is housed in an agent called Cognitive Engine (CE). The theoretical design of this CE is presented in this chapter. Section 4.1 outlines the core cognitive features in CogRF. The design in this chapter incorporates most of these features within the CE algorithm. Sections 4.2 and 4.3 present the theoretical development and simulation based experimentation of the CE, respectively.

4.1 The "Cognitive-ness" of CogRF

CogRF contains *cognitive* features that are absent in the *adaptive* RF front-end control mechanisms that are reviewed in Section 1.4.1. Like the adaptive control

mechanisms, CogRF also adapts the RF front-end to the patterns of the environment. Unlike the adaptive algorithms, however, CogRF contains self-awareness and learning capabilities. This makes CogRF a more stable and effective compared to adaptive RF front-end control systems.

The core features in CogRF are described below;

- *Environmental awareness*: The spectrum sensor in CogRF makes the radio aware of its radio environment (state of spectrum occupancy).
- *Intelligent adaption*: CogRF contains intelligent algorithms that adapt the RF front-end to the radio environment based on a pre-defined objective.
- *Learning*: In addition, CogRF monitors the effects of its actions by measuring the performance of the communication link on the desired signal after the RF front-end is reconfigured. The profiles of successful actions are archived for future reference.
- *Self-awareness*: CogRF is aware of the characteristics of the RF front-end under all settings.

As mentioned above, the last two features differentiate CogRF from other adaptive RF front-end mechanisms [38-44]. Adaptive RF front-end control systems are based on a model representing the functional characteristics and properties of the radio environment and the RF front-end. In adaptive RF front-ends, the control mechanism malfunctions if the RF front-end or the radio environment deviates from the presumed model.

Cognitive control mechanisms, however, rely less on models and more on intelligence and awareness. Using the self-awareness capability, CogRF develops the model of the RF front-end "on-the-field." In addition, because of the learning capability in cognitive mechanisms, unsuccessful actions will not be repeated at a

later time. This feature progressively improves the robustness and stability of the mechanism.

Most of the above CogRF features are implemented by the CE. A detailed version of Figure 2.1 is shown in Figure 4.1. The designed CE controls the Local Oscillator's (LO) and the ADC's sampling frequency in receiver RF front-ends. The spectrum sensor measures the occupancy of the spectrum and reports to the CE. The CE also obtains packet-error-rate measurement from the modem to evaluate the outcome of its recent actions. Moreover, the CE contains a self-awareness mechanism that measures the Channelized Spectrum Representation (CSR) model of the receiver RF front-end.

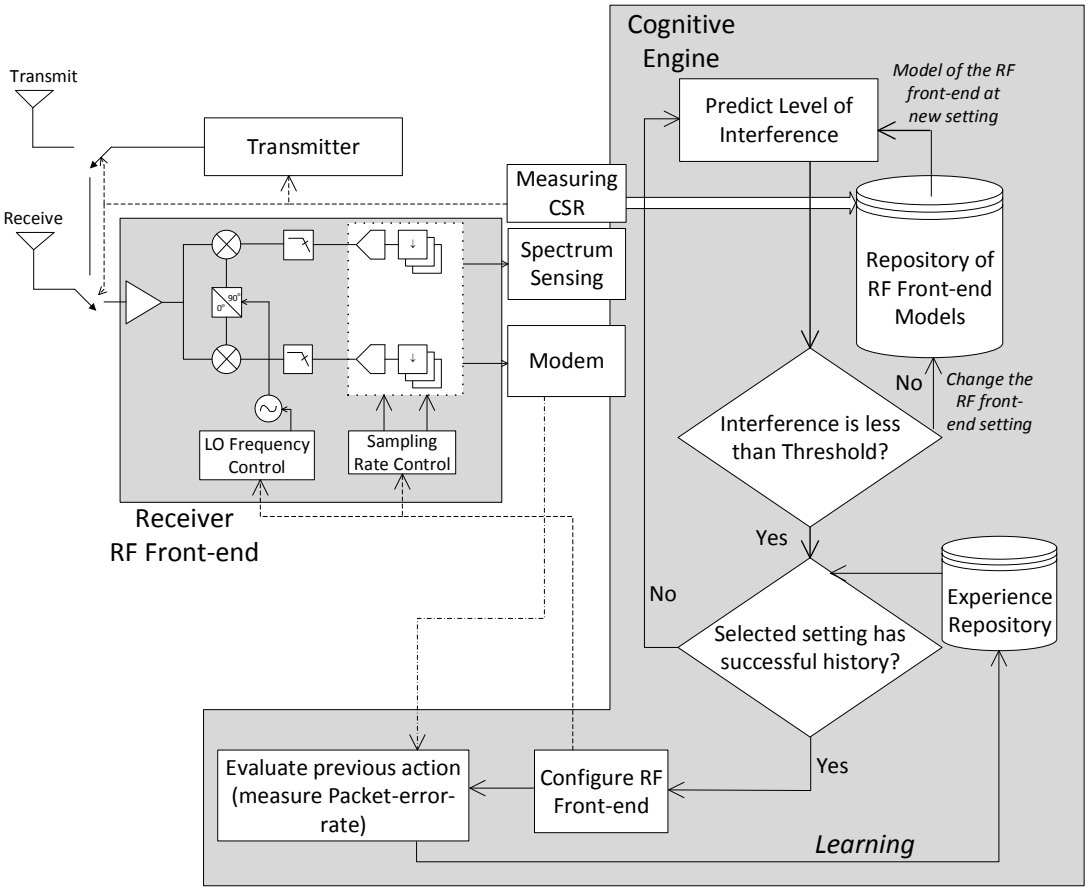

Figure 4.1. Detailed illustration of the designed cognitive engine.

4.2 Theoretical Design

4.2.1 Cognitive Engine Algorithm

As given in (3.19), the CS transform of the receiver transforms CSR of the mixer input to CSR of the ADC output. That is,

$$\boldsymbol{P_d}\left(f_{LO}, f_S\right) = \boldsymbol{A}\left(f_{LO}, f_S\right)\boldsymbol{P_w} + \boldsymbol{V}\left(f_{LO}, f_S\right) \tag{4.1}$$

where the vector $\boldsymbol{V}$ accounts for the power of internally generated signals such as additive noise and spurs. The vectors $\boldsymbol{P_d}$ and $\boldsymbol{P_w}$ are CSR of the receiver input and the ADC output, respectively.

Let the desired channel be the k^{th} channel and the i^{th} channel in the CSR of the signal at the output of the ADC and the input of the mixer, respectively. Then, from (4.1),

$$\begin{aligned} p_d\left(k\,; f_{LO}, f_s\right) &= a_{k,i}\left(f_{LO}, f_s\right) p_w(i) + \sum_{j\neq i} a_{k,j}\left(f_{LO}, f_s\right) p_w(i) + v(k) \\ &= a_{k,i}\left(f_{LO}, f_s\right) p(i) + \eta\left(f_{LO}, f_s, \boldsymbol{P_w}\right) \end{aligned} \tag{4.2}$$

where $a_{k,i}$ represents the element at the k^{th} row and i^{th} column of $\boldsymbol{A}$, and $\eta\left(f_{LO}, f_s, \boldsymbol{P_w}\right)$ represents the undesired power that folds into the desired channel as the signal traverses through the RF front-end. The objective of the CE is to search for the combination of f_{LO} and f_s that insures that $\eta\left(f_{LO}, f_s, \boldsymbol{P_w}\right) < p_{TH}$, where p_{TH} is a predefined threshold. This approach provides a feasible ("good enough") performance within the execution time.

Let i be the index of the channel containing the desired signal at the input of the mixer. If the CS of the signal input to the mixer is modified by removing the power corresponding to the desired channel, the resulting CS is, $\boldsymbol{P}_{w*} = \begin{bmatrix} p_w(1) & p_w(2) & \ldots & p_w(i-1) & 0 & p_w(i+1) & \ldots & \ldots \end{bmatrix}^T$.

From (4.1), the corresponding CS at the output of the ADC sampler is given by,

$$\boldsymbol{P}_{d*}\left(i_{LO}, l_{f_s}\right) = \boldsymbol{A}\left(i_{LO}, l_{f_s}\right)\boldsymbol{P}_{w*} + \boldsymbol{V}\left(i_{LO}, l_{f_s}\right) \tag{4.3}$$

Note that, if $i \geq i_{\mathrm{LO}}$, the index of the desired channel at the input of the mixer maps to the channel with index $k = (i - i_{\mathrm{LO}}) - round\left((i - i_{\mathrm{LO}})/l_{\mathrm{f_s}}\right) \cdot l_{\mathrm{f_s}}$ at the output of the ADC sampler. The operator $round(\ \ )$ finds the nearest integer to a given real number.

Let $L_{\mathrm{f_s}}$ and I_{LO} be sets of the channel indexes of all the possible sampling and LO frequencies of the RF front-end. And let the set,

$$S = \left\{\left(l_{f_s}, i_{LO}\right) : l_{f_s} \in L_{f_s}, i_{LO} \in I_{LO} \text{ and } \boldsymbol{P}_{d*}\left(k; i_{LO}, l_{f_s}\right) \leq p_{TH}\right\} \tag{4.4}$$

The objective of the CE is to find,

$$\left(l_{f_s}^{feas}, i_{LO}^{feas}\right) = \begin{cases} \left\{\left(l_{f_s}, i_{LO}\right) \in S : l_{f_s}^{feas} \leq l_{f_s}, \forall l_{f_s} \in L_{f_s}\right\}, & S \neq \phi \\ \left(l_{f_s}^{\max}, i\right), & S = \phi \end{cases} \tag{4.5}$$

where $l_{\mathrm{f_s}}^{max}$ represents the maximum possible sampling frequency. According to (4.4), the local oscillator frequency can assume any of the possible values as long as the sampling frequency is minimized. Thus, the solution of (4.5) is not necessarily unique.

The intelligence of the CE refers to the capability which allows it to find a feasible setting given by $\left(l_{f_s}^{feas}, i_{LO}^{feas}\right)$. In this research, this aspect is implemented by a simple brute-force search algorithm which attempts every possible combinations starting from the smallest possible $l_{\mathrm{f_s}}$ and i_{LO}. Then, the searching process continues by sequentially increasing $l_{\mathrm{f_s}}$ and i_{LO} until a combination that satisfies the constraint of (4.4) is obtained. Section 4.2.3 shows that a brute-force search algorithm can find a solution within a reasonable duration of time.

Table 4.1lists the algorithm of the CE. The CE receives a reading from the spectrum sensor in line 1 and nullifies the reading in the desired channel to obtain $\boldsymbol{P}_{w^*}$. The condition in line 3 checks if a solution obtained in a previous successful run still applies. The solution still applies if the state of the spectrum has not changed significantly. Using previous successful solutions reduces the average search-time of the CE. If the previous successful solution is obsolete, the CE searches for a new solution. The algorithm halts and returns at line 9 if a solution which satisfies the condition in (4.4) is obtained. The term $\left|L_{f_s}\right|_{\max}$ in line 13 denotes the index in L_{f_s} corresponding to the largest sampling-rate. The term $\left|I_{LO}\right|_{\text{closest}}$ in line 13 denotes the index in I_{LO} that corresponds to the LO frequency closest to the desired signal's channel. If a solution could not be obtained during the search process, the algorithm uses the default solution, $\left(\left|L_{f_s}\right|_{\max}, \left|I_{LO}\right|_{\text{closest}}\right)$.

After the search process is completed and the RF front-end is reconfigured, the CE evaluates its actions by obtaining the packet-error-rate on the desired signal from the modem (see Figure 4.1). An action is stated to be successful if the packet error rate is below a programmable threshold. The profile of a successful action,

which includes the associated spectrum reading and the selected RF front-end settings, is achieved in the experience repository of the CE.

Table 4.1 Searching algorithm in the cognitive engine.

Inputs:

- $\left(l_{f_s}^{feas}, i_{LO}^{feas}\right)$ from experience repository (output of a successful previous action)
- $\boldsymbol{P}_{w*}$ from spectrum sensing
- $\boldsymbol{A}\left(i_{LO}, l_{f_s}\right)$ for all possible $\left(i_{LO}, l_{f_s}\right)$

Output: $\left(l_{f_s}^{opt}, i_{LO}^{opt}\right)$

compute $\boldsymbol{P}_{w*}$ from $\boldsymbol{P}_{w}$
compute $\boldsymbol{P}_{d*}\left(i_{LO}, l_{f_s}\right)$
if $\boldsymbol{P}_{d*}\left(k; i_{LO}, l_{f_s}\right) > p_{TH}$
  iterate j through elements of L_{f_s}
    iterate i through elements of I_{LO}
      compute $\boldsymbol{P}_{d*}\left(k; j, i\right)$
      if $\boldsymbol{P}_{d*}\left(k; j, i\right) < p_{TH}$ **and** setting $\left(j, i\right)$ has history of success
        $\left(l_{f_s}^{feas}, i_{LO}^{feas}\right) = \left(j, i\right)$
        return $\left(l_{f_s}^{feas}, i_{LO}^{feas}\right)$
      end if
    end repeat
  end repeat
  $\left(l_{f_s}^{feas}, i_{LO}^{feas}\right) = \left(\left|L_{f_s}\right|_{\max}, \left|I_{LO}\right|_{\text{closest}}\right)$
  return $\left(l_{f_s}^{feas}, i_{LO}^{feas}\right)$
else
  return $\left(l_{f_s}^{feas}, i_{LO}^{feas}\right)$
end if

4.2.2 Performance Limit

This sub-section presents a theoretical limit of the designed CE. Assume the ADC has attenuation level of Q_u in the $(u+1)^{th}$ Nyquist zone. Similarily, the baseband filter is assumed to have attenuation level of $|H_u|^2$ in the $(u+1)^{th}$ Nyquist zone[8]. The mixer is assumed to have image rejection ratio of β at all frequencies. The pre-selector filter is assumed to have an infinite bandwidth. Based on these assumptions, (4.2) can be rewritten as[13],

$$p_d(k) = \sum_{u=-b}^{b} Q_u |H_u|^2 \left\{ p_w\left(k - ul_{f_s} + i_{LO}\right) + \beta p_w\left(k - ul_{f_s} - i_{LO}\right) \right\} \tag{4.6}$$

and b approaches infinity since the radio is assumed to have no filtering. This formula is simply stating that the power contained in a channel at the output of the ADC is a sum of the power of aliased and image signals. The power of image signals is scaled by the image-rejection ratio (β), and the power of aliased signals is scaled by the attenuation level of the corresponding Nyquist zone $Q_u |H_u|^2$.

From (4.6), if no signal is being received, the average undesired power folded into the desired sub-band at the output of the ADC is due to noise only. It is given by,

$$p'_m = p_m (1+\beta) \sum_u Q_u |H_u|^2 \tag{4.7}$$

where, p_m represents the input referred power level of noise per channel (input referred noise-floor). Accordingly, for a given RF front-end, p'_m is the theoretical minimum of the undesired signal power contained in any channel at the output of

[8] The baseband filter's response is not constant through the span of a given Nyquist zone. The attenuation level of a given zone is approximated by the response of the filter in the middle of the zone.

the ADC. Because of the infinite-pre-selector-bandwidth assumption, however, p'_m is only a lower bound for the actual limit.

For example, assume the ADC is impulsive-sampling ($Q_u = 1$ for all u) and $\beta = -10$ dB for the mixer. The baseband filter is second order Butterworth filter with a cut-off frequency equal to half of the sampling frequency. For this RF front-end, it can be shown that $p'_m / p_m \approx 1.0$ dB [13].

Noting that p_m is the sensitivity level of perfectly-selective receiver, this result indicates that the cognitive engine may improve the sensitivity of a poorly-selective receiver to be within $10\log_{10}\left(p'_m / p_m\right)$ dBs of a highly-selective filter's sensitivity. However, the cognitive engine can never find a solution which can do better than this limit. It should also be noted that the value of this limit is a dependent on characteristics of the RF front-end elements.

4.2.3 Feasibility of Searching-based Cognitive Engine

Implementing a CE using a search algorithm potentially makes it slow. This sub-section attempts to address this concern by statistically analyzing the number of steps the CE takes to find a solution. The computational complexity of the CE algorithm is also analyzed in this sub-section.

Under the independent trial assumption (the images of the desired channel are a different set at each trial), the number of steps the CE takes to obtain a solution is geometrically distributed [88, 89]. Therefore, the CE will find a solution within (also see (4.13)),

$$N_C < \frac{ln(1-C)}{ln\left(1-Pr\left\{p_d(k) \le p_{TH}\right\}\right)} \tag{4.8}$$

steps[9]; where C represents the degree of confidence; and $Pr\{\ \}$ denotes probability operator. Note that $N_C \to \infty$ as $p_{TH} \to p'_m$.

Figure 4.2 presents a plot of N_C versus p_{TH} for different degrees of confidence. The plot is obtained by first computing $Pr\{p_d(k) \le p_{TH}\}$ using Monte Carlo simulation of (4.6) with $b = 201$; and assuming p_w follows the distribution in (3.26)[10] with $p_{TX} = 30$ dB, $p_m = -100$ dBm, $n_{pl} = 4$, and $q_{oc} = 0.8$. In this analysis, a natural-sampling ADC, with 50% duty-cycle is assumed; and both the pre-selector and the baseband filter are assumed to have infinite bandwidth. The mixer is assumed to have 0 dB image rejection. For this RF front-end, the $10\log_{10}(p'_m / p_m) = 4.8$ dB [89].

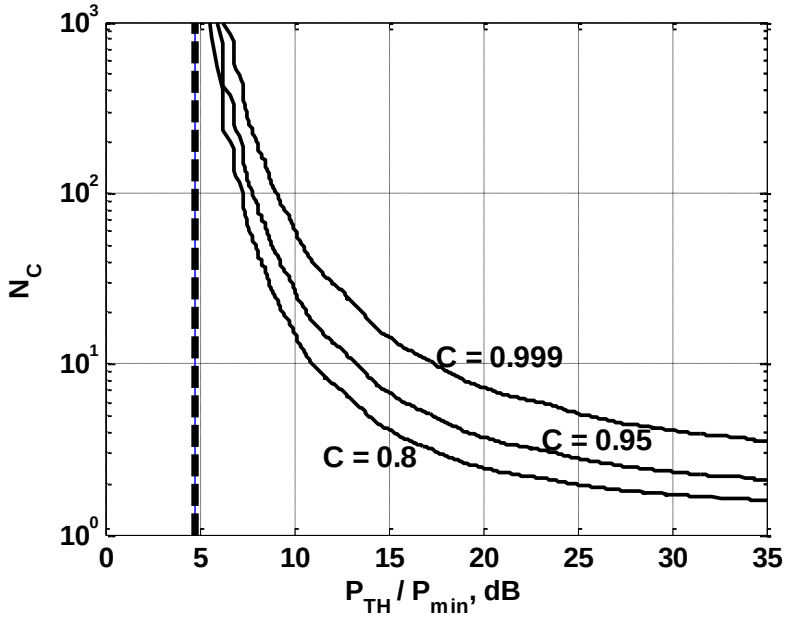

Figure 4.2. The number of steps the CE takes to obtain a solution.

[9] As stated above, note that N_C is an upper bound on the actual number of independent steps the CE takes to find a solution.

[10] See Section 3.5 for definitions of p_m, p_{TX}, n_{pl}, and q_{oc}

The result shows that the CE can find a solution within reasonable number of steps (less than 1000) even for extreme p_{TH}/p_m with significant confidence. If there are M channels in the received spectrum, then, each search trial in the CE algorithm involves a step at which two $M \times 1$ vectors are multiplied (line 6 in Table 4.1). The same type of vector multiplication is also carried out during the initialization of the algorithm (line 2). Each of these vector multiplications need M multiplication and $M-1$ addition operations (total of $2M-1$ operations).

Then, for non-parallelized system containing a single multiplier and a single adder, the time duration the CE takes to obtain its solution with C degree of confidence can be approximated by,

$$T_{CE} \approx (N_C + 1)(2M - 1) / f_{clock} \tag{4.9}$$

Accordingly, it can be concluded that the complexity of the CE algorithm in increases linearly with respect to M. If the span of the spectrum is 100 MHz, and the width of the channels is set to be 2 MHz, it can be shown that $T_{CE} < 0.5\ ms$ for $N_C < 1000$ and $f_{clock} = 100$ MHz. This indicates that it is feasible to implement the CE as a brute-force search algorithm even when the span of the spectrum of interest is very wide.

4.2.4 Theoretical Performance Comparison

The performance of a CogRF is compared against conventional RF front-end topologies. Three types of RF front-ends are considered in this analysis. The first one is a traditional receiver containing a brick-wall pre-selector filter that passes only the desired signal into the receiver. The second is also a traditional radio with no pre-selector filter. Like the second one, the third RF front-end does not contain a pre-selector filter. However, it incorporates the CE developed in this chapter. All

the three RF front-ends contain a second order anti-aliasing Butterworth baseband filter whose cut-off frequency is always half of the sampling frequency. The mixers in all the RF front-end were assumed to have -10 dB image rejection capability and all ADCs were also assumed to produce no filtering (impulsive ADCs are assumed). Furthermore, the received power in each channel is assumed to follow the distribution given in (3.26).

The metric for evaluating the RF front-ends is given by,

$$q = Pr\{x < p_{TH}\} \tag{4.10}$$

where x is a random variable representing the amount of undesired power contained in a desired channel at the output of the ADC.

Since the first type RF front-end is highly selective, the undesired power contained in the desired channel corresponds to noise only. Hence, it can be easily shown that,

$$q_1 = \begin{cases} 1, & p_{TH} > p_m \\ 0, & p_{TH} \le p_m \end{cases} \tag{4.11}$$

For the second type of RF front-end, the probability that the undesired power within of a given RF front-end setting is less than p_{TH} can be computed using (4.6) as,

$$q_2 = Pr\{p_d(k) \le p_{TH}\} \tag{4.12}$$

If CE is in use, multiple settings are tested before the RF front-end is reconfigured. The search for an RF front-end setting in which the undesired power is below a given threshold is a Bernoulli trial experiment. Hence, the probability

of finding an RF front-end setting for which the undesired power is below p_{TH} is given by,

$$q_3 = 1 - \left(1 - Pr\left\{p_d(k) \le p_{TH}\right\}\right)^N \tag{4.13}$$

where N is the number of independent CE trials.

Figure 4.3 compares the performance metrics obtained for the different types of RF front-ends in (4.11), (4.12) and (4.13). The plots are obtained by setting $p_{TX} = 23$ dBm, $p_m = -100$ dBm, $n_{pl} = 4$, and $q_{oc} = 0.8$.

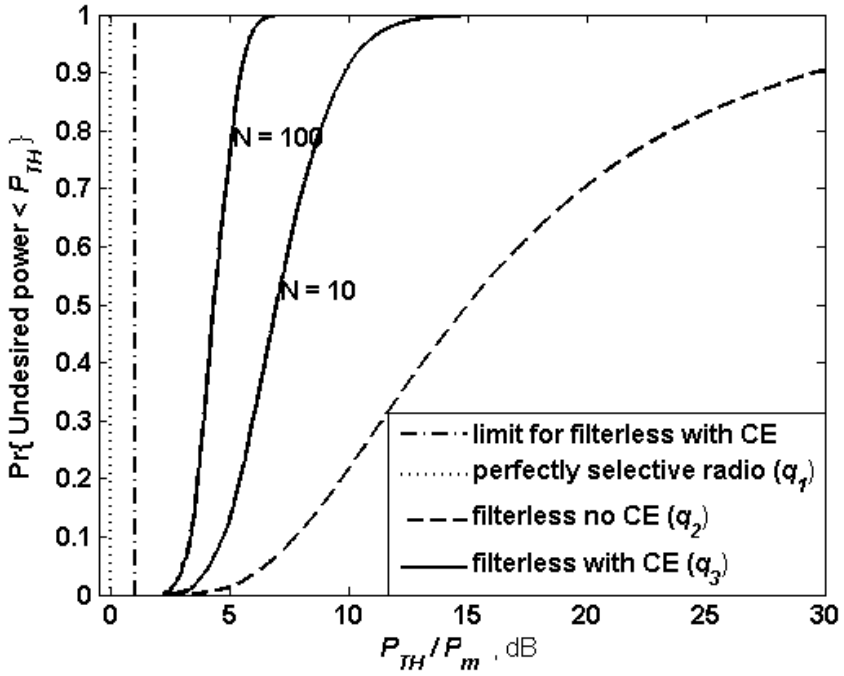

Figure 4.3. Comparison in terms of probability of undesired power being less than p_{TH}, ($p_m = -100$ dBm). [Copyright permission is provided under Appendix F]

The CE pushes the curves of the filterless RF front-end (no pre-selector) towards the curve of the perfectly selective RF front-end. This implies that an RF front-end with no pre-selector filter can behave similar to a perfectly selective RF front-end

by incorporating the proposed CE. The benefit of the CE is significant for the low p_{TH}/p_m region. For example, a filterless radio achieves a $p_{TH}/p_m = 10$ dB performance almost 100% of the time if the 100 step CE is employed. This can be compared to the fact that $p_{TH}/p_m = 10$ dB performance is achieved only 10% of the time if the CE is not employed.

The CE is also expected to improve capacity because it reduces the average amount of undesired power in the desired channel. Modeling the undesired power folding into the desired channel as an additive white Gaussian noise and assuming the CE finds the optimal RF front-end setting instantaneously, the capacity that is achieved 80% of the time is given for the different type of radios using Shannon's formula [76] as, $C^{0.8} = \log_2\left(1 + p_{sig}/p_{TH}^{0.8}\right)$. The term $p_{TH}^{0.8}$ is obtained from (3.26) by letting $Pr\{x \leq p_{TH}^{0.8}\} = 0.8$. The term p_{sig} represents the average power of the desired signal.

From Figure 4.3, $P_{TH}^{0.8}$ is -100 dBm for perfectly selective radio. For filterless radio with no CE, $p_{TH}^{0.8}$ is -76.6 dBm. For the filterless radio with the CE, $p_{TH}^{0.8}$ is -94.8 dBm for 100 step CE, and -91.2 dBm for a 10 step CE. The 80% achievable capacity ($C^{0.8}$) for the three types of radios is plotted in Figure 4.3.

According to Figure 4.4, a 100 step CE allows a filterless RF front-end to have a capacity performance within 1 bit of a perfectly selective RF front-end. Similarly, a 10 step CE allows a filterless RF front-end to have a capacity performance within 2 bits of a perfectly selective RF front-end. This shows that CE can improve performance of poorly-selective receiver RF front-ends without requiring improvement in the actual selectivity.

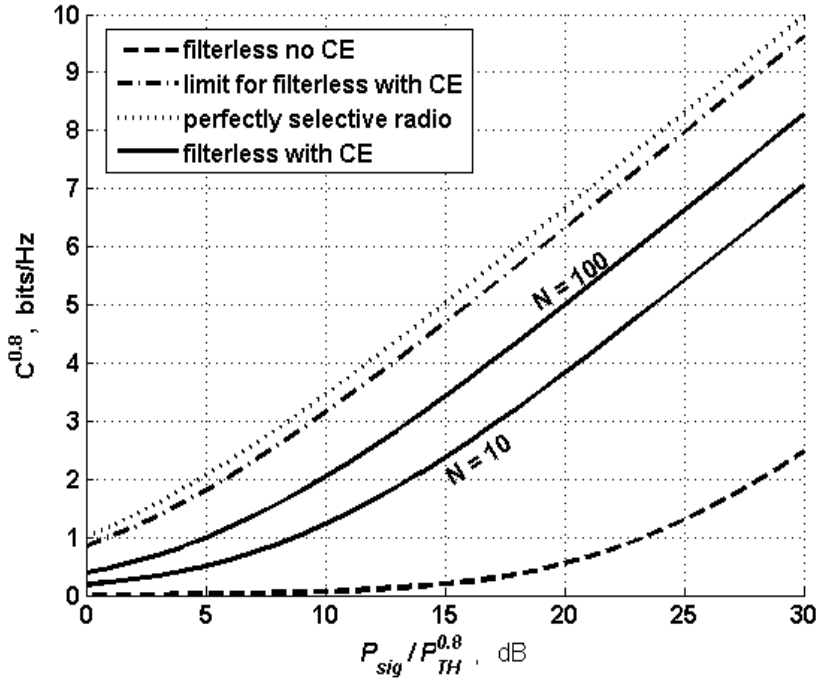

Figure 4.4. Comparison in terms of a capacity metric. [Copyright permission is provided under Appendix F]

4.3 Simulation based Evaluation of CogRF

The previous section analyzed the benefit of the CE in an RF front-end that has no pre-selector filter. In this section, the benefits of the CE are analyzed using a CSR-domain simulation of more realistic RF front-ends. Three types of RF front-ends are compared in this simulation. Except the selectivity of their pre-selector filters, all the parameters of the three RF front-ends are set to be the same. The parameters used in this simulation are presented in Table 4.2.

.

Table 4.2 Simulation parameters.

Element	**Value/Type**
Pre-selector filter	Brick-walled
LNA	IIP3 = -10 dBm
Mixer	Image rejection = -10 dB
Baseband filter	2^{nd} order Butterworth, 3-dB bandwidth equals to half of sampling rate
ADC	Has no filtering effect
Transmission power (p_{TX})	23 dBm
Path-loss exponent (p_m)	-100 dBm
Noise floor at receiver (n)	4
Probability of spectrum occupancy	0.8
Span of input spectrum	600 MHz – 1400 MHz
Channel bandwidth	1 MHz

The pre-selector filter selectivity of 30%, 10% and 1% are considered. The probability that undesired power in a desired channel exceeds a threshold (complement of the metric in (4.10)) is used as a metric to compare the three RF front-ends. This metric loosely represents the probability of outage on the desired communication. The simulation also compared the performance of the RF front-ends with and without the CE.

A spectrum data of 500 time steps was generated using the distribution in (3.26). The desired channel was set to be at 1 GHz. The possible LO frequencies were ranging from 999 MHz, 997 MHz, 995 MHz, and 993 MHz. The possible sampling frequencies were 2 MHz, 4 MHz, 6 MHz and 8 MHz.

The simulation was run for p_{TH} = -98.5 dBm, -95.0 dBm and -85.0 dBm. The probability that undesired power within the desired channel exceeds p_{TH} was measured in the simulation over 500 time steps. This value corresponds to the

probability of communication outage on the desired signal. The results of the experiment are presented under Table 4.3.

Table 4.3. The probability that undesired power within a desired band exceeds p_{TH}.

Pre-selector Bandwidth	Five step cognitive engine			Without cognitive engine		
	$\frac{p_{TH}}{p_m}$=1.5dB	$\frac{p_{TH}}{p_m}$=5.0dB	$\frac{p_{TH}}{p_m}$=15.0dB	$\frac{p_{TH}}{p_m}$=1.5dB	$\frac{p_{TH}}{p_m}$=5.0dB	$\frac{p_{TH}}{p_m}$=15.0dB
30%	0.68	0.31	0.02	0.94	0.65	0.31
10%	0.66	0.31	0.02	0.94	0.64	0.31
1%	0.12	0.31	0.02	0.83	0.54	0.15

According to the result in Table 4.3, the CE enabled the RF front-end with 30% selectivity to perform better than a traditional RF front-end with 1% pre-selector selectivity. For example, the undesired power exceeds -98.5 dBm is 94% of the time for the RF front-end with 30% pre-selector selectivity. This indicates the RF front-end will have a high rate of communication outage. This rate lowers to 68% if CE is employed and to just 83% if selectivity is increased to 1%.

The results in Table 4.3 confirm the assertion that an RF front-end with poorly-selective pre-selector filter can obtain performance level similar to a highly selective RF front-end by incorporating the designed CE. In addition, the results also indicate that the proposed CE can improve performance even when selectivity of the pre-selector filter is relatively high.

4.4 Chapter Summary

This chapter presents the formulation and theoretical design of a CE that controls the LO and sampling frequency of receiver RF front-ends. The CE is

implemented using a simple brute-force searching based algorithm. This chapter also presents a theoretical analysis to justify the use of brute-force based CE. The result shows that the CE can find its solutions in millisecond time frame even for receivers whose reception bandwidth is in the order of 100 MHz or more.

The results presented in this chapter showed that the performances of a poorly-selective receiver can be improved by employing the designed CE to control the frequency-plan of the receiver. In other words, the CE allows a poorly-selective receiver to perform similar to a highly-selective receiver without using an actual filter. A 100 step CE is shown to allow a pre-selector-less RF front-end to have a capacity performance within 1 bit of a perfectly-selective RF front-end. A 5 step CE is also shown to improve the rate of outage from 65% to 31% for a poorly selective receiver. This rate lowers just to 54% if the actual selectivity is of the receiver is increased by a factor of 30 without incorporating the CE. It is also shown that the CE can enhance the performance of a highly-selective receiver as well.

Chapter 5

Spectrum Sensing Design for CogRF

5.1 Introduction

Spectrum sensing is has been explored extensively [90-99]. However, this research presents practical problems that have not been addressed in previous spectrum sensing research.

Derived by the application of CogRF in dynamic spectrum access and mmWave technologies, the overall receiver, including the one that is used for sensing purposes, is assumed to be poorly-selective. As described in Chapter 1, poorly-selective receivers are vulnerable to receiver impairments such as IQ imbalance and aliasing. These impairments can degrade the accuracy of the

spectrum sensing. This chapter presents a spectrum sensing method that has enhanced performance in the presence of IQ imbalance and aliasing.

Moreover, unlike other cognitive radios which employ detection-based spectrum sensing [91, 95] to determine just the absence or presence of a signal, CogRF requires an estimation of the actual power level in all neighboring-channels (see the cognitive engine algorithm in Table 4.1). The cognitive engine selects an RF front-end setting as a solution if the setting allows for limiting the level of interference to be under a given threshold. The cognitive engine computes the level of interference corresponding to a given RF front-end setting through analytical computation – not actual measurement. The cognitive engine computes the level of interference in any channel by weighting-and-summing the power levels in the neighboring-channels (see Chapter 3). Accordingly, the cognitive engine has to first obtain the estimate of the actual power within each neighboring-channel to predict the interference level. The cognitive engine obtains the actual power level in neighboring-channels from an estimation-based spectrum sensor. This chapter presents an estimation-based multi-band spectrum sensing method for CogRF.

Different techniques are used to implement multi-band spectrum sensing. The most well-known technique is Nyquist sampling based spectrum sensing (Nyquist-sensing) [96]. There have been some studies regarding the effects of receiver impairments on detection-based Nyquist-sensing. Verlant-Chenet *et. al* [92] studied the impacts of IQ imbalance and sampling clock offset on both single-band energy-detection and single-band cyclostationary-features-based sensing. More recently, Gokceoglu *et. al* [98] developed a scheme that eliminates the effects of IQ imbalance on multi-band energy detection based spectrum sensing. In addition, Rebeiz *et. al* [93] analyzed the effect of third-order RF non-linearities on energy-

detection and cyclostationary-features-based wideband sensing. Furthermore, Grimm *et. al* [100] presented analysis and digital mitigation of IQ imbalance, RF non-linearity distortion and baseband non-linearity distortion on multi-band spectrum sensing.

If the sensed spectrum bandwidth is large, for example, in the order of 100 MHz, Nyquist-sensing may not be a feasible option because it requires high performance analog-to-digital-convertors (ADCs). To reduce the sampling rate requirement, compressive-sampling-based sensing (compressive sensing) can be employed [90, 94, 97]. Compressive sensing allows sampling at sub-Nyquist rates by leveraging sparsity in spectrum occupancy. However, the sparsity assumption makes compressive sensing impractical for sensing densely or moderately occupied spectrum. Another solution is the use of analog filter-bank that contains multiple tuned filters for different sections of the monitored spectrum [97, 99]. The output of each filter is independently down-converted and sampled using a low-rate ADC. However, this technique results in high hardware complexity as the number of bands increases.

The other alternative is the serial multi-band spectrum sensing (S-MSS) [97] which is also referred as sweeping-based sensing [96]. In S-MSS, only a subset section of spectrum is measured at a time and the overall spectrum is sensed by stepping through serious of sections by tuning the local oscillator (LO) frequency of the sensing receiver. Compared to a Nyquist-sensing and compressive sensing, S-MSS is known to be slow [96] mainly due to the slowness of the LO tuning speed and the probability of missing signals while scanning other bands. However, if the slow tuning speed can be tolerable, S-MSS is the most affordable technique to implement multi-band spectrum sensing in conventional CRs. In addition, new

types of LO architectures utilizing direct-digital-synthesis are proposed [59]. These can provide better tuning speed for S-MSS receiver.

Even though its implementation is simple, S-MSS also suffers from errors produced by receiver imperfections, including IQ imbalance and aliasing. The method proposed in this chapter can correct for both IQ imbalance and aliasing by collectively observing the raw data output from measuring all the sections in S-MSS. This method is called *robust S-MSS* (RS-MSS) because it is tolerant against IQ imbalance and aliasing. Furthermore, the proposed method can also be used to address other types of imperfections such as spurs and higher-order harmonic down-conversions.

5.2 CSR of Serial Multi-band Spectrum Sensing

An S-MSS senses only a section in the spectrum at a time; and steps through multiple sections by changing its LO frequency [97]. The state of the spectrum is assumed to stay constant during one S-MSS measurement cycle.

Consider a spectrum containing N channels, and S-MSS sub-divides these into N_{SEC} sections - sensing one section at a time. Each section contains s channels. This can be formulated using CSR domain as,

$$\begin{bmatrix} \boldsymbol{P_d}\left(f_{LO,1}, f_S\right) \\ \boldsymbol{P_d}\left(f_{LO,2}, f_S\right) \\ \vdots \\ \boldsymbol{P_d}\left(f_{LO,N_{SEC}}, f_S\right) \end{bmatrix} = \begin{bmatrix} \boldsymbol{A}\left(f_{LO,1}, f_S\right) \\ \boldsymbol{A}\left(f_{LO,2}, f_S\right) \\ \vdots \\ \boldsymbol{A}\left(f_{LO,N_{SEC}}, f_S\right) \end{bmatrix} \boldsymbol{P_w} + \begin{bmatrix} \boldsymbol{V}\left(f_{LO,1}, f_S\right) \\ \boldsymbol{V}\left(f_{LO,2}, f_S\right) \\ \vdots \\ \boldsymbol{V}\left(f_{LO,N_{SEC}}, f_S\right) \end{bmatrix} \tag{5.1}$$

Note that sampling-rate, f_S, is assumed to be the same for all sections, and $f_S = s\Delta$, where Δ is the channel bandwidth (see Section 3.2.5). Consider $\breve{\boldsymbol{A}}$ is a $sN_{SEC} \times N$ matrix formed by concatenating $\boldsymbol{A}$ matrix corresponding to N_{SEC} different LO frequencies. This matrix is referred as *multi-LO-CS transform* of the receiver. Similarly, $\breve{\boldsymbol{P}}_{\boldsymbol{d}}$ and $\breve{\boldsymbol{V}}$ are both $sN_{SEC} \times 1$ vectors formed by concatenating $\boldsymbol{P_d}$ and $\boldsymbol{V}$, respectively. The vector $\breve{\boldsymbol{V}}$ is referred as the *multi-LO-zero-input CS response* of the receiver. Accordingly, (5.1) can be re-written as,

$$\breve{\boldsymbol{P}}_{\boldsymbol{d}} = \breve{\boldsymbol{A}}\boldsymbol{P_w} + \breve{\boldsymbol{V}} \tag{5.2}$$

The CSR model in (5.2) is a compact way to track how energy is redistributed as signal propagates through a non-ideal receiver. The next section shows how the CSR model is used to develop an accurate multi-band spectrum sensing mechanism.

5.3 Robust Serial Multi-band Spectrum Sensing

5.3.1 Mechanism Concept

The objective of energy-measurement-based multi-band spectrum sensing is to estimate the CSR (see Section 3.2) of a receiver input. However, the DSP that carries out the computation of spectrum sensing can observe the CSR of the ADC output only. In practical radio receivers, however, CSR of the ADC output may not be accurate depiction of CSR of the receiver input due to radio imperfections.

As it was discussed previously, IQ imbalance and aliasing re-distribute the signal energies inside the receiver. The model given in (5.2) easily captures how

energy is redistributed inside the receiver. The state of the spectrum at the receiver input can be estimated from the CSR of the ADC output and the reverse of the RF fromt-end model. In other words, the mechanism estimates for $\breve{\boldsymbol{P}}_{\boldsymbol{w}}$ in (5.2) given $\breve{\boldsymbol{P}}_{\boldsymbol{d}}$, and prior knowledge of $\breve{\boldsymbol{A}}$ and $\breve{\boldsymbol{v}}$.

The next sub-section briefs how CSR of the ADC output is measured in this research. Then, the following sub-section presents the theoretical design of the proposed sensing mechanism.

5.3.2 Measuring CSR of the ADC output

Either digital filter banks or windowed fast-frequency-transform (FFT) can be used to measure CSR [72]. In this research, Blackman-windowed FFT is used to measure CSR of the ADC output. The Blackman window is selected because it has side-lob levels lower than most other known windowing functions [75]. Despite its low side-lob levels, the Blackman window is also known to have relatively wider main-lob. For this reason, the windowing can introduce leakage between adjacent-channels unless the size of the FFT and the window is increased to over-sample the signal.

The width of the main lob for a Blackman window is approximated to be equal to $12\pi/N_{FFT}$, where N_{FFT} is the size of the window (or the size of the FFT) [75]. The size of the window should be large enough to constrain the main lob within the channel bandwidth. This minimizes the leakage between neighboring-channels during CSR measurements. That is,

$$\frac{12\pi}{N_{FFT}} < \frac{\Delta}{f_s} = \frac{1}{N_{sb}} \tag{5.3}$$

where N_{sb} is the number of channels in the first Nyquist zone. Hence, to satisfy the condition in (5.3), $N_{FFT} > 12\pi N_{sb}$.

Accordingly, multiple FFT samples fall within one channel. The average power in a channel is computed by averaging both across frequency and time. First the magnitude-squares of all the FFT samples within a channel are averaged. Then, time-domain averaging is carried out across multiple FFT periodograms of the signal [75].

5.3.3 Estimator Design

This sub-section presents an approximately maximum-likelihood estimator that is designed to obtain the CSR of the receiver input given the CSR of the ADC output. FFT perediograms are used to measure the CSR of the ADC output.

Needless to say, measurement error is inevitable in CSR measurement of the ADC output. Hence, using (5.2), the *measured* CSR of the ADC output can be given by,

$$\breve{\boldsymbol{P}}_{\boldsymbol{d,m}} = \breve{\boldsymbol{A}}\boldsymbol{P}_{\boldsymbol{w}} + \breve{\boldsymbol{V}} + \boldsymbol{W} \tag{5.4}$$

where $\boldsymbol{W}$ is an $sN_B - by - 1$ vector and it represents measurement error. Consider, $\boldsymbol{Z} = \breve{\boldsymbol{P}}_{\boldsymbol{d,m}} - \breve{\boldsymbol{V}}$, then,

$$\boldsymbol{Z} = \breve{\boldsymbol{A}}\boldsymbol{P}_{\boldsymbol{w}} + \boldsymbol{W} \tag{5.5}$$

The objective is to obtain $\hat{\boldsymbol{P}}_{\boldsymbol{w}}$, the estimate of $\boldsymbol{P}_{\boldsymbol{w}}$.

Understanding the statistical distribution of $\boldsymbol{W}$ is important to properly design the estimator. Assuming the true average power corresponding to the j^{th} element of $\boldsymbol{Z}$ is given by $z_t[j]$, and assuming periodogram based CSR measurement is used,

it can be shown that the distribution of the measurement error in the j^{th} element is normally distributed with zero mean and variance given by $\sigma_j^2 = \left(z_t[j]\right)^2 \big/ \left(2N_p\right)$; where N_p is the number of periodograms used in the measurement. (Please see Appendix D for proof.)

Accordingly, the maximum likelihood (weighted least-squares) estimator of $\boldsymbol{P_w}$ minimizes,

$$\hat{\boldsymbol{P}}_{\boldsymbol{w}} = \arg\min_{\boldsymbol{P_w}} \sum_{j=1}^{sN_B} \left(\frac{z[j] - \breve{\boldsymbol{a}}_j \boldsymbol{P}_{\boldsymbol{w}}}{z_t[j]} \right)^2 \tag{5.6}$$

where $\breve{\boldsymbol{a}}_j$ represents the j^{th} raw of $\breve{\boldsymbol{A}}$ and $z[j]$ represents the j^{th} element in $\boldsymbol{Z}$. However, because the true value $z_i[j]$ is not known, it is approximated by $z[j]$. Then, the estimator in (5.6) becomes,

$$\hat{\boldsymbol{P}}_{\boldsymbol{w}} = \arg\min_{\boldsymbol{P_w}} \sum_{j=1}^{sN_B} \left(\frac{z[j] - \breve{\boldsymbol{a}}_j \boldsymbol{P}_{\boldsymbol{w}}}{z[j]} \right)^2 \tag{5.7}$$

This estimator is a relative-error least-squares [101] type because it normalizes the square of observed errors with the corresponding elements of the observation vector. This feature has a practical value in the CSR measurement. Noting that the elements of the observation vector ($\boldsymbol{Z}$) can have very high dynamic range; the normalization ensures that strong signals do not overshadow the weak signals in the operation of the estimator.

To illustrate this assertion, consider a CSR measurement of a spectrum containing a -20 dBm signal and a -80 dBm signal in Table 5.1. The table compares relative and absolute errors in milliwatt scale assuming ±1dB measurement error on both signals.

Table 5.1. Normalizing error.

Power in dBm		Power in Milliwatt[11]		Absolute error in Milliwatt	Relative error in Milliwatt
True	Measured	True	Measured		
-20	-19	0.01	0.0126	0.0026	0.2057
-80	-79	1e-8	1.26e-8	2.59e-9	0.2057
-20	-21	0.01	0.0079	0.0021	0.2589
-80	-81	1e-8	7.94e-9	2.06e-9	0.2589

It can be observed that the absolute errors have six orders of magnitude difference. On the other hand, the relative errors in milliwatt scale have comparable values similar to the absolute error in dB scale. Accordingly, the error in the -20 dBm signal does not overshadow the error in the -80 dBm signal when relative-error based estimator is employed.

The estimator in (5.7) can be re-written in more compact form as;

$$\hat{\boldsymbol{P}}_{\boldsymbol{w}} = \left(\breve{\boldsymbol{A}}^T \boldsymbol{R}^{-1} \breve{\boldsymbol{A}}\right)^{-1} \breve{\boldsymbol{A}}^T \boldsymbol{R}^{-1} \boldsymbol{Z} \tag{5.8}$$

where $\boldsymbol{R} = diag\left(z[0]^2, z[1]^2, \ldots, z[sN_B - 1]^2\right)$.

To avoid the computational burden of matrix inversion in (5.8), a simpler iterative algorithm is used to solve (5.8). Leveraging the non-negativity of $\breve{\boldsymbol{A}}$, $\boldsymbol{Z}$ and $\boldsymbol{P}_{\boldsymbol{w}}$, sequential coordinate-wise algorithm (SCA) for non-negative least squares (NNLS) [102] is used to implement the estimator. SCA is preferred due to its simplicity, compared to other traditional active-set-based NNLS algorithms [103]. Its simplicity makes the algorithm favorable for hardware implementation. SCA adapted from [103] for spectrum sensing is presented in Table 5.2.

Because this algorithm minimizes the effects of IQ imbalance and aliasing from the raw spectrum sensing data, it is referred as *robust S-MSS* (RS-MSS).

[11] The values shown under these columns are approximated to the fourth decimal. The actual values that are used to compute the values under the last column are more accurate (double-precision in MATLAB).

However, the RS-MSS assumes prior knowledge of the CSR model of the receiver RF front-end. The next sub-section presents a mechanism that can be used to measure the CSR model of a receiver.

Table 5.2 Algorithm of the designed estimator.

Notation: $\zeta = \{1,2,\cdots,n\}$, $\zeta_k = \zeta / k$, $\boldsymbol{H} = \left(\breve{\boldsymbol{A}}^T \boldsymbol{R}^{-1} \breve{\boldsymbol{A}}\right)$, $\boldsymbol{h}_k$ is the k^{th} column of $\boldsymbol{H}$ and $\boldsymbol{H}_{i,j}$ refers of the element of $\boldsymbol{H}$ at i^{th} raw and j^{th} column.
Algorithm: SCA-NNLS adapted for spectrum sensing
Input: $\breve{\boldsymbol{A}}$, $\boldsymbol{Z}$
Initialization: $n = 0$, $\boldsymbol{P}^0 = [p_m]$, $\boldsymbol{\mu}^0 = -\breve{\boldsymbol{A}}^T \boldsymbol{R}^{-1} \boldsymbol{Z}$
Repeat: for $k = 1$ to N 1. $\boldsymbol{P}_k^{n+1} = \max\left(0, \boldsymbol{P}_k^n - \boldsymbol{\mu}_k^{n+1} / \boldsymbol{H}_{k,k}\right)$, $\boldsymbol{P}_l^{n+1} = \boldsymbol{P}_l^n$ for all $l \in \zeta_k$ 2. $\boldsymbol{\mu}^{n+1} = \boldsymbol{\mu}^n + \left(\boldsymbol{P}_k^{n+1} - \boldsymbol{P}_k^t\right) \cdot \boldsymbol{h}_k$
Until: $\max\left(\boldsymbol{P}^{n+1} - \boldsymbol{P}^n\right) < p_m$ (the largest element in the vector $\boldsymbol{P}^{n+1} - \boldsymbol{P}^n$ is less than p_m)
Output: $\hat{\boldsymbol{P}}_{\boldsymbol{w}} = \boldsymbol{P}^{n+1}$

where p_m is the average power of additive noise in a channel at ADC output and $[p_m]$ is a vector whose elements are all equal to p_m.

5.3.4 Measuring CSR Model of a Receiver

The proposed estimator assumes prior knowledge of receiver's multi-LO-CS transform (or the $\breve{\boldsymbol{A}}$ matrix), and the multi-LO-zero-input CS response (the $\breve{\boldsymbol{V}}$ vector). This section presents a simple measurement mechanism for $\breve{\boldsymbol{A}}$ and $\breve{\boldsymbol{V}}$.

1) Measuring multi-LO-zero-input CS response ($\breve{\boldsymbol{V}}$): As it can be inferred from (3.19), the zero-input CS response at a given LO can obtained by measuring CSR of the ADC output while the receiver input is terminated with a matched load (no signal except noise is input to the receiver). The multi-LO-zero-input

CS response can be obtained by repeating this measurement at all the relevant LO frequencies.

2) Measuring multi-LO-CS transform ***(ĂĂ):*** As it can be inferred from (3.19), a column of CS transform can be obtained by measuring the CSR of the ADC output and subtracting the zero-input CS response; while only one channel is active at the receiver input. That is, only one channel contains a signal with non-zero input power. The other columns of the CS transform can be obtained by sequentially activating the corresponding input channels one at a time. By repeating the measurement at different LO frequencies, the multi-LO-CS transform can be obtained.

This measurement can be carried out in factory and the measurement results can be achieved in the cognitive engine. In doing these measurements, several issues should be taken into consideration. First, the zero input CS response has to be measured before the CS transform of a receiver can be measured. Secondly, the input signal should be within the dynamic range of the receiver; particularly the dynamic range of the LNA. The proposed CSR model is valid only within the dynamic range of the receiver. Thirdly, an appropriate normalization may be necessary because the power level within the active channel is not numerically equal to one.

5.4 Simulation based Evaluation of RS-MSS

This section presents simulation based experiments that demonstrate the benefits of RS-MSS over S-MSS, the current state-of-the-art. The receiver architecture shown in Figure 3.1 is assumed in this section. The pre-selector is

emulated by not generating any signal outside the frequency range of interest. The LNA is represented as a simple pass-through to the received signal (ideally linear LNA). The down-conversion mixer, the anti-aliasing filter and the ADC are modeled in time domain using (3.5), (3.10), and (3.14), respectively.

The first experiment shows the benefit of RS-MSS by using an example spectrum occupancy scenario. The second and third experiments use a probabilistic spectrum occupancy model to demonstrate the benefits of RS-MSS in a more general sense.

5.4.1 Simulating an Example Spectrum Scenario

This experiment simulated a 96 MHz spectrum that is divided into 96, 1 MHz channels. These channels are sensed using the simulated receiver. The parameters of the simulated receiver are listed in Table 5.3.

Table 5.3 Parameters of simulated receiver for experiment A.

Parameter	Value
Noise floor	-100 dBm per channel (referred to ADC output)
Pre-selector	Brick-walled 96 MHz bandwidth
LNA	Perfectly linear, unity gain
Down-conversion	Amplitude imbalance = 10%, Phase imbalance = 3^{o} That is, Image Rejection Ratio (IRR) = 25 dB
Anti-aliasing filter	5^{th} order Butterworth, Cut-off frequency = 5.3 MHz
ADC	Sampling frequency = 16 MHz
DSP	Blackman window with 256 point FFT Number of periodograms = 32

The spectrum is set to contain two, 0.5 MSa/s BPSK signals with power levels of -60 dBm and -50 dBm at the 26^{th} and 44^{th} channels, respectively. The BPSK signals use a root-raised cosine pulse shaping with roll of factor of 0.9.

First, S-MSS based spectrum sensing is carried out. The entire 96 MHz spectrum is measured by sensing a 16 MHz section at a time. Six non-overlapping 16 MHz sections were measured to sense the whole 96 MHz band.

Then, the CSR response of the simulated receiver is obtained using the mechanism that is described in Section 3.2. Finally, the output of S-MSS, and the measured CSR model of the simulated receiver are passed through the RS-MSS algorithm presented in Table 5.2. The output of the algorithm is compared with the output of S-MSS in Figure 5.1.

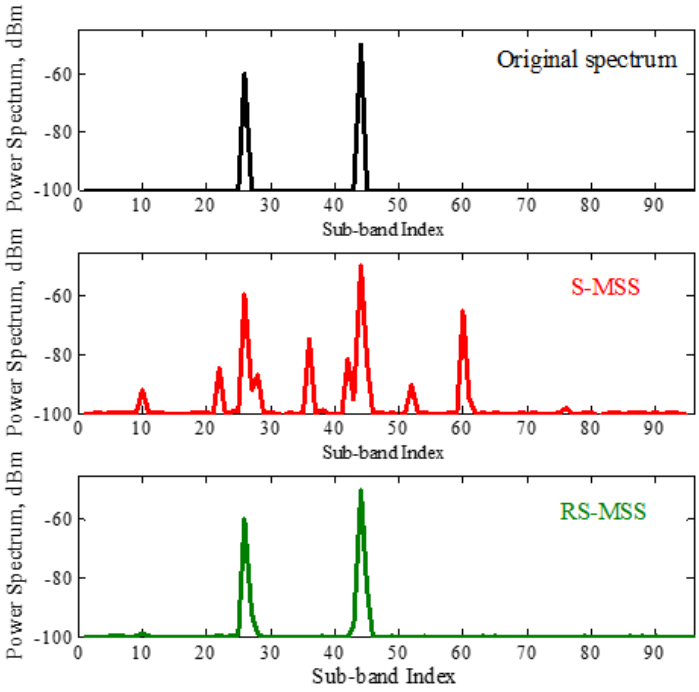

Figure 5.1 Comparison of RS-MSS and S-MSS.

The result in Figure 5.1 demonstrates that RS-MSS can provide a more accurate spectrum sensing compared to S-MSS. This is because the proposed mechanism minimizes the impact of receiver impairments on spectrum sensing.

5.4.2 Accuracy of RS-MSS

This experiment analyzes the benefits of RS-MSS in a more generalized sense. In this experiment, the spectrum is assumed to span 96 MHz which is divided into 96, 1 MHz wide channels.

The power level in the channels is assumed to follow the distribution in spectrum occupancy model given in Section 3.3, by setting p_m = -100 dBm, p_{TX} = 23 dBm, n_{pl} = 4 and $q_{oc} = 0.95$. The 3 dB bandwidth of the anti-aliasing filter is set to be equal to 5.3 MHz and sampling rate of ADC is equal to 16 MHz.

This experiment compares the accuracy of S-MSS with RS-MSS while varying the order of the anti-aliasing filter and the image-rejection ratio (IRR) of the simulated receiver. Accuracy is calculated as the average absolute difference between the measured and the true channel powers in dB domain. The result is presented in Figure 5.2.

Figure 5.2 shows that RS-MSS provides better spectrum sensing accuracy compared to S-MSS. It can also be observed that the accuracy S-MSS improves as IRR and the order of the anti-aliasing filter increases. This is because the effect of aliasing and image signals becomes less significant as the receiver becomes more selective.

Figure 5.2 Comparing accuracy of RS-MSS and S-MSS.

On the contrary, the accuracy of RS-MSS shows little dependence on receiver parameters. This observation confirms that RS-MSS minimizes the impact of receiver impairments on spectrum sensing.

5.5 Application in DSA

So far, the application of the RS-MSS was discussed from perspective of CogRF. This section shows the value RS-MSS in Secondary Users (SUs) of a DSA [104] to find truly vacant channel without being masked by receiver impairment.

A SU employing RS-MSS for spectrum sensing is considered in this section. The SU uses spectrum sensing to identify a vacant channel. The probability that an SU identifies a vacant channel is called probability of opportunity detection. This section shows that RS-MSS can improve the opportunity detection performance of a SU.

The spectrum is assumed to span 96 MHz which is divided into 96, 1 MHz wide sub-bands. The power content of all the sub-bands is generated using the distribution in (3.26). The power level of the 44^{th} sub-band (the center sub-band) was purposely set to be equal to p_m (the noise floor), and p_m = -100 dBm per sub-band. The simulation measures the opportunity detection performance by computing the probability that the measured power level at the 44^{th} sub-band (vacant sub-band) does not exceed the threshold, $p_m + 3$ dB.

In this experiment, two types of receivers were simulated. The first receiver has IRR = 31 dB and the order of its anti-aliasing filter is equal to 5. The second receiver has relatively inferior radio quality. It has IRR = 25 dB and the order of its anti-aliasing filter is equal to 3. For both cases, the 3 dB cutoff frequency of the anti-aliasing filter is set to be equal to 5.3 MHz and sampling rate of ADC is equal to 16 MHz. The simulation is run by varying q_{oc} between 0.1 and 0.9. The average opportunity detection probability obtained after 300 simulation runs is shown in Figure 5.3.

For ideal receiver, the probability of opportunity detection is expected to remain constant as the density of spectrum occupancy increases because there is no signal folding from other bands to the vacant band. In non-ideal receivers employing S-MSS, however, the probability of opportunity detection is expected to deteriorate as the density of spectrum occupancy increases. This assertion is

confirmed in Figure 5.3. According to the result, the probability of opportunity detection in S-MSS based SU has strong dependence on the density of spectrum occupancy. In addition, the probability of opportunity detection was shown to be lower for a lower quality sensing receiver.

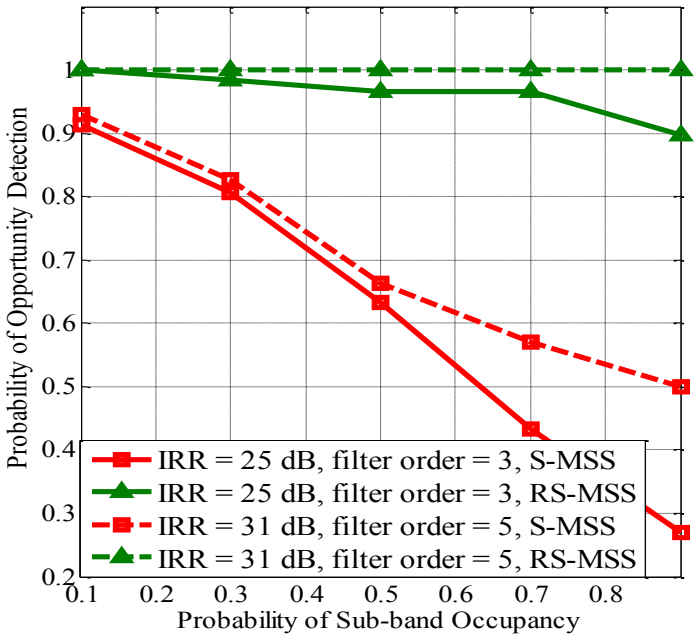

Figure 5.3 Opportunity detection probability while using RS-MSS and S-MSS.

The probability of opportunity detection is shown to be significantly better when RS-MSS is employed. In addition, similar to an ideal receiver, the probability of opportunity detection shows little dependence on both the density of spectrum occupancy and the quality of the receiver. This indicates that RS-MSS based SU can exhibit significantly better throughput in spectrum sharing network compared to S-MSS based SU. In addition, the result imply that RS-MSS based SU can behave similar to a high-quality receiver even if it has poor RF front-end quality.

5.6 Chapter Summary

This chapter presents a spectrum sensing mechanism that can address the effects of IQ imbalance and aliasing in multi-band spectrum sensing. The developed sensing mechanism is called Robust Serial Multi-band Spectrum Sensing (RS-MSS). RS-MSS is designed to measure the occupancy of the spectrum for the cognitive engine in CogRF.

RS-MSS estimates the true state of the spectrum at the receiver input by removing the effects of receiver imperfections from the spectrum sensing data measured at the output of analog-to-digital converters (ADC). To achieve this, RS-MSS uses the CSR-based modeling to track how energy is re-distributed inside the receiver due to IQ imbalance and aliasing. RS-MSS estimates the state of the spectrum at the receiver input by applying the ADC output to the reverse CSR model of the receiver.

A simulation-based evaluation shows that the RS-MSS significantly improves the accuracy of spectrum sensing. It is shown that RS-MSS provides up to 2.5 dB improvement in spectrum accuracy for poorly-selective receivers. In addition, this chapter shows that RS-MSS can also be applied in DSA to improve the opportunity detection performance of secondary users significantly. The results show that RS-MSS improves the opportunity detection performance of a secondary user by up to 74-percetnage points – from 26% to about 100%.

Chapter 6

CogRF Implementation

6.1 Overview

The later part of this research involves implementing CogRF according to the designs presented in Chapter 3, 4 and 5. This chapter is written as a documentation for the CogRF implementation. This chapter also reports the results obtained from experiments carried out using the implementation and demonstrates how the performance of a radio containing low quality RF components can be improved using CogRF.

Wireless@Virginia Tech's RFIC5 circuit-board [105] is used as a platform for the CogRF implementation. RFIC5 is one of the recently introduced CMOS-based, flexible RFICs. This RFIC is ideal for CogRF implementation because it is highly

reconfigurable and its parameters are digitally-controllable. The picture of the RFIC5 circuit board is shown in Figure 6.1.

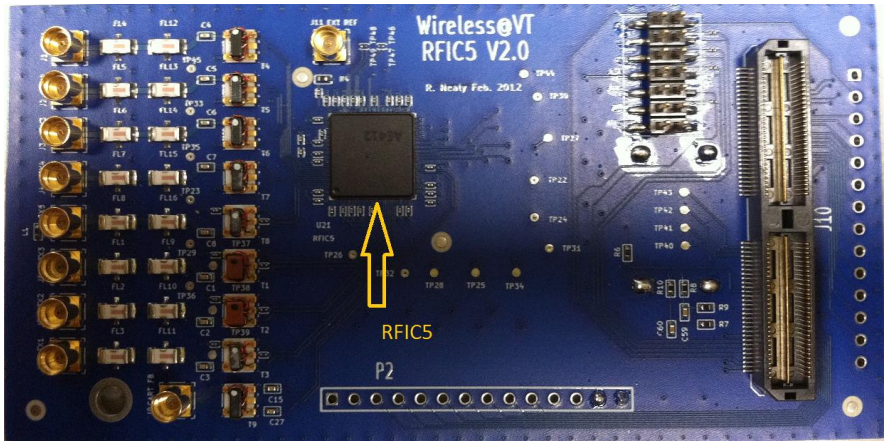

Figure 6.1 Wireless@Virginia Tech's RFIC5 board.

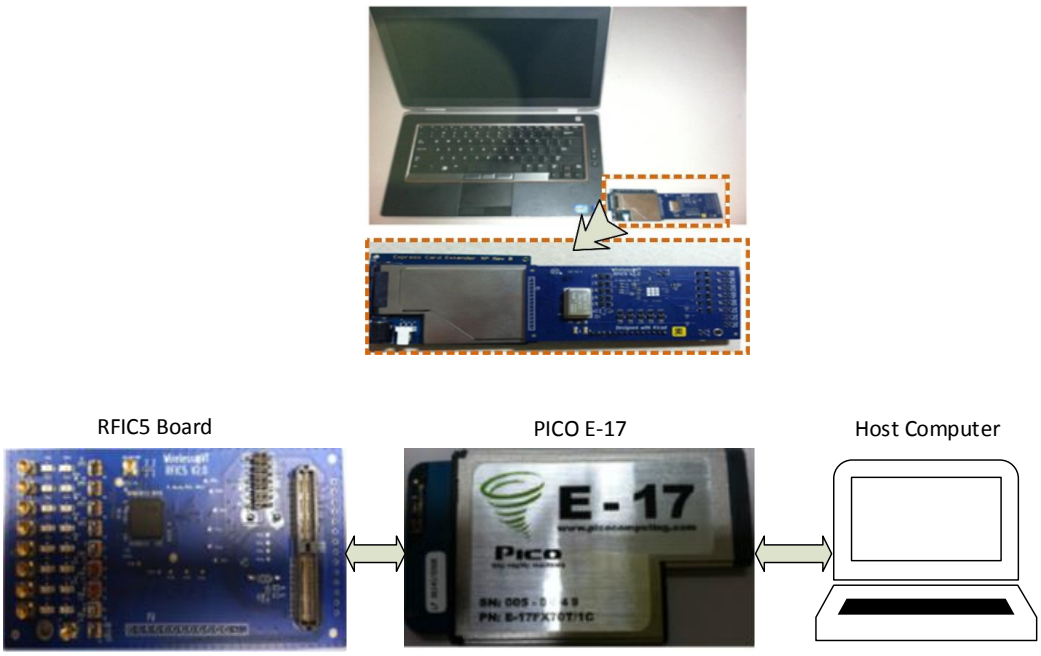

Figure 6.2 PicoRF platform.

This board interfaces with Pico Computing's PICO E-17 FPGA board. This board contains Xilinx's FX70T family Virtex-5 FPGA. The PICO E-17 board interfaces with a host computer through PCI Express (PCIe) connector. The combination of the RFIC5 board and PICO E-17 is called PicoRF [105]. The picture of a PicoRF plugged to a host computer is shown in Figure 6.2.

The detail of the CogRF implementation is shown in Figure 6.4. Controlling the LO and sampling frequencies of PicoRF using the cognitive engine designed in Chapter 4 is the main objective of the CogRF implementation. To simplify the development, the cognitive engine is implemented using software running on the host computer. The other elements of the CogRF implementation are described below.

- *Spectrum sensing*: The implementation of the spectrum sensor is distributed across the FPGA and the host computer. In the FPGA, the Power Spectral Density (PSD) of the receiver output is measured using periodogram-based FFT processing (see Section 5.3.2). In the host computer, CSR of the received input is estimated from the PSD of the receiver output using the approach presented in Chapter 5.

  In the current CogRF implementation, the spectrum sensor and the modem share the same receiver RF front-end. Hence, spectrum is sensed only when the desired signal is not being received. Consequently, the current CogRF implementation cannot be operated in FDD mode.

- *CSR model measurement*: As discussed in Chapter 4 and Chapter 5, both the spectrum sensor and the cognitive engine algorithms assume a knowledge of the receiver RF front-end's CSR model. For this purpose, a CSR-model-measurement mechanism is implemented using a script that runs on the host

computer. The implementation of this mechanism is based on the approach presented in Section 5.3.

As shown in Figure 6.4, the CSR-model-measurement script can control external signal generators through Ethernet LAN. The script should be invoked on the host computer only after the RF output from a controlled signal generator is manually connected to the receiver's input port. The script automatically commands the signal generator to inject a desired RF signal into the receiver. The script uses Standard Commands for Programmable Instruments (SCPI) [106] to control signal generators.

After measuring the CSR of the receiver RF front-end, the CSR-model-measurement script stores the output of the measurement in a database file along with the corresponding settings of the RF front-end. Note that the CSR model of the RF front-end changes with any change in the frequency plan setting of the receiver.

- *Sample-rate matching and down-conversion*: At the input of the modem, the desired signal needs to be running at specific sampling-rate and its center frequency should be zero. However, because the cognitive engine adjusts the sampling and LO frequencies of the receiver, the frequency and sampling-rate of the receiver output may not match the specifications of the modem. Therefore, a sample-rate matching block is used to match the sample-rate of the receiver output to the specification of the modem. Similarly, a complex multiplier along with a Number-Controlled-Oscillator (NCO) is used to down-convert the receiver RF front-end output to zero frequency.

  It should also be noted that the settings of the sample-rate matching block and the NCO are respectively matched to the sampling and LO frequency settings

of the RF front-end. That is; whenever the frequency plan of the RF front-end is changed by the cognitive engine, the settings of the sample-rate matching block and the NCO are also changed accordingly.

- *FPGA registers*: The CogRF software controls the elements of the FPGA by writing into the FPGA registers. The FPGA registers also map the RFIC registers for the CogRF software. Hence, the CogRF software accesses the RFIC registers indirectly through the FPGA registers.

The frequency band ranging approximately from 891 MHz to 939 MHz is used for experimenting the implementation. As shown in Figure 6.3, this band is channelized into 24 sub-bands (channels). This frequency range is selected because it contains the 915 MHz ISM band. The cognitive engine uses one of two possible sampling frequencies, and one of five possible LO frequencies to configure the RF front-end. Accordingly, the RF front-end can attain one of ten possible settings at a time. The list of the sampling and LO frequencies used in the CogRF implementation are listed under Table 6.1. The five possible LO frequencies are shown in Figure 6.3 as well.

Table 6.1 Parameters of CogRF implementation.

Parameter	**Value/s**
Channel bandwidth	1.953125 MHz
Sampling rates	1. 31.25 MSa/s (16 channels) 2. 15.625 MSa/s (8 channels)
LO frequencies	1. 922.8125 MHz 2. 911.09375 MHz 3. 915.0000 MHz 4. 918.90625 MHz 5. 922.8125 MHz

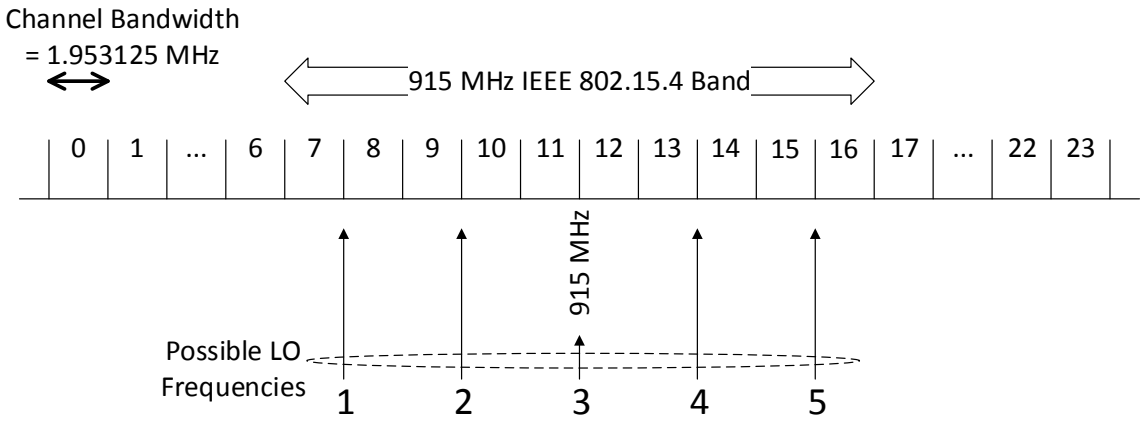

Figure 6.3 Channelization of experiment's frequency band for experiment.

The next section details the hardware subsystem of the CogRF implementation. Then, Section 6.3 presents the details of the software subsystem of the implementation. Finally, Section 6.4 presents the set-up of the experiments and reports the obtained results.

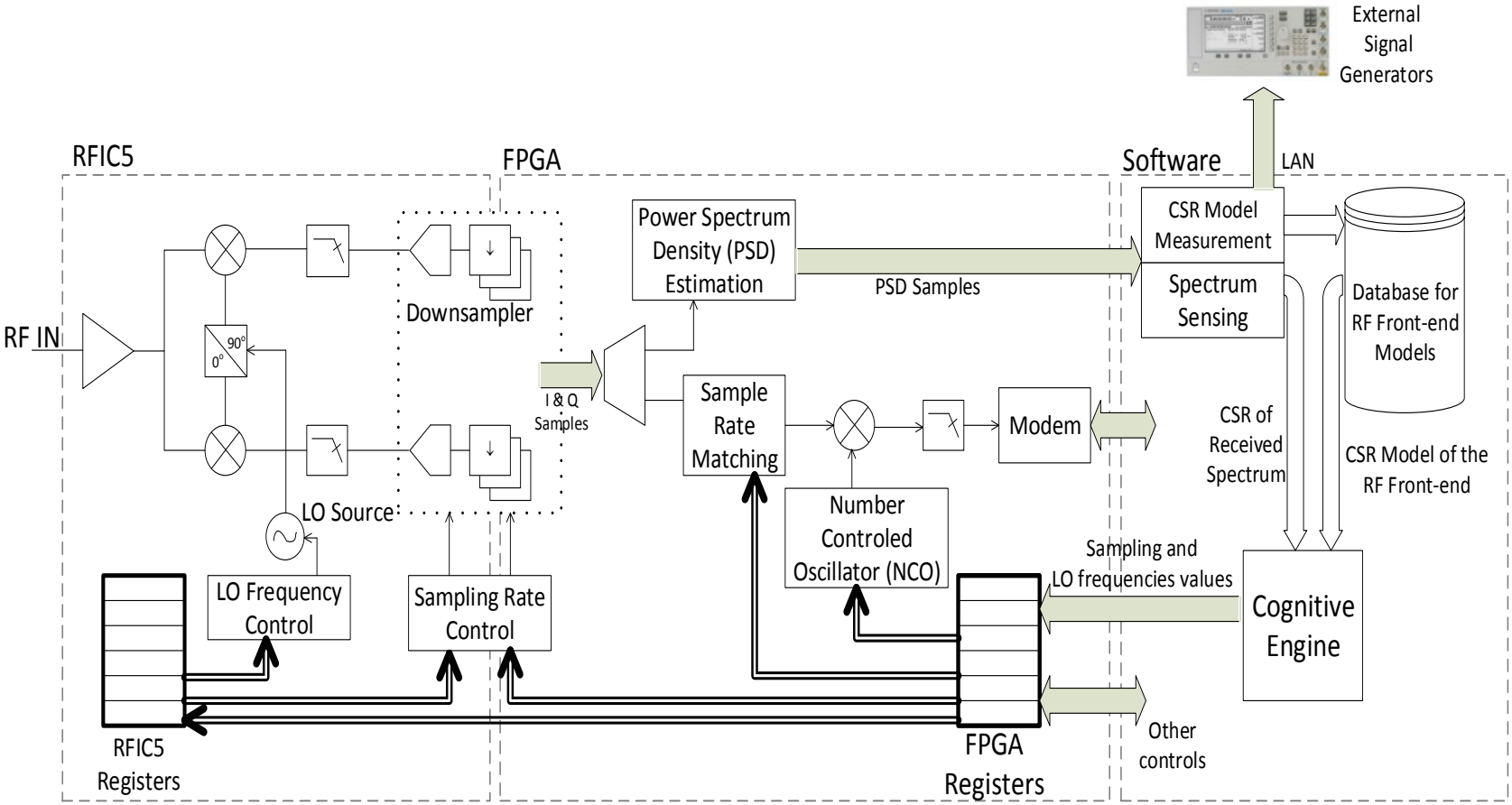

Figure 6.4 CogRF implementation architecture.

6.2 Hardware Subsystem

6.2.1 RFIC5

As described above, RFIC5 is a CMOS-based, highly reconfigurable and digitally-controllable RFIC. It is operational from 100 MHz to 4 GHz. It can also operate up to 6 GHz using an external LO source. The RFIC contains more than 1000 registers to control its parameters. For example, its LNA bias, LNA gain, baseband filter gain, baseband filter selectivity, LO frequency, LO phase, ADC sampling clock rate, decimation rate after the ADC, interpolation rate before DAC, transmitter's gain, and many more features are all controllable through the registers of the RFIC. The registers can be accessed from outside through SPI bus provided at the ports of the RFIC.

RFIC5 has ADC, DAC and the associated DSP on the same chip. A high-speed serial bus carries the bits of IQ samples into and out of the RFIC.

6.2.2 Wireless@VT's RFIC5 Board

As mentioned above, Wireless@Virginia Tech's RFIC5 board is used in the CogRF implementation. In addition to the RFIC5, the board contains the following elements;

- *Oscillator:* A 31.25 MHz oscillator is used to reference the RFIC. The stability-performance of the oscillator is about 10 ppm.
- *JTAG:* The JTAG for configuring the FPGA on the PICO E-17 board is also placed on the RFIC5 board.
- *FPGA interface port:* A high-speed interface port is used between the PICO E-17 board and the RFIC5 board. This port carries, the high-speed serial IQ

sample bus, the system clock generated by RFIC5, SPI bus between the FPGA and the RFIC, JTAG, and other general purpose pins.

6.2.3 Inside the FPGA

Figure 6.5 shows a high-level block diagram of the implementation inside the FPGA. The major components are the RFIC-data-interface block, the RFIC-control -interface block, DC offset-correction (DCOC) block, the DSP block, and the PCIe- interface block. The operation in the FPGA is referenced by a 100 MHz clock. This clock is generated on the PICO E-17 board.

For the receive path, the RFIC-data-interface block de-serializes bits coming from the RFIC and constructs the IQ samples. The output of the RFIC-data-interface block is first passed through a DCOC block to reject DC in the received signal. The signal is then passed to the DSP module for further processing. The sample-rate matching block, the filter of the desired signal, the modem and the PSD estimation block are all contained in the DSP module.

The RFIC-control-interface block communicates with the RFIC registers through an SPI bus. The block maps the FPGA registers (see Figure 6.4) to the registers of the RFIC. Accordingly, a software running on the host computer accesses the RFIC registers indirectly through the FPGA registers.

The other block is the PCIe-interface block. It is implemented according to the PCIe standard in [107]. Xilinx's PCIe endpoint IP implements the lower two layers of the standard; and this IP is used in this implementation. The remaining upper layer (the transport layer) is implemented based on the architecture given in [105]. As shown in Figure 6.4, the upper layer is composed of the PCIe transmitter (TX) engine, the PCIe receiver (RX) engine and the FPGA registers.

Unlike the design in [105], however, this PCIe-interface block is not optimized for streaming data transfer. In the CogRF implementation, the PCIe interface carries either short control (FPGA register read/write) packets or PSD packets originating from the FPGA.

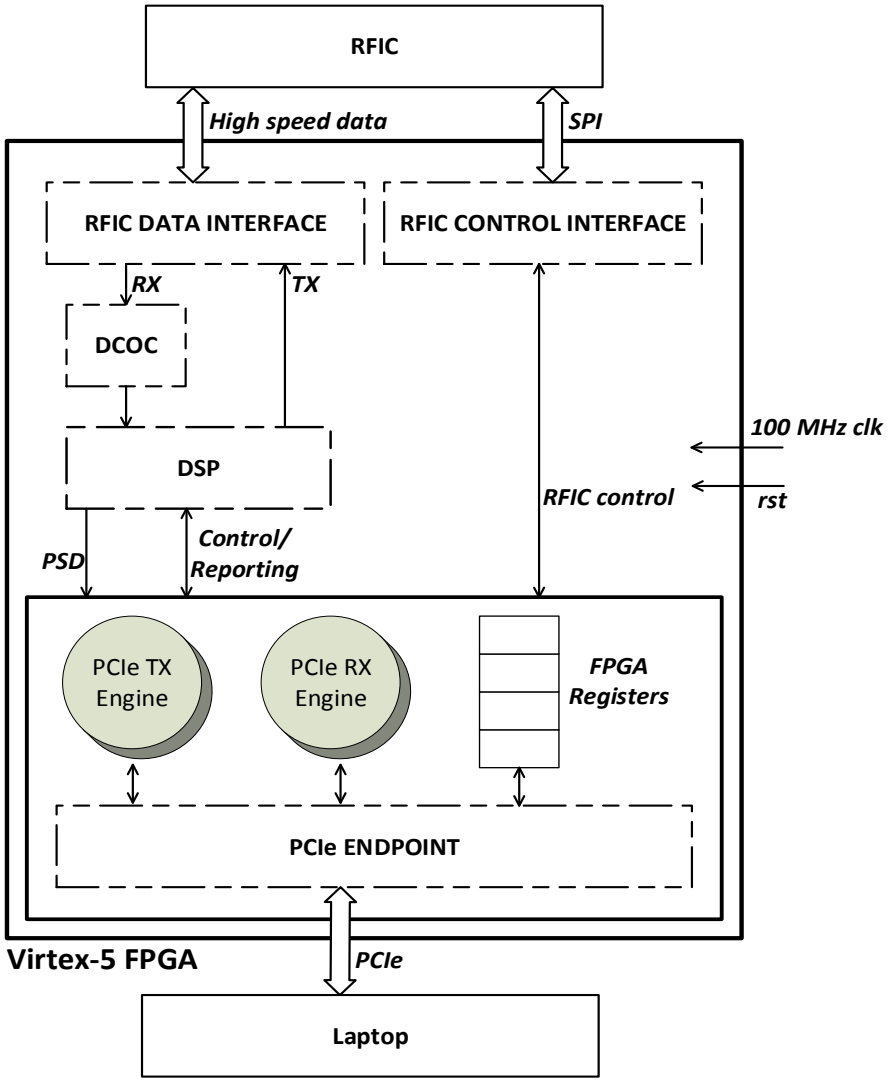

Figure 6.5 Inside the FPGA in CogRF implementation.

6.2.4 Signal Processing in the FPGA

The inside detail of the DSP block is shown in Figure 6.6. The DSP block contains a sample-rate matching chain, a down-conversion multiplier and NCO, a modem, a power measurement block and a PSD estimation block.

RFIC5 becomes unstable when its sampling rate is changed dynamically. A complete reset on the RFIC is typically required to change the sampling-rate reliably. To circumvent this issue, the sampling-rate selection is actually carried out in the FPGA. In addition, the signal output from the RFIC is always sampled at 31.25 MSa/s, which is equal to the first sampling-rate setting listed in Table 6.1. As it can be shown in Figure 6.4, if the cognitive engine selects a sampling rate of 15.625 MSa/s, the down-sampled-by-2 version of the RFIC output is passed through the first multiplexer (MUX-1 in Figure 6.6) instead of the original 31.25 MSa/s RFIC output.

The LO frequency is adjusted in the RFIC. The selected LO frequency may not be equal to the RF frequency of the desired signal. Therefore, the output of MUX-1 is down-converted to zero frequency whenever it is necessary. Then, the signal is further down-sampled before it enters the modem. The sample-rate specification of the modem input is approximately equal to 2 MSa/s.

The power measurement block measures the power contained in the desired channel by averaging the instantaneous power of 1024 IQ samples at the input of the modem.

Two types of filters were used in the DSP block. The first kind filter is used in the down-sample-by-2 blocks and it is referred as FIL-A in Figure 6.6. The other filter is used right before the modem to extract the signal from the desired

channel[12]. The second filter is referred as FIL-B in the figure. The frequency response of these two filters is shown in Figure 6.7. The filters are placed in a 200 MHz clock region to reduce the number of multipliers they require. The DSP resource consumption of the filters is presented Table 6.2.

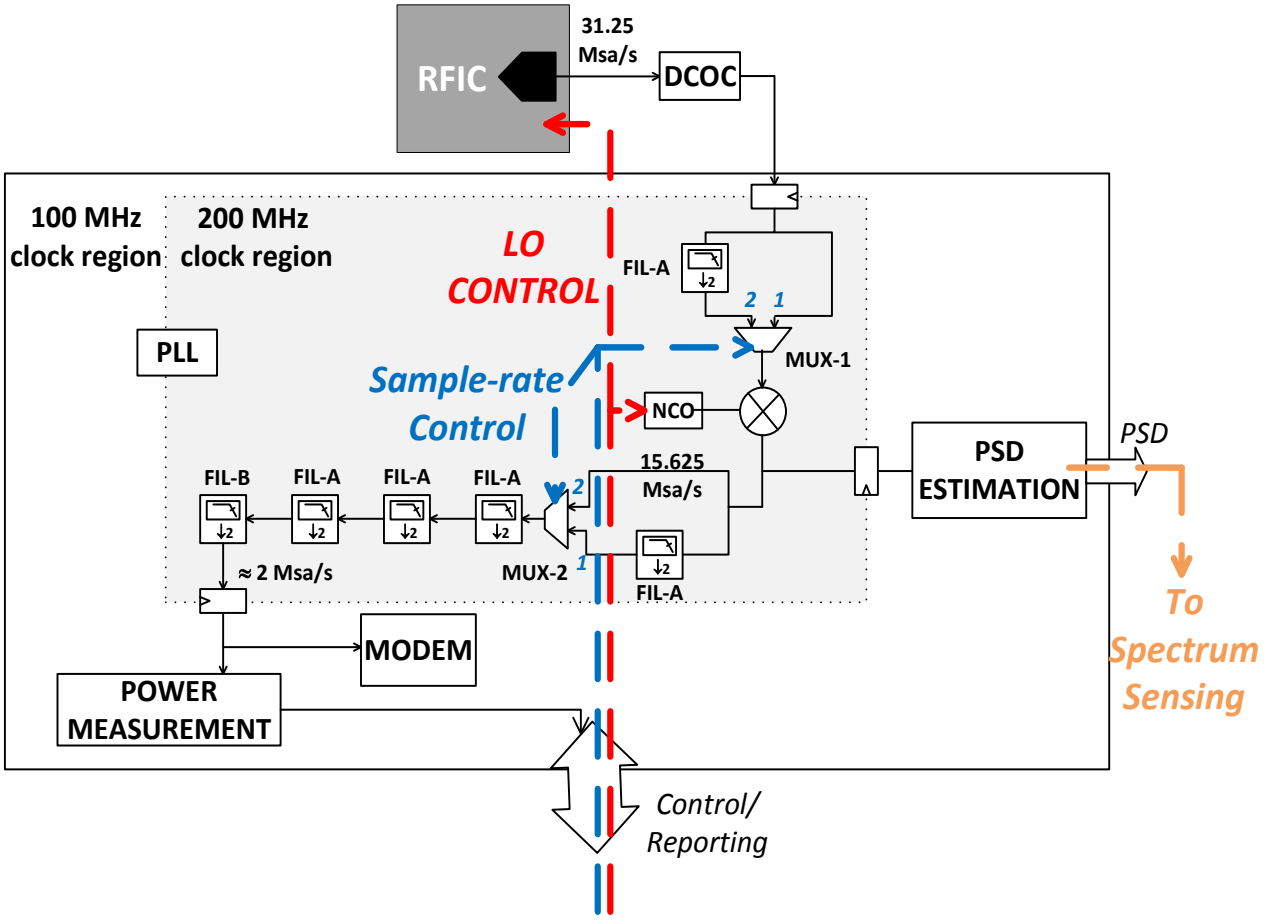

Figure 6.6 Inside the DSP block within the FPGA.

Table 6.2 Resource consumption of the DSP block.

Filter	Number of taps	Number of Multipliers
FIL-A	21	6
FIL-B	8	2

[12] Note that the signal does not occupy the whole channel

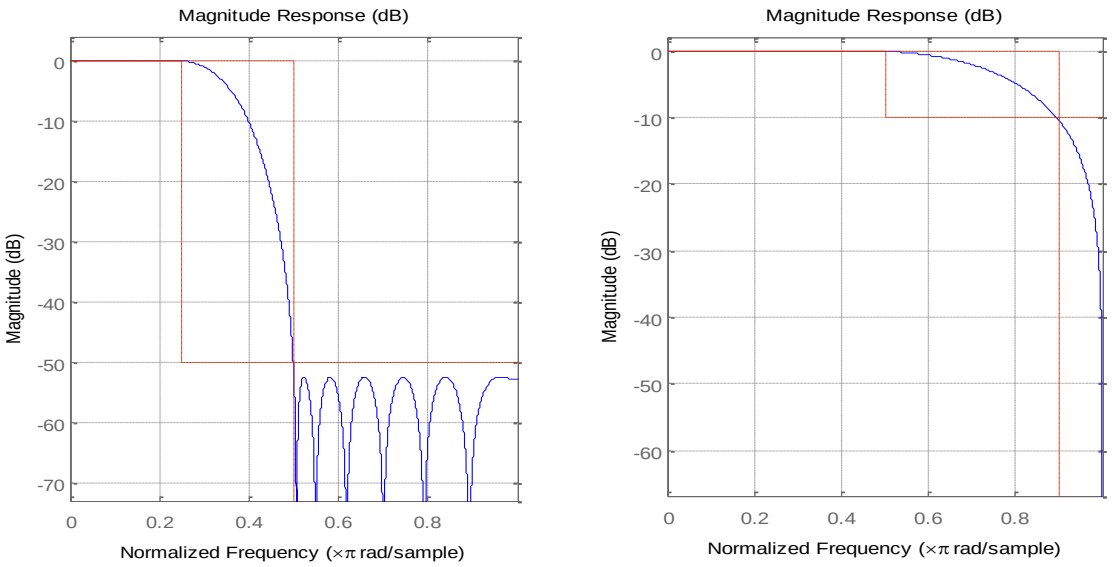

Figure 6.7 Frequency characteristics of DSP filters (left: FIL-A, right: FIL-B).

6.2.5 PSD Estimation

The PSD estimation block serves the spectrum sensing function of the CogRF software (see Section 6.3). The spectrum sensing function computes the CSR of the received signal from the PSD data it obtains from the PSD estimation block in the FPGA.

The PSD estimation block is implemented using FFT periodogram based scheme [75] that is shown in Figure 6.8. According to the design in Section 5.3.2, a Blackman window is applied on the signal to minimize the leakage between adjacent channels during CSR measurement.

Thirty-two periodograms of 1024-point FFT are used to estimate PSD of the ADC output. The PSD estimation consumes a total of 11 multipliers and 13 kBytes of memory on the FPGA.

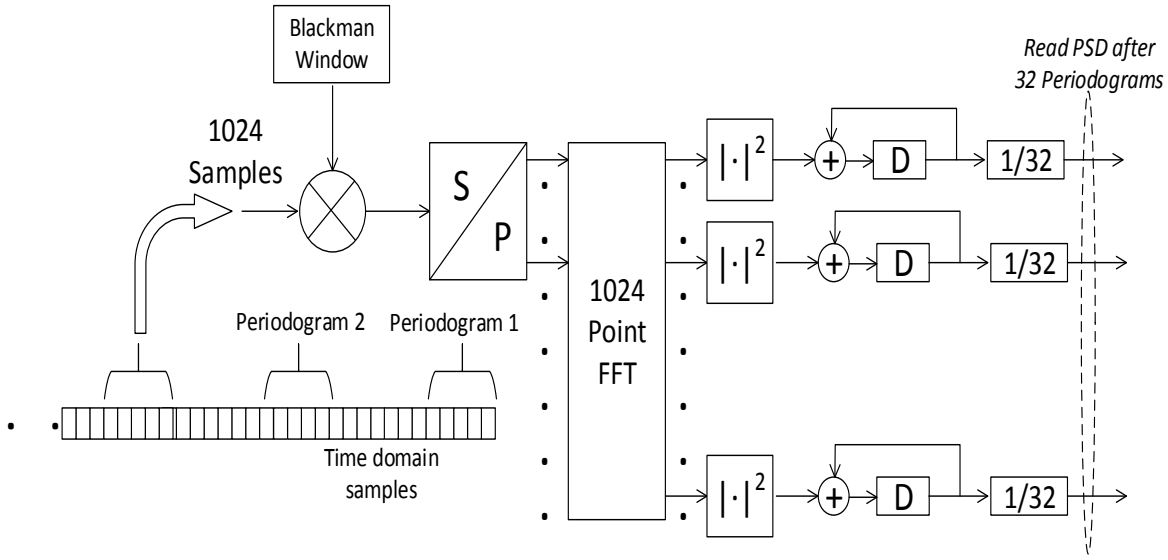

Figure 6.8 FFT periodograms based PSD estimation.

6.3 Software Subsystem

The CogRF software is implemented using C-programming language. The software is developed on Ubuntu's 12.04 distribution which contains the Linux 3.5.0-23-generic kernel.

The CogRF software contains four layers. These are; the driver, PicoRF API, CogRF API and CogRF application layers. The details of these layers is presented in this section. The architecture of CogRF is pictorially presented in Figure 6.9.

6.3.1 Linux Driver

A Linux PCI character-driver [108] is implemented to interface the CogRF software with the FPGA in PicoRF. The major functions of the driver are listed in Table 6.3.The table also shows how each driver function is invoked.

Table 6.3 Major driver functions

Name of function	**Invoked by**	**Purpose**
probe( )	Invoked by kernel when PicoRF is plugged on PCIe slot	- Enables the character device (a file abstraction of the hardware)
remove( )	Invoked by kernel when PicoRF is removed from PCIe slot	- Disables the device
open( )	Invoked from PicoRF API	- Needs to be called before read( ) and ioctl( ) calls - Allocates DMA buffers - Resets PCIe interface block in FPGA
close( )	Invoked from PicoRF API	- De-allocates DMA buffers
read( )	Invoked from PicoRF API	- Read from the buffers associated with the TX engine in the FPGA (see Figure 6.5)
ioctl( )	Invoked from PicoRF API	- Read and write to the FPGA registers (see Figure 6.5)

6.3.2 PicoRF API

The PicoRF API abstracts the driver's functions to upper layer functions. In this implementation, the PicoRF API has two parts - the DSP API and the RFIC API. The functions in the DSP API target the elements of the DSP block in the FPGA while the functions in the RFIC API target the registers of the RFIC. The

RFIC API developed in [105] is re-used in this implementation. The functions in the DSP API, and some of the functions in the RFIC API are presented in Table 6.4. Some arguments of these functions are also shown in the table. A more extensive list of the RFIC API is presented in [105].

Table 6.4 Functions in PicoRF API.

Function Name	**Purpose**
DSP API	
picorf_read (int *src*, …)	This function is used to read from one of the following, - if *src* = PSD (or 1), reads output of PSD estimation block in the FPGA (see Figure 6.5) - if *src* = MODEM (or 4), reads output of the modem in the FPGA (see Figure 6.5) - if *src* = CHANNEL_PWR (or 3), reads the output of the power measurement block in the FPGA (see Figure 6.5)
set_dsp_freq(…)	This function sets the frequency of the NCO output, the state of MUX-1 and the state of MUX-2 in the FPGA (see Figure 6.5).
Low-level RFIC API	
rfic_reset(…)	Resets the RFIC
SPI_read(int *addr*)	Reads from the RFIC register at address *addr*
SPI_write(int *addr*, …)	Writes from the RFIC register at address *addr*
High-level RFIC API	
quiet_freq(*int freq*,…)	Used to set the output of frequency sources in the RFIC. One of the sources is the LO source of the receiver.
set_LNA_bias(…)	Sets the bias of the LNA

Function Name	Purpose
set_rxbb_bw(…)	Sets the bandwidth of the receive baseband filters
set_ADC_decimation(…)	Sets the decimation rate in the decimation filters in the RFIC

6.3.3 CogRF API

The CogRF API contains the functions that are used to construct the cognitive engine, the spectrum sensor and the CSR-model measurement mechanisms. The list of functions in the CogRF API are listed in Table 6.5.

Table 6.5 Function in CogRF API.

Function Name	Purpose
csr(int *fs* , int *flo*, …)	Sets the sampling rate and LO frequencies of the RF front-end to *fs* and *flo*, respectively. Then, it measures the CSR of the ADC output according to the procedure described in Section 5.2. It uses picorf_read(…) from the PicoRF API to obtain the PSD of the receiver output.
s_mss(int *fmin*, int *nbin*,…)	This function does multi-band spectrum sensing using the S-MSS method described in Chapter 4. It senses the spectrum starting from frequency *fmin*, and senses *nbin* channels.
rs_mss(…)	This function senses the spectrum within the default frequency range[13] using the RS-MSS mechanism described in Chapter 4.

[13] The default frequency range contains 24 channels from 891 MHz to 939 MHz. (A channel is approximately 2 MHz wide). The 915 MHz ISM band is contained in this range.

Function Name	**Purpose**
get_chan_pwr(int *channel_idx*, …)	This function measures the average power output in the desired channel. The index of the desired sub-band is given by *channel_idx*. And, if sampling rate is equal to 31.25 MSa/s (option 1), $0 \leq channel\_idx \leq 15$ and if sampling rate is equal to 15.625 MSa/s (option 2), $0 \leq channel\_idx \leq 7$
config_radio(int *fs_idx*, int *flo_idx*)	This function sets the sampling and the LO frequencies of the RF front-end. The value of the sampling frequency is set using the index *fs_idx* and the value of the LO frequency is set using the index *flo_idx*. And, *fs_idx* = 1,2 and *flo_idx* = 1,2,3,4 or 5. The values corresponding to these of these indices is given in Table 6.1.
engine(…)	This function implements the cognitive engine algorithm that was designed in Chapter 4.
siggen_ctrl(int *freq*, int *pwr*, char* *ip*)	This function sets the frequency and power the RF output of a signal generator at address *ip*. This function is used by the functions that measure the CSR model of the RF front-end.
gen_engine_db(…)	This function generates the CSR model of the RF front-end and saves it into a database file according to the format used by the cognitive engine. It uses siggen_ctrl(…) to control the signal generators.
gen_sense_db(…)	This function generates the CSR model of the RF front-end and saves it into a database file according to the format used by rs_mss_default(…)

6.3.4 CogRF Applications

The last layer contains executables that are used to experiment the overall CogRF implementation. The list of these executables is given in Table 6.6. The results reported in Section 6.4 are obtained using these executables.

Table 6.6 Executables for CogRF applications.

Executable	**Purpose**
./psd	- Gets raw PSD samples and displays them in GNU plot. This script is used for debugging purposes.
./csr *flo fs*	- Setting the sampling frequency to *fs* and LO frequency to *flo* - Computes and returns the CSR of the ADC output
./s_mss	- Senses spectrum in the default frequency range* using the S-MSS mechanism
./rs_mss	- Senses spectrum in the default frequency range* using the RS-MSS mechanism
./cogrf	- Senses the spectrum using rs_mss(…) - Selects feasible optimal and sampling frequencies - Configures the RF front-end accordingly
./calib	- Obtains the CSR model of the RF front-end and saves it to the appropriate files
./power *idx*	- Measures the average power of the signal contained in the channel referenced by *idx*

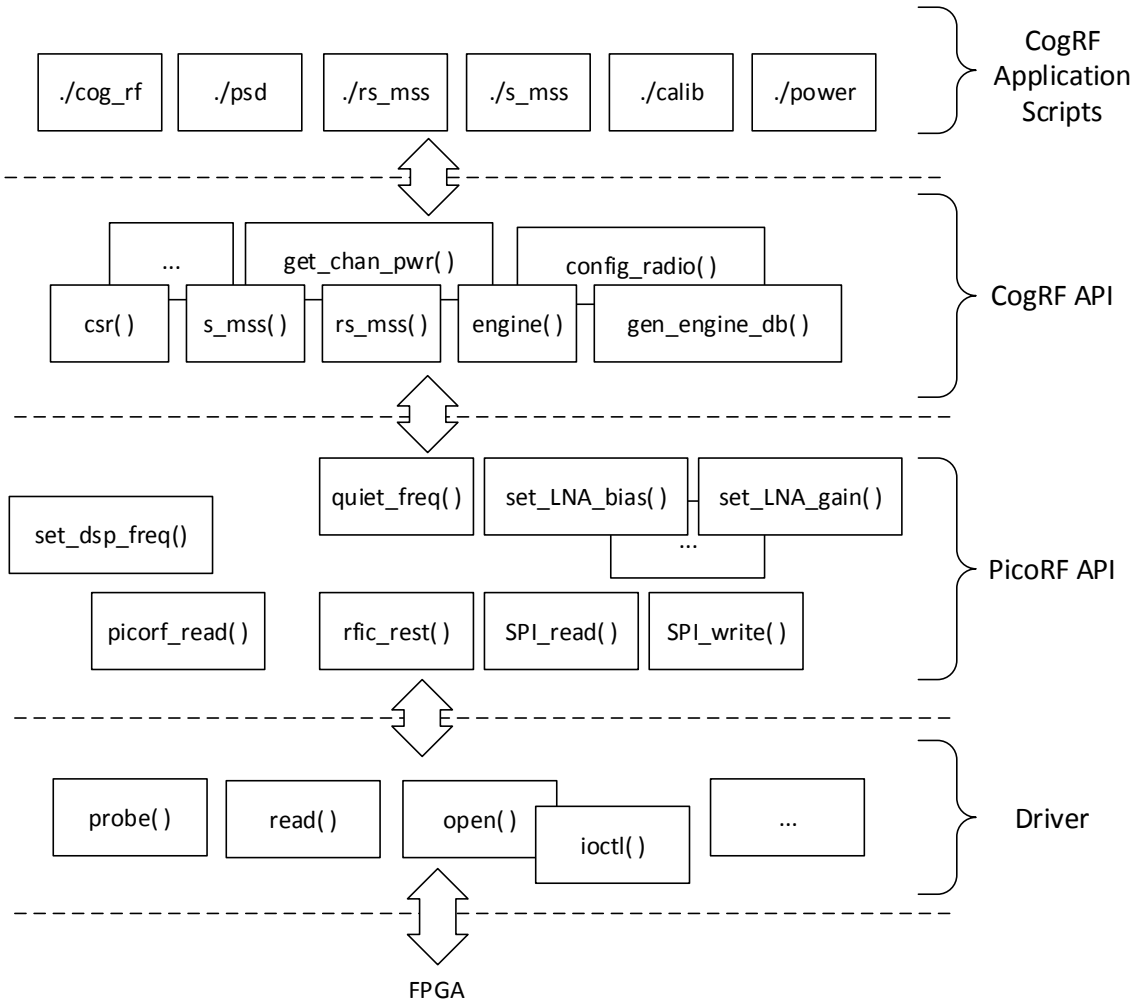

Figure 6.9 Elements of the CogRF Software.

6.4 Experiments

Figure 6.10 shows the experiment set-up that is used in this research. The set-up contains a PicoRF platform and three signal generators. The host computer uses Standard Commands for Programmable Interface (SCPI) [106] over a local-area network to control the frequencies and power levels of the signal generators' RF output. The outputs of the signal generators are input to the receiver through a

combiner. CogRF applications, such as ./rs_mss and ./cog_rf, are executed in the host computer. The configurations and the results of the experiments are presented in this section.

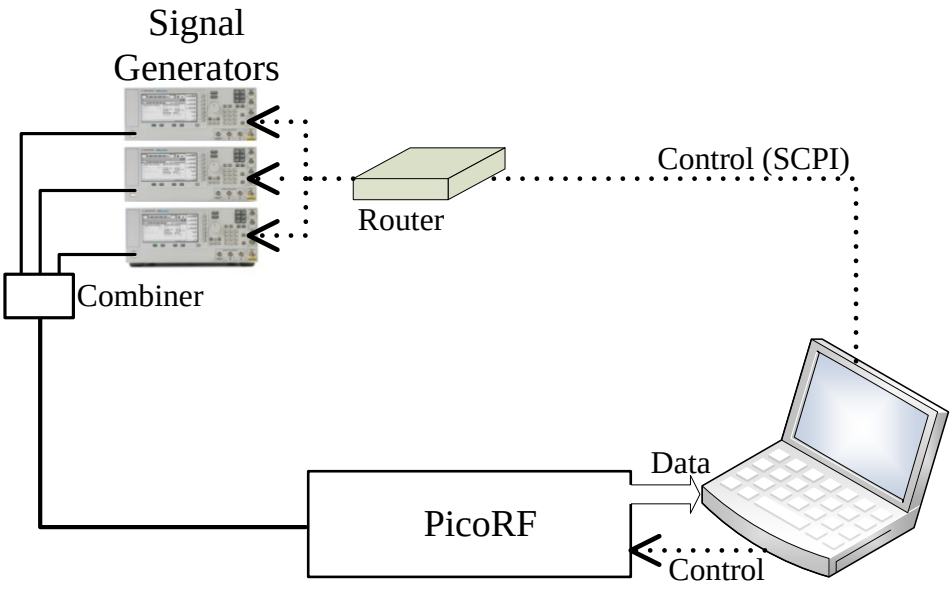

Figure 6.10 Experiment setup to demonstrate RS-MSS.

6.4.1 Receiver Performance Metric

To illustrate the validity of the CSR modeling technique and the receiver performance metric that is proposed in Section 3.4, the following experiment is carried out. Because it contains a reconfigurable RF front-end, PicoRF is ideal for this experiment because it can demonstrate how the proposed metric varies as the characteristics of a receiver changes.

In this experiment, the proposed metric is measured while the receiver is configured at different baseband-filter-bandwidth and sampling-rate settings. The CSR transform and the zero-input CSR response of the receiver are first measured

using the scheme that is presented in Section 3.4, using a -30 dBm single tone signal ($p_{meas} = -30$ dBm). $\hat{\boldsymbol{B}}$ of PicoRF that is measured for 7 MHz baseband bandwidth, and 15.625 MSa/s sampling-rate is shown in Figure 6.11. To save space, values are shown only to the second decimal place. The measured matrix clearly exhibits some of the CSR signatures that are presented Section 3.5.

Columns 1 to 12

0	0	0	0	0	0	0	0	1.00	0	0	0
0	0	0	0	0	0	0.04	0	0	1.00	0	0
0	0	0	0	0	0	0	0	0	0	1.00	0
0	0	0	0	0	0	0	0	0	0	0	1.00
0	0	0	0	0	0	0	0	0	0	0	0.01
0	0	0	0	0	0	0	0	0	0	0.03	0
0	0	0	0	0	0	0.01	0	0	0.45	0	0
0	0	0	0	0	0	0	0.40	0.17	0	0	0

Columns 13 to 25

0	0	0	0.26	0.56	0	0	0	0	0	0	0	0.01
0	0	0.22	0	0	0.01	0	0	0	0	0	0	0.02
0	0.01	0	0	0	0	0	0	0	0	0	0	0.02
0.00	0	0	0	0	0	0	0	0	0	0	0	0.00
1.00	0	0	0	0	0	0	0	0	0	0	0	0.00
0	1.00	0	0	0	0	0	0	0	0	0	0	0.02
0	0	1.00	0	0	0.07	0	0	0	0	0	0	0.03
0	0	0	1.00	0	0	0	0	0	0	0	0	0.02

Figure 6.11 $\hat{\boldsymbol{B}}$ of the experimented receiver platform. The non-zero elements of the matrix are colored. The grayed elements, that contain 1.00, denote the desired mapping between the sub-bands at the receiver input and output. The pinked elements are likely due to the effects of IQ imbalance. The light-blued elements are likely due to the effects of aliasing. Finally, the greened elements in the last column represent the noise-floor.

The receiver performance metric that is measured at different receiver configurations are reported in Table 6.7.

Table 6.7 Measured receiver performance metrics

Baseband filter's 3 dB bandwidth	Sampling rate	ρ
14 MHz	15.625 MSa/s (8 sub-bands)	0.81 dB
14 MHz	31.25 MSa/s (16 sub-bands)	7.33 dB
7 MHz	15.625 MSa/s (8 sub-bands)	1.86 dB
7 MHz	31.25 MSa/s (16 sub-bands)	9.47 dB

As it should be expected, the results show that a higher ρ score can be obtained when the receiver is set at higher selectivity and higher sampling-rate. The values of ρ in the table generally reflect the intuition on the relative qualities of the receiver configurations. This indicates the practical validity of both the proposed receiver performance metric and the CSR-based receiver modeling technique.

6.4.2 RS-MSS based Spectrum Sensing

In this experiment, RS-MSS is demonstrated to improve the accuracy of multi-band spectrum sensing using PicoRF. The image rejection ratio of PicoRF receiver varies with frequency, but it can be as low as 20 dB. The anti-aliasing filter in the receiver is a 5^{th} order Butterworth type active filter. Over-sampling sigma-delta ADC is employed in the receiver. Aliasing of signals and noise is caused mainly due to finite rejection of the decimation filters. These receiver impairments can easily degrade the accuracy of spectrum sensing data obtained from PicoRF.

The frequency range that is shown in Figure 6.3 (from 891 MHz to 939 MHz) is sensed in this experiment. As shown in the figure, this spectrum contains 24, 1.953124 MHz wide channels. The sampling rate is equal to 15.625 MHz. This means that there are 8 channels in the first Nyquist zone. Thus, three S-MSS steps are needed to sense the 24 channels. Because the CSR measurement in the FPGA used 1024 point FFT, 128 FFT samples fall within each of the 8 channels of the

first Nyquist zone. According to (5.3), this oversampling rate is sufficient to reject the power leakage between neighboring-channels.

Before the RS-MSS experiment is started, the multi-LO-CS transform and the multi-LO-zero-input-CS response of the receiver are measured. During this measurement, the host computer commands the signal generators such that the desired CSR is input to the receiver.

After the CSR model of the receiver is measured, RS-MSS (./rs_mss script) and S-MSS (./s_mss script) are executed to estimate the CSR of the signal at the input of the receiver. Two example results are presented below.

Figure 6.12 compares the output of S-MSS and RS-MSS. The plot in the left is obtained while two signals with power level -25 dBm and -45 dBm are input to the receiver at 907 MHz and 929 MHz, respectively. The results show RS-MSS providing improvements of more 20 dB at the first channel. The plot in the right is obtained while three -30 dBm signals are input to the receiver at 901 MHz, 923 MHz and 929 MHz. The result shows that RS-MSS provides significantly more accurate measurement compared to S-MSS.

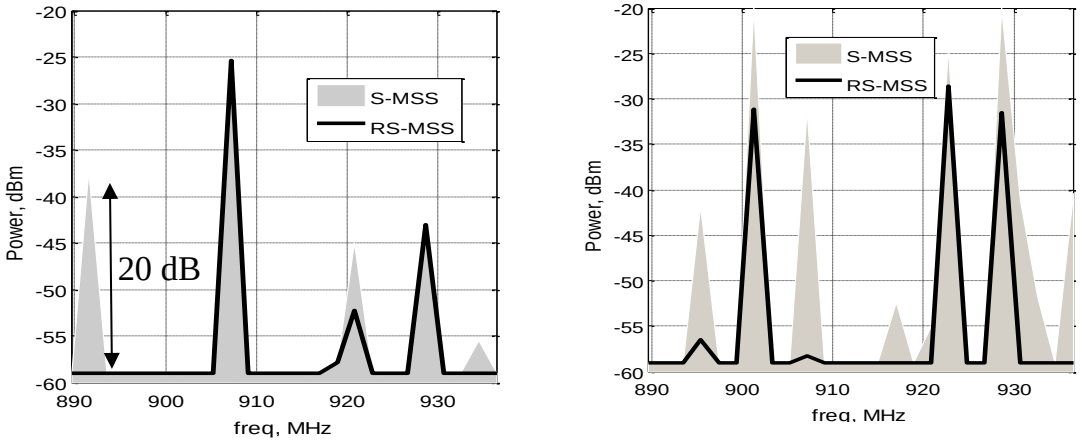

Figure 6.12 Comparing S-MSS with RS-MSS: (left) measuring a spectrum containing a -25 dBm signal at 907 MHz and -45 dBm signal at 929 MHz, (right) measuring a spectrum containing three signals -30 dBm signals at 901 MHz, 923 MHz and 929 MHz.

The results in Figure 6.12 confirm the benefits of RS-MSS over S-MSS. The fact that the overall system is functional on hardware also confirms the practical validity of the CSR-based receiver modeling technique presented in Chapter 3.

In poorly-selective receivers, the effects of IQ imbalance and aliasing are significant. The discussion in Chapter 5 showed how these impairments can degrade the accuracy of multi-band spectrum sensing in poorly-selective receivers. The above results demonstrate that RS-MSS can clean the products of RF impairments from a spectrum sensing data. This proves that RS-MSS is a viable method to sense the spectrum when a poorly-selective receiver is employed.

6.4.3 Demonstrating the operation of the Cognitive Engine

The other experiment demonstrates the operation of the cognitive engine. The experiment uses the same set-up as shown in Figure 6.10 except that only one, instead of three, signal generators are used. The ./cog_rf script is used to run this experiment.

In this experiment, the desired channel is assumed to be channel 13; and it is set to be vacant at all times. Consequently, the power level measured in the desired channel is always expected to be equal to the noise-floor. This power level exceeds the noise floor only if receiver impairments cause neighboring-channel signals to spill into the desired channel.

The experiment measures the power level in the desired channel at the output of the ADC. The experiment is carried out by injecting a narrow-band signal in to the receiver. The channel of the input signal changes every five seconds. Each one of the 24 channels, except the desired channel, has equal chance of hosting the input signal. As stated above, the desired channel (channel 13) is always vacant in the received spectrum. As the frequency (channel) of the input signal changes, the cognitive engine adjusts the sampling and the LO frequencies of the RF front-end such that the power in the desired channel does not exceed the noise floor by more than 4 dB. The experiment is carried out for 500 time-steps; and a time-step is equal to 5 sec. Figure 6.13 shows the result for the first 150 time-steps.

The upper two plots trace sampling and LO frequencies of the RF front-end with respect to time. The plots show that the cognitive engine is constantly changing the settings of the receiver as the state of the spectrum changes. It can be noted that the cognitive engine is using only the third and fourth LO frequency options in this experiment. This is reasonable because the third and the fourth LO frequency options are the closest to the desired channel – channel 13 (see Figure 6.3).

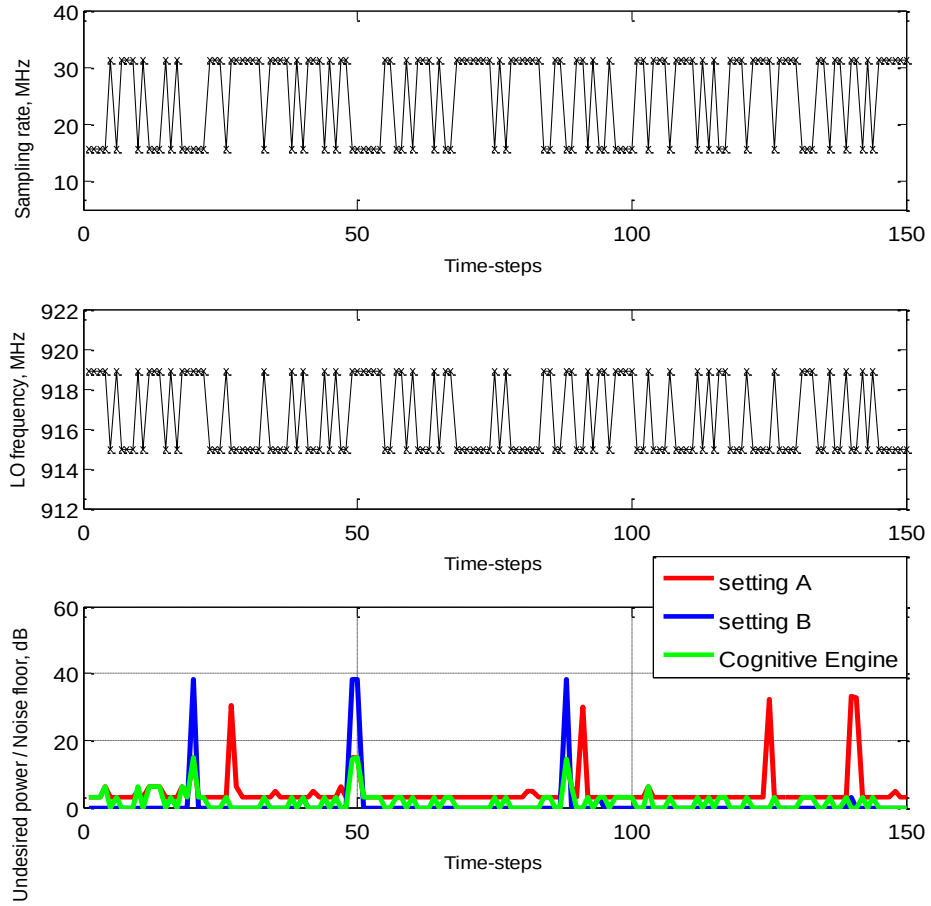

Figure 6.13 The CogRF operation.

The lower plot shows the power level measured in the desired channel. The power level measured using a cognitive engine is compared with that of two different fixed RF front-end settings. The first setting (setting A) uses the third LO frequency while the second setting (setting B) uses the fourth LO frequency. Both setting use the first sample-rate option.

The result shows that spikes occur at certain time-steps; especially when a fixed RF front-end setting is used. These spikes correspond to a dropped-calls or

dropped-connections in the desired channel. If cognitive engine is employed, however, the spikes are less aggressive and rare. This is because the cognitive engine helps the receiver to avoid a setting that will cause a high undesired power level in the desired channel.

From 500 time steps, the cognitive engine was found to correctly select the best RF front-end setting 61.8% of the time, and either the best or the second best setting 99.4% of the time. These results demonstrate the functionality of the cognitive engine (and CogRF). Further, the result also show the cognitive engine can improve the reliability of a communication link by minimizing or avoiding the effects of neighboring-channel signals.

6.4.4 Benefit of CogRF in Poorly-selective Receivers

The previous experiment showed that the cognitive engine can reduce the effect of neighboring-channels on the desired signal. This experiment also shows that CogRF can minimize the probability of communication outage due to interference from neighboring-channel signals.

The effects of neighboring-channel signals is significant only in poorly-selective receivers. In this experiment, up to three different signals are input into the receiver. The frequency of the input signals is varied every 5 sec. The desired channel is assumed to be channel 13; and it is set to be vacant at all times. Otherwise, each of the 24 channels has equal chance of hosting an input signal.

In this experiment, a CogRF enabled pre-selector-less receiver is compared with a traditional (non-CogRF) pre-selector-less receiver, and a traditional selective receiver. In non-CogRF receivers, the LO frequency and the sampling-rate are fixed at 915 MHz and 15.625 MHz respectively. In CogRF enabled

receivers, however, the frequency plan of the receiver changes in accordance to the change in state of the received spectrum.

An actual pre-selector is not employed in this experiment; rather, the pre-selector is emulated by controlling the power levels of the signal generators' outputs. The exact profile of the emulated pre-selector is shown in Figure 6.14. The power levels of the signal generators' output is lowered from the reference level by the attenuation level shown in the figure. The reference level (0 dB level) in Figure 6.14 is equal to -25 dBm.

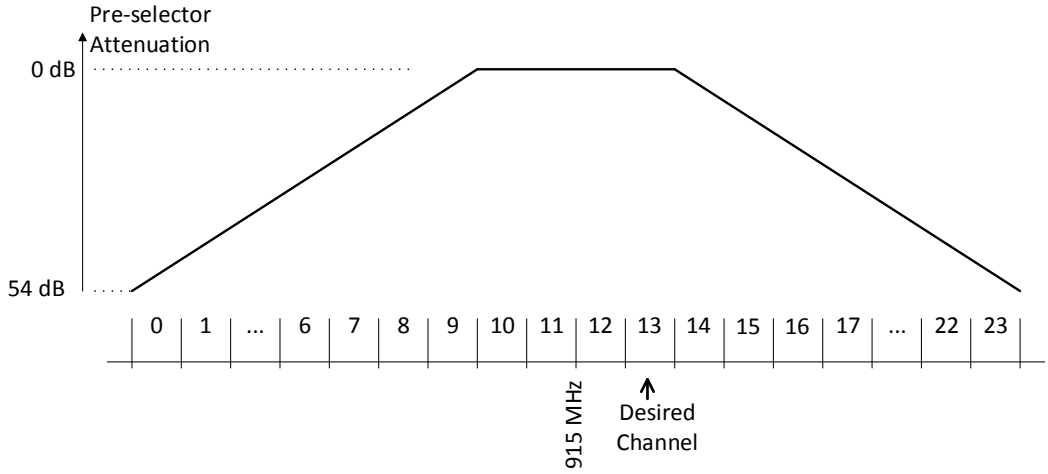

Figure 6.14 Pre-selector profiles used in CogRF experiment.

In this experiment, probability of outage, or probability of communication outage is used as a metric to compare the performance of four types of receivers. An outage is said to occur if the power level in the desired channel exceeds the noise-floor by more than 5 dB.

The results are presented in Figure 6.15. The results show that a traditional (non-CogRF) pre-selector-less receiver has poor dropped-connection performance.

The performance also degrades as the occupancy of the spectrum increases. As discussed throughout this dissertation, this is due to the interference caused by neighboring-channel signals. On the other hand, a selective receiver expectedly portrayed a good communication outage performance. It is also shown that the performance of a selective receiver slightly improves by incorporating CogRF. This was observed from simulation-based results as well (see Table 4.3).

Figure 6.15 shows that CogRF has significant benefit in a pre-selector-less receiver. The probability of outage (dropped-connections) performance is shown to improve by an order of magnitude in pre-selector-less receivers due to CogRF. This result confirms that CogRF can enable a poorly-selective receiver to behave like a highly-selective receiver.

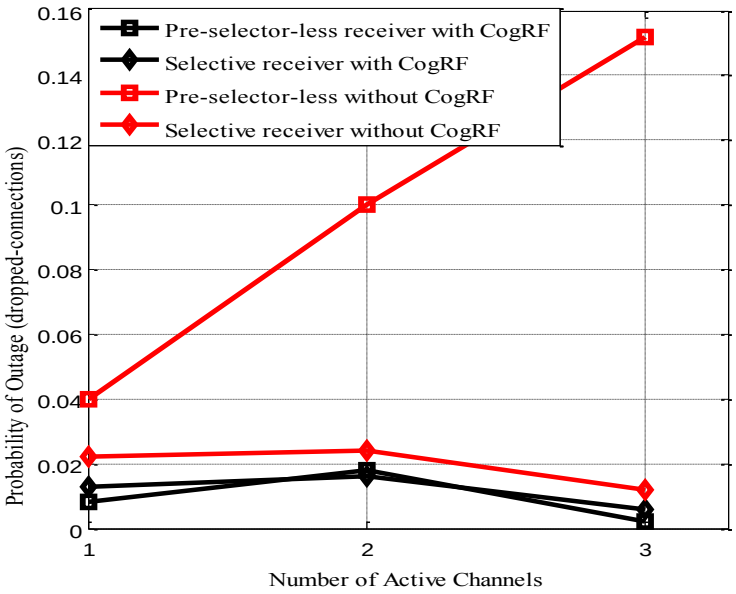

Figure 6.15 Comparing the performance of CogRF based pre-selector-less receiver with that of a selective receiver. A receiver is said to be "selective" if its pre-selector uses the filter profile shown in Figure 6.14.

The performance of CogRF is measured in the presence of only three or less active neighboring-channels. This is only because only three signal generators were available in the laboratory. The performance of CogRF in more energetic spectrums can be predicted using simulation.

6.5 Chapter Summary

This chapter documents the implementation of CogRF. CogRF is implemented on Wireless @ Virginia Tech's PicoRF platform. The details of the software and hardware subsystems of this implementation are presented in this chapter.

This chapter also presents the results obtained from three experiments that are carried out using the CogRF implementation. The first experiment measures the practical performance of the spectrum sensing mechanism that is developed in Chapter 5. Because the mechanism corrects for the effects of receiver impairments, it is shown to provide accurate spectrum sensing data. The measurement shows that the developed mechanism provides up to 20 dB improvement in accuracy compared to a spectrum sensing mechanism that does not correct for the effects of receiver impairments.

The second experiment investigates the operation of the cognitive engine that is designed in Chapter 4. The experiment clearly shows that the cognitive engine enables the receiver to "dodge" interference spikes that are caused by the appearing of a strong neighboring-channel signals in the spectrum. The cognitive engine is shown to adjust the receiver's local-oscillator and sampling frequencies to diminish the effects of neighboring-channels on the desired signal.

The last experiment measures the practical benefits of the CogRF in terms of improving the performance of poorly-selective receivers. The experiment shows that CogRF improves the communication outage performance of poorly-selective receivers. CogRF is shown to reduce the rate of communication outage from 16% to less than 1% in a pre-selector-less receiver. Under the same spectrum scenario, a selective receiver presented a communication outage performance of about 1.5%. This result confirms that CogRF indeed enables a poorly-selective receiver to behave similar to a highly-selective receiver.

Chapter 7

Addressing Strong Neighboring-Channel Signal

As it is stated in Chapter 3, Channelized Spectrum Representation (CSR) modeling technique is valid under the assumption that the receiver is ideally linear[14], which means, the power levels of all neighboring-channel signals are assumed to be within the linear region of the receiver. Because CogRF is designed based on CSR-modeling technique, it is expected to malfunctions whenever the received spectrum contains a signal that is strong enough to enter the non-linear

[14] This statement indicates that undesired non-linearities (strong and weak non-linearities) are neglected in the previous chapter. It is not implying that inherent non-linearities of the mixer and ADC are also neglected. Accurate definitions of the "inherent non-linearity" and "undesired non-linearly" are provided under Appendix E.

region of the receiver. Receiver non-linearity[15] causes a cross-modulation between neighboring-channel signals and the desired signal; and the effects of cross-modulation cannot be resolved by adjusting the frequency plan of the receiver.

The spectrum occupancy model in Section 3.5 suggests that strong signals are generally rare and they are not likely to originate from the desired signal's network. However, within the newly introduced spectrum management scheme [2], civilian wireless operations can share bands with military radars. The radar signals are often very high-powered. They can easily saturate any receiver operating in the same band or a poorly-selective receiver operating in an adjacent band. Similar problems may also occur in cellular systems at 600 MHz that exist close to TV stations.

In this chapter, a scenario in which a desired weak signal is received along with a strong neighboring-channel signal is considered (see Figure 7.1). Both the weak and the strong neighboring-channel signal are assumed to be within the reception bandwidth of the receiver. The term P_{sat} in Figure 7.1 represents the clipping (saturation) level of the receiver. This level is shown to be exceeded by the strong undesired signal. As it will be discussed in this chapter, the desired signal will be distorted by the non-linearity effects of the strong neighboring-channel signal.

[15] The term "non-linearity" in this chapter exclusively refers to undesired non-linearity (see Appendix E)

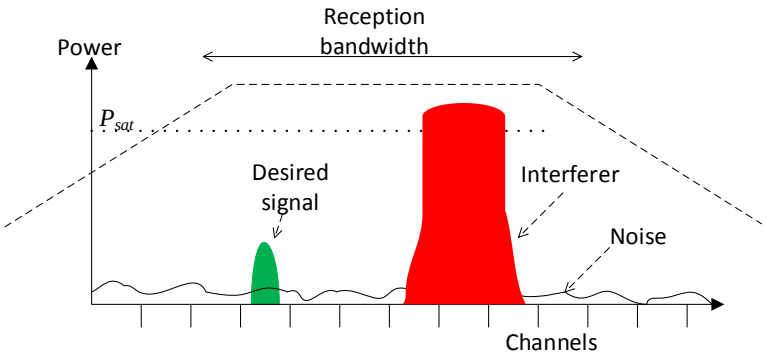

Figure 7.1 Spectrum scenario assumed in this chapter.

Traditionally, strong signals are addressed using automatic gain control (AGC). That is, AGC is used to avoid strong non-linearity distortions at the expense of the signal to noise ratio (SNR) of the desired signal. Using an AGC mechanism, the gain of the LNA is lowered whenever a strong signal is detected in the spectrum. However, AGC pushes the weak desired signal down into the noise floor and descensitizes the receiver as it attempts to fit the strong undesired signal into the dynamic range of the receiver.

This chapter analytically investigates the scenario in Figure 7.1. Then, two methods that can minimize the effect of the strong undesired signal with minimal penalty on the SNR of the desired signal are developed and verified using simulations. One of the developed methods is also demonstrated using hardware-based experiment.

The outline of this chapter is as follows. Section 7.1 presents a brief review on receiver non-linearity. Analytical model for the scenario in Figure 7.1 is developed in Section 7.2. Section 7.3 describes the detail of the methods that are proposed to address the effects of strong signals. Section 7.4 and Section 7.5 present a simulation and hardware-based evaluation of the methods, respectively.

7.1 Review of Receiver Non-Linearity Models

Receiver non-linearity[16] is a mixture of strong and weak non-linearity. The main difference between the two is that weak non-linearity is a small-signal characteristics while strong non-linearity is a large-signal characteristics. In Figure 7.2, the weak and strong non-linearity regions of a receiver are illustrated on a third-order intercept graph [11]. According to the figure, weak non-linearity occurs when the received signal is moderately strong. Strong non-linearity occurs when the received signal is within the saturation region of the receiver.

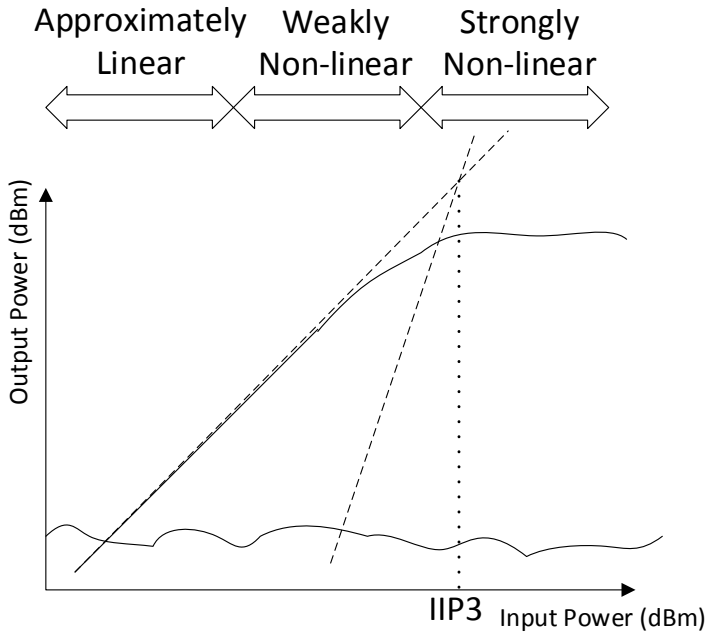

Figure 7.2 Non-linearity regions of a receiver.

[16] As it is stated above, the term "non-linearity" refers to undesired non-linearity in this chapter (see Appendix E)

Weak non-linearity is the most widely studied type of non-linearity [109]. The effects of weak non-linearity include odd and even order intermodulation distortions. Intermodulation distortions occur when two strong signals produce an intermodulation product within the desired channel. The other type of weak non-linearity distortion occurs when a weak desired signal arrives at the input of the receiver along with an undesired strong signal. The envelope of the strong signal distorts the desired signal by modulating the gain of the receiver [12].

On the other hand, strong non-linearity is caused by the limitedness of the voltage and current biases of the receiver. For this reason, strong non-linearity is generally independent of the small signal attributes of the receiver. Strong non-linearity can be quantified using parameters such as the input referred saturation power (P_{sat}), which denotes to the clipping level of the receiver.

Circuit level linearization is typically used to address weak non-linearity. For example, Zhang *et. al.* [109] proposed a linearization technique that cancels the components of weak non-linearity distortion using a linear feedback. Aparin *et. al.* [110] also proposed a technique in which the biasing point of transistors is adjusted to obtain optimal weak non-linearity performance. Furthermore, Ding *et. al.* [111] and Zhang *et. al.* [112] proposed the use of auxiliary circuit paths to cancel the components of weak non-linearity distortion. Using these linearization techniques, sub-micron CMOS LNAs with IIP3 in excess of 10 dBm have been reported [111, 113]. However, because all these techniques are designed based on the small-signal characteristics of the receiver, they fail to address the effects of strong non-linearity.

Marshal [33, 34, 114] proposed a network-level technique which relaxes the linearity and selectivity specifications of receiver RF front-ends. In this technique, a communication link is established in a frequency band that is not only

unoccupied, but also less vulnerable to intermodulation products of neighboring-channels'. Marshal's experiments [114] showed that this technique can effectively relax IIP3 specification of the receiver.

In summary, techniques that can address weak non-linearity already exist in the literature. In contrast, strong non-linearity have not received similar level of research attention [109]. Perhaps, this is because received signals are rarely strong enough to cause strong non-linearity distortions in today's planned spectrum management scheme. However, strong non-linearity will become relevant in the new spectrum allocation scheme where commercial wireless services share spectrum with powerful government radars [115]. These radars often generate Mega and Giga-watts of RF power [116]. Hence, such radars may easily saturate a near-by receiver.

It should be noted that various works have been attempting to address the effects of strong non-linearity distortions (or clipping) in transmitters; more specifically, in power amplifiers. For example, Cha *et. al.* [117], Dinis *et. al.* [118] and Nikopour *et. al.* [119], studied the effects of clipping the desired (transmitted) signal in power amplifiers. Obviously, such studies assume the cases in which the clipping is primarily caused by the desired signal. This is contrary to the receiver scenario in which a neighboring-channel signal is the main cause of the strong non-linearity distortion (see Figure 7.1). Accordingly, the techniques that are developed to address strong non-linearity in transmitters cannot address the effects of strong non-linearity in receivers.

7.2 Modeling Receiver Non-Linearity

In this chapter, a non-linear receiver is modeled according to the block diagram shown in Figure 7.3. The first two elements after the antenna represent an LNA. The LNA is modeled as a cascade of a variable gain amplifier and a non-linear element. To simplify the analysis, the non-linearity of the receiver is attributed to the LNA only. The non-linearities of the mixer, the baseband filter and the ADC are neglected. This is because the gain in the LNA can be adjusted such that the signal remains within the linear region of the sub-sequent RF front-end elements. The third element in the chain represents an ideal the down-conversion mixer and an LO source that is tuned to the frequency of the desired signal. The next element represents an ideal ADC. The last element represents a low-pass filter implemented in the digital section of the receiver. The mixer and the ADC are assumed to be complex; that is, even though it is not explicitly shown in the figure, they contain real and imaginary paths.

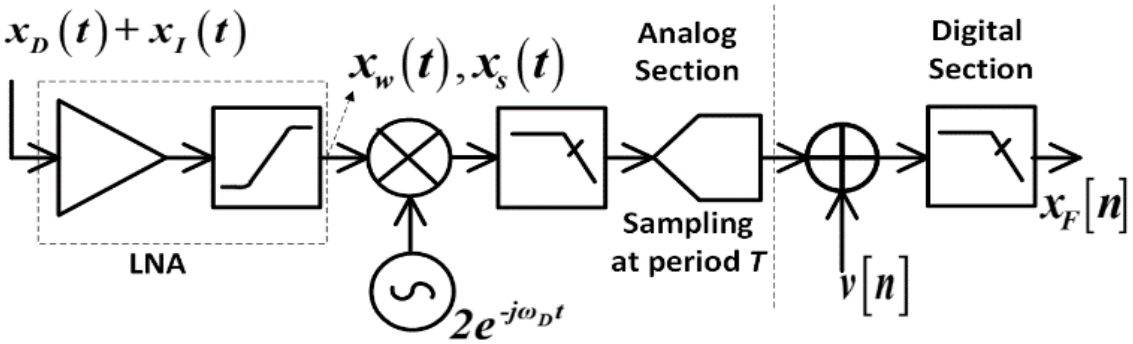

Figure 7.3. Block diagram of a non-linear receiver.

Consider $x_D(t)$ is a weak desired signal and $x_I(t)$ is a strong neighboring-channel signal. The terms $D(t)$ and $\theta_D(t)$ denote the amplitude and phase of the desired signal, respectively. Similarly, $I(t)$ and $\theta_I(t)$ denote the amplitude and phase of the strong undesired signal, respectively. In addition, let $\theta_D(t) = \omega_D t + \varphi_D(t)$ and $\theta_I(t) = \omega_I t + \varphi_I(t)$.

The receiver input is given by,

$$x(t) = x_D(t) + x_I(t) \tag{7.1}$$

and,

$$\begin{aligned} x_D(t) &= D(t)\cos\left(\theta_D(t)\right) \\ x_I(t) &= I(t)\cos\left(\theta_I(t)\right) \end{aligned} \tag{7.2}$$

The output of the LNA is $x_w(t)$ if the LNA is assumed to be weakly non-linear only; and $x_s(t)$ if the LNA is assumed to be strongly non-linear only. In reality, however, LNAs exhibit both weak and strong non-linearities. The distinction here is only to simplify the analysis. The output of the LO source is given by $2e^{-j\omega_D t}$. The digital filter is assumed to be selective enough to sufficiently reject the strong neighboring channel signal. The output of the digital-filter is denoted by, $x_F[n]$. In this chapter, for any analog signal $y(t)$, its digital version is given by $y[n] = y(t)|_{t=nT}$, where T is the sampling period of the ADC in Figure 7.3.

7.2.1 Modeling Weak Non-linearity

The power series is the simplest method that is used to model weakly non-linear RF front-end element. The output of a weakly non-linear element can be written as,

$$x_w(t) = \sum_{i=0}^{\infty} a_i x(t)^i \tag{7.3}$$

where $x(t)$ is the continuous time input to and $x_w(t)$ is the output of a weakly non-linear element. Typically, a_i is equal to zero for i greater than 3. In this research, we consider balanced RF front-end elements such that the even-index coefficients can be approximated by zero since they tend to be out-of-band [11]. Without loss of generality, it can also be assumed that $a_1 = 1$. Hence the output of a weakly non-linear LNA, $x_w(t)$ is given by,

$$x_w(t) = x(t) + a_3 x(t)^3 \tag{7.4}$$

Substituting (7.1) into (7.4),

$$x_w(t) = x_D(t) + x_I(t) + 3a_3 x_D(t)^2 x_I(t) + 3a_3 x_I(t)^2 x_D(t) + a_3 x_D(t)^3 + a_3 x_I(t)^3 \tag{7.5}$$

Considering that the desired signal is a weak signal and the digital filter has a sufficient selectivity, (7.5) can be simplified to,

$$x_F[n] = \left(1 + \frac{3}{2} a_3 I[n]^2\right) D[n] e^{-j\varphi_D} \tag{7.6}$$

7.2.2 Modeling strong non-linearity

The input-output characteristics of a symmetric strongly non-linear element can be modeled by (7.7).

$$x_s(t)=\begin{cases} V_o, & x(t)\geq V_o \\ -V_0, & x(t)\leq -V_o \\ x(t), & -V_o < x(t) < V_o \end{cases} \tag{7.7}$$

where $x_s(t)$ is the output of a strongly non-linear element. By noting that $x(t)$ and $x_s(t)$ are both periodic in the $\theta_I(t)$ domain with period 2π. Hence, Fourier series expansion of $x_s(t)$ with respect to $\theta_I(t)$ (not with respect to t) is given by,

$$\begin{aligned} x_s(t) &= \sum_{m=-\infty}^{\infty} C_m e^{+jm\,\theta_I(t)} \\ C_m &= \frac{1}{2\pi}\int_0^{2\pi} x_s(t) e^{-jm\,\theta_I(t)} d\theta_I(t) \end{aligned} \tag{7.8}$$

After substituting (7.7) into (7.8) and simplifying, $x_s(t)$ can be expressed as,

$$\begin{aligned} x_s(t) = {} & V_o\left[1-\frac{\beta(t)+\alpha(t)}{\pi}\right]+\frac{I(t)}{\pi}\left[\sin(\beta(t))-\sin(\alpha(t))\right] \\ & +\sum_{k=1}^{\infty}\frac{2V_o}{k\pi}\left[\sin(k\beta(t))+\sin(k\alpha(t))\right]\cos(k\theta_I(t)) \\ & +\sum_{k=2}^{\infty}\frac{I(t)}{(k+1)\pi}\left[\sin((k+1)\beta(t))-\sin((k+1)\alpha(t))\right]\cos(k\theta_I(t)) \\ & +\sum_{k=2}^{\infty}\frac{I(t)}{(k-1)\pi}\left[\sin((k-1)\beta(t))-\sin((k-1)\alpha(t))\right]\cos(k\theta_I(t)) \\ & +\frac{I(t)}{\pi}\left[\beta(t)-\alpha(t)+\frac{\sin(k\beta(t))+\sin(k\alpha(t))}{2}\right]\cos(\theta_I(t)) \\ & +\left\{\left[\frac{\beta(t)-\alpha(t)}{\pi}\right]+\sum_{k=1}^{\infty}\frac{2}{k\pi}\left[\sin(k\beta(t))-\sin(k\alpha(t))\right]\cos(k\theta_I(t))\right\}x_D(t) \end{aligned} \tag{7.9}$$

where,

$$\alpha(t)=\begin{cases}0, & I(t)\geq V_o\\ \cos^{-1}\left(\dfrac{V_o-x_D(t)}{I(t)}\right), & I(t)<V_o\end{cases},\quad \beta(t)=\begin{cases}0, & I(t)\geq V_o\\ \cos^{-1}\left(\dfrac{-V_o-x_D(t)}{I(t)}\right), & I(t)<V_o\end{cases}$$

The equation in (7.9) is an expanded version of (7.7). The two equations are compared using an arbitrary $x(t)$ in Figure 7.4. The plots in Figure 7.4 are obtained by setting $V_o = 2.0$ and computing summation terms in (7.9) only to $k = 10$. The plots in Figure 7.4 illustrate that the relation in (7.9) correctly depicts the input-output characteristics of the strongly non-linear element that is modeled by (7.7).

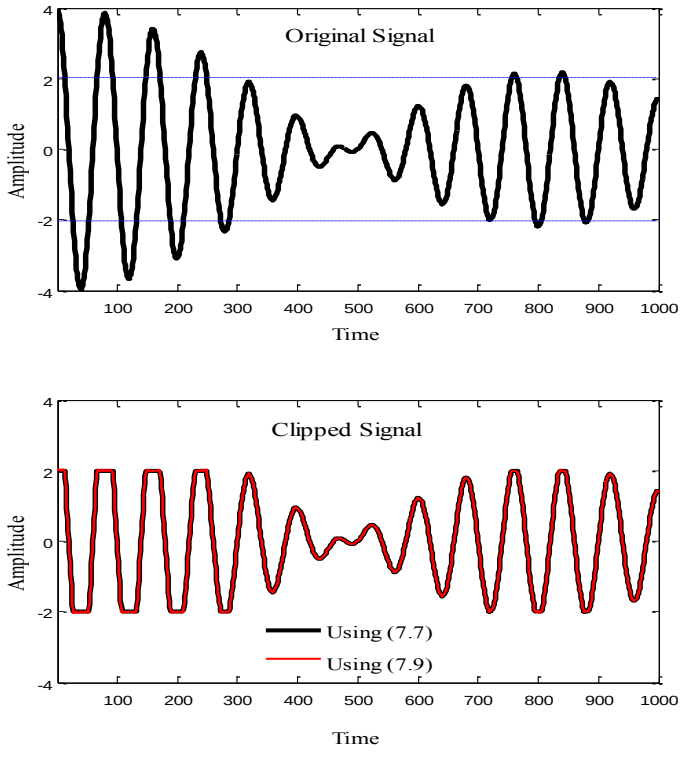

Figure 7.4. Verification of strong non-linearity formula.

Considering $V_o >> D(t)$, then, $\beta(t) \approx \pi - \alpha(t)$. By simplifying (7.9) accordingly, it can be shown that the output of the digital filter is,

$$x_F[n] \approx \left\{1 - \frac{2}{\pi}\alpha[n]\right\} D[n] e^{j\varphi_D} \tag{7.10}$$

In summary, both (7.10) and (7.6) can be written using the format,

$$x_F[n] \approx \gamma[n] D[n] e^{j\varphi_D} \tag{7.11}$$

$$\text{where, } \gamma[n] = \begin{cases} 1 - \frac{2}{\pi}\alpha[n], & \text{for strong non-linearity} \\ 1 + \frac{3}{2} a_3 I[n]^2, & \text{for weak non-linearity} \end{cases}$$

The following observations can be drawn from the above model;

- It can be noted that $0 \le \gamma[n] \le 1$ for both weak and strong non-linearites. Note that $a_3 < 0$ for balanced receivers [11].
- The term $\gamma[n]$ represents time-varying compression on the desired signal. For both weak and strong non-linearities, $\gamma[n]$ is a function of $I[n]$(the envelope of the undesired signal). This shows that the envelope of the strong undesired signal is distorting the weak desired signal by modulating the gain of the receiver.
- According to the above models, the strong signal does not cause any phase distortion on the desired signal.
- The receiver can demodulate and decode $x_F[n]$ with a lesser amount of error if it is not blind to the value of $I[n]$ (or $\gamma[n]$). The next section proposes the use

of an auxiliary receive path to measure $I[n]$ and provide the value to the modem in the receiver.

- The compression caused by weak non-linearity is very small. For a receiver with IIP3 equal to 10 dBm, an undesired signal with power level of -10 dBm produces less than 0.1 dB compression on a weak desired signal. Therefore, the focus of the forthcoming analysis will be entirely on strong non-linearity. The results and conclusions, however, can be extended to apply to weak non-linearity as well.
- In addition to revealing the characteristics of non-linear RF front-ends, this model is convenient to account the effects of RF non-linearity in baseband simulations. This study also uses this model in the simulations that are reported later in this chapter.

7.3 Addressing Strong Neighboring-Channel Signals

The plots in Figure 7.5 illustrate that clipping does not occur at all times. Hence, all the symbols of the desired signal are not compressed. Accordingly, when the AGC reduces gain to avoid clipping, the good SNR on would-be-uncompressed symbols will be sacrificed.

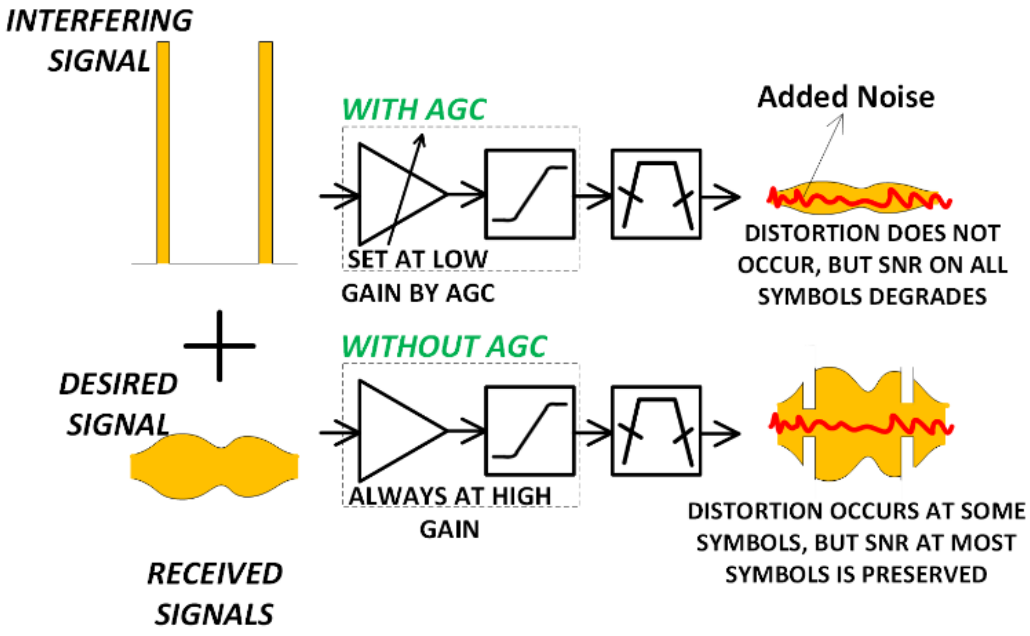

Figure 7.5 Comparison of AGC and non-AGC based receivers.

Instead of using AGC to lower the gain on the overall signal, the signal could simply be allowed to clip. Then, the effects of the clipping can be removed using the sub-sequent analog and digital filters in the receiver. Assuming that the information on the desired signal is error coded in the transmitter (which is typical in most digital communication systems), the symbols at which compression did not occur can be leveraged to estimate the transmitted information. This way, the proposed technique can provide a better Bit-Error-Rate (BER) and throughput performance compared to AGC based systems. These assertions are verified using simulations and hardware experiments that are presented later in this chapter.

Based on this idea, this section presents two types of non-AGC methods to address strong signals. The methods are called *Auxiliary-Path-Assisted Digital Correction* (APA-DC) and *Auxiliary-Path-Assisted Soft-Decoding* (APA-SD).

7.3.1 Auxiliary-Path-Assisted Digital Correction (APA-DC)

If the envelope of the strong signal is known in real-time, the effect of clipping on the desired signal can be removed by multiplying $x_F[n]$ by $1/\hat{\gamma}[n]$ in DSP, where $\hat{\gamma}$ is the estimate of the multiplicative distortion. This estimate can be obtained by using an envelope-tracking auxiliary receive path. The auxiliary receive path and the digital correction blocks are reddened in Figure 7.6.

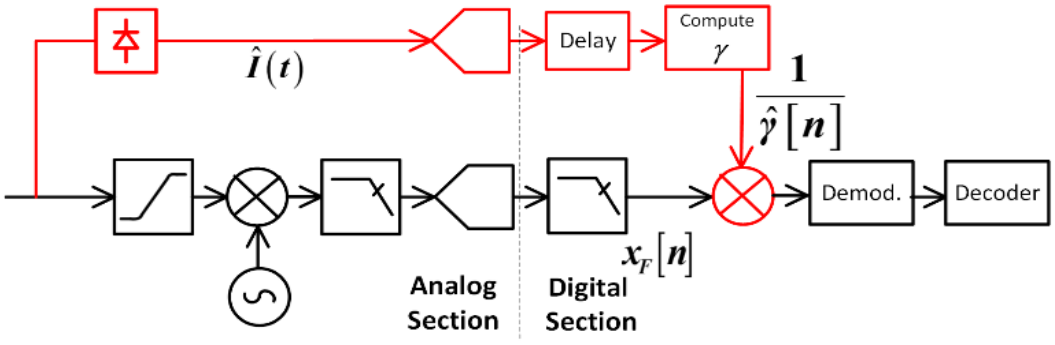

Figure 7.6. Auxiliary-path assisted digital correction.

The proposed technique does not attenuate the desired signal at every time point like an AGC. Rather, by allowing clipping, the symbols of the desired signal at which clipping occur are left to be compressed while the rest are preserved. If the desired signal is a digital communication signal, this technique is expected to provide better performance compared to AGC because it rightfully preserves the SNR of the symbols at which clipping does not occur.

Let $\frac{1}{\hat{\gamma}[n]} = \frac{1}{\gamma[n]} + \varepsilon$. Then, the input to the demodulator in Figure 7.6 is given by,

$$x_F[n] = D[n]e^{j\varphi_D} + \varepsilon D[n]e^{j\varphi_D} + v[n]\left(\frac{1}{\gamma[n]} + \varepsilon\right) \tag{7.12}$$

Accordingly, the digital-compensation in APA-DC has disadvantages because it causes the desired signal to self-interfere. It may also cause noise enhancement. Note that the digital compensation could cause significant phase distortion because compensating multiplication is carried out after noise is added to the signal.

The major short-coming of APA-DC can be attributed to a potential mismatch between the model that is used to compute $\hat{\gamma}[n]$ and the actual characteristics of the receiver. This mismatch causes APA-DC to introduce unpredictable amount of error on the desired signal during compensation. The compensation will be effective only when the model correctly reflects the characteristics of the receiver. However, the actual characteristics of the receiver may not be accurately known. Accordingly, APA-DC is difficult to implement on an actual hardware.

These short-comings inspired the development of an alternative to APA-DC called Auxiliary-Path-Assisted Soft-Decoding (APA-SD). APA-SD uses the value of $\hat{\gamma}[n]$ not for compensation purpose, but to inform a decoder about the quality of each received bit.

7.3.2 Auxiliary-Path-Assisted Soft-Decoding (APA-SD)

As shown in Figure 7.7, APA-SD does not compute $\hat{\gamma}[n]$ to use it for digital compensation purposes. Rather, the envelope of the neighboring-channel that is measured by the auxiliary path ($\hat{I}[n]$) is used by the decoder to weight the information that is contributed by each received bit. Hence, this scheme allows the

decoder to obtain better estimate of the transmitted information by deemphasizing the contribution of compressed (or "bad") bits in the estimation process. Furthermore, APA-SD does not suffer from self-interference and noise enhancement that are exhibited in APA-DC. Unlike AGC, and like APA-DC, APA-SD does not sacrifice the good SNR in uncompressed symbols.

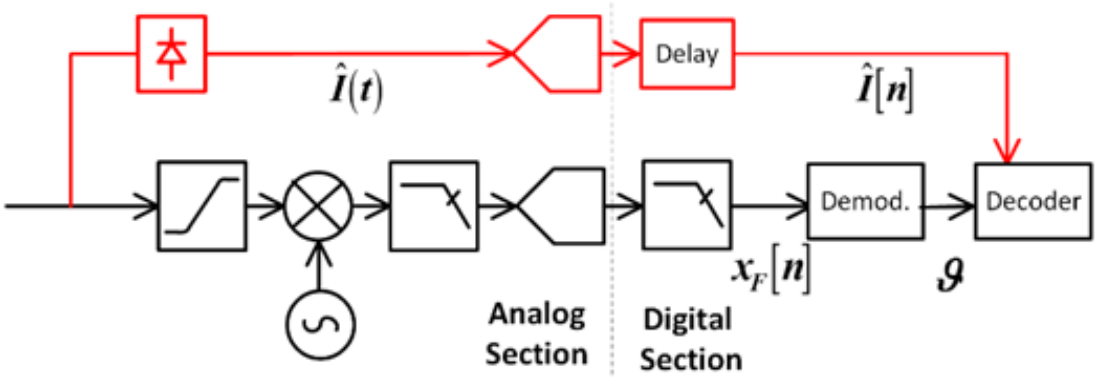

Figure 7.7 Auxiliary-path-assisted soft-decoding.

In this study, a soft-decoder for convolutional code is considered [76]. Unlike hard-decoders, a soft-decoder takes a confidence value, ϑ, instead of the binary value of the received bit as its input (see Figure 7.7). A soft-decoder generally performs better than hard-decoders [18].

In this study, a confidence value that is input to the soft-decoder ranges from 0 to 7 (three bit representation); where 0 represents the most confident 0, and 7 represents the most confident 1. In APA-SD, the value of $\hat{I}[n]$ is used to modify the confidence value of a bit that is received at n^{th} time-point according to the following rule;

$$\begin{aligned}
&\text{If } \hat{I}[n]/V_o \le TH \text{ , then } \vartheta_{mod} = \vartheta \\
&\text{If } \hat{I}[n]/V_o > TH \text{ and } 4 \le \vartheta \le 7 \text{ , then } \vartheta_{mod} = 4 \\
&\text{If } \hat{I}[n]/V_o > TH \text{ and } 0 \le \vartheta \le 3 \text{ , then } \vartheta_{mod} = 3
\end{aligned} \tag{7.13}$$

where TH is a threshold value that is a function of the modulation (i.e. 16-QAM, 64-QAM, etc.).

In other words, the confidence value of a bit is reduced to the lowest level if the symbol that was carrying the bit was distorted due to clipping. This allows the decoder to obtain better estimate of the transmitted information because it fairly weights the contribution of the extrinsic information that is provided by each received bit. The value of TH also depends on the index of the bit per symbol (for example, 1st out of the 4 bits of a 16 QAM symbol). Noting that the compression does not cause any phase variation on the signal, it can be inferred that $TH = \infty$ for bits that cannot be flipped due to amplitude distortion/compression only.

To further illustrate the operation of APA-SD, consider a multi-level Pulse-Amplitude-Distortion (PAM) signal that is shown in Figure 7.8. For this constellation, an amplitude compression corresponding to $\gamma < 2/3$ likely causes 'D' transmitted symbol to be appear as 'C', or 'A' transmitted symbol to appear as 'B', at the input of a demodulator (symbol de-mapper). From (7.10), it can be shown that $\gamma = 2/3$ corresponds to $I[n]/V_o \approx 1.15$. Also note that amplitude compression causes only the second bit to be flipped during de-mapping, while the first bit cannot be affected by amplitude compression unless SNR is low. Accordingly, for this modulation scheme, $TH = \infty$ and $TH = 1.15$ are reasonable values for the first and second bits of a given symbol, respectively.

Figure 7.8 shows an example in which ‘A’ symbol is transmitted and due to compression, the received symbol appears closer to ‘B’ than to ‘A’. For a regular soft-decoding procedure, the received symbol appears to correspond to ‘B’, with high-confidence. However, a receiver employing APA-SD, lowers the confidence of the second bit to the minimum possible value before soft-decoding. Hence, this scheme ensures that the compressed symbols do not mislead the decoder.

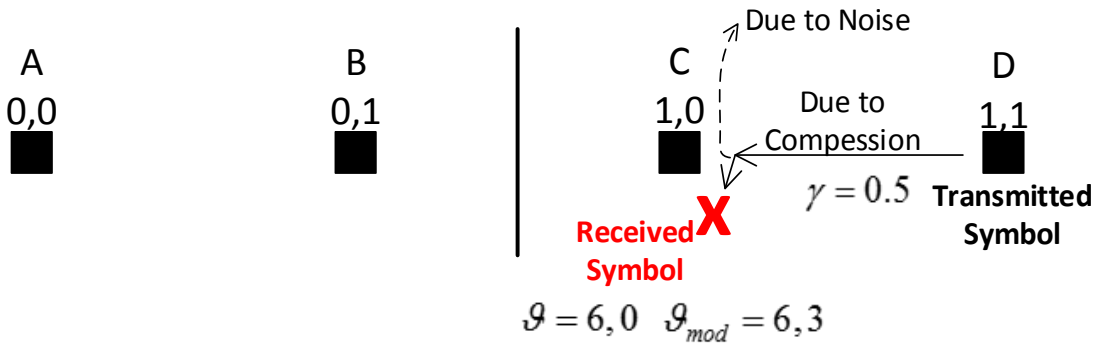

Figure 7.8 Illustration of APA-SC

7.4 Simulation-Based Evaluation

In this simulation, the performance of APA-DC and APA-SD receivers are compared with that of an AGC-based receiver and a regular non-AGC-non-auxiliary-path receiver. The non-AGC-non-auxiliary-path receiver employs neither an AGC nor an auxiliary-path. It demodulates the raw output of the digital-filter in Figure 7.3.

The undesired strong signal is a pulsed (radar) signal that is modulated by a carrier. In this simulation, receiver non-linearity is modeled as given in (7.10). The distortion on the desired signal is computed from the envelope of the undesired

signal (the radar signal). In this simulation, compression due to the undesired signal is quantified as,

$$C = 20\log\left(\frac{\max I(t)}{V_o}\right) \tag{7.14}$$

The AGC sets the gain of the LNA such that the overall received signal (or $x(t)$ in (7.1)) avoids distortion by nearly missing the clipping level of the receiver. In other words, an AGC based receiver lowers the gain of the LNA by *C* dBs to fit the interfering signal into the dynamic range of the receiver. In doing so, AGC-based receiver also lowers the SNR of all symbols of the desired signal by up to *C* dBs.

To demonstrate the penalty associated with using AGCs, a simulation is used to compare the Bit-Error-Rate (BER) performance of APA-DC, APA-SD, AGC and non-AGC-non-auxiliary-path receivers. The SNR on the auxiliary-path (the ratio of the envelop signal's power to the additive noise signal's power) is set to be 20 dB. The pulse width of the radar signal (the neighboring-channel interferer) is assumed to be equal to the duration of a single symbol in the desired signal. Similarly, the period of the radar signal is set to be equal to 50 symbol intervals in the desired signal.

The desired signal is packetized, and each packet contains 1000 bits. It is coded using a 4/5-rate convolutional code. A 1/2-rate convolutional encoder is punctured to set the rate of the actual code to 4/5. In the receiver, a soft-Viterbi-decoder is employed.

The simulation measures BER by varying SNR, while the peak power of the radar signal is set to be 8 dB above the saturation level of the receiver (*C* = 8 dB).

A receiver for which C = 0 dB is also simulated to serve as a benchmark. Figure 7.9 and Figure 7.10 show BER versus SNR curves for 16-QAM and QPSK signals, respectively.

The results confirm that APA-SD performs significantly better than AGC. Up to 8 dB improvement in performance is obtained, which is the same as the compression level. Furthermore, the performance of APA-SD is comparable to the case in which there is no compression. This implies that APA-SD enables the receiver to behave indifferent to the presence of the radar signal.

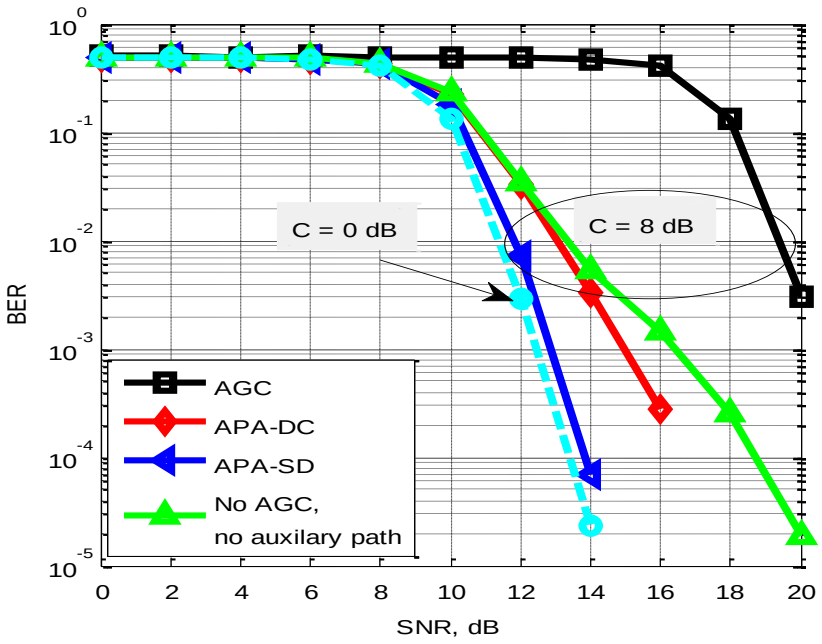

Figure 7.9 BER versus SNR for a 16-QAM signal.

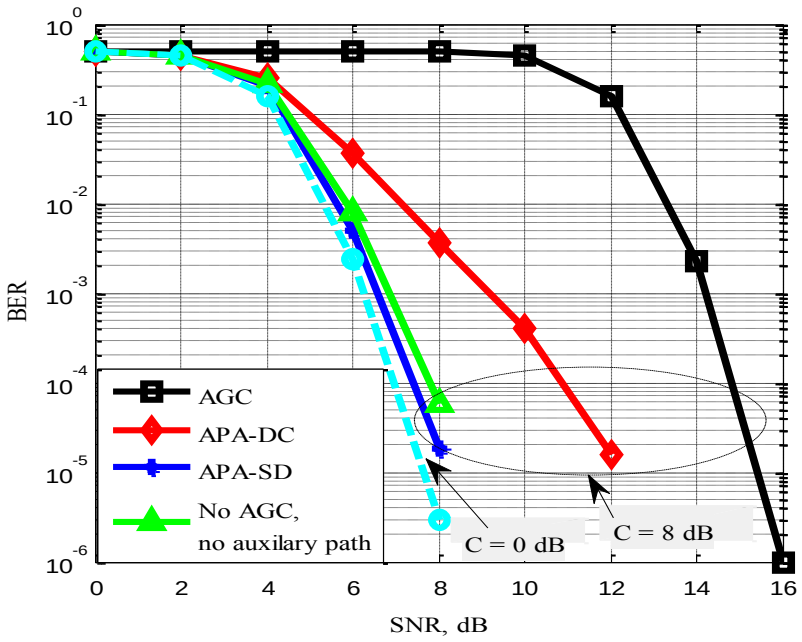

Figure 7.10 BER versus SNR for QPSK signal.

Due to self-interference and noise enhancement during the compensation stage, APA-DC performs inferior to APA-SD. No-AGC-no-auxiliary-path receiver performs the same as APA-SD for QPSK. This is because amplitude compression does not cause flipping of bits in QPSK signals. Furthermore, the compression by the RF front-end appropriately lowers the confidence level of compressed bits at the input of the soft-decoder. Hence, additional adjustments from auxiliary path are not necessary. For 16-QAM signal, however, compression causes some of the bits to flip. Hence, no-AGC-no-auxiliary-path receiver performs inferior to APA-SD for 16-QAM signal. This shows that auxiliary path has benefit in 16-QAM based communication. In general, the results imply that the auxiliary path has significant benefit particularly in multi-level-modulation-based communication systems.

The above results also confirm that lowering the gain of the receiver is not a viable strategy to address the effects of radar signals. This is because indiscriminately gain reduction sacrifices the good SNR at undistorted symbols.

7.5 Hardware-based Experiment

In this section, the performance APA-SD method is investigated using a hardware-based experiment. The block diagram of the experiment set-up is detailed in Figure 7.11. The picture of the experiment set-up is shown in Figure 7.12. The experiment uses USRP1 [120] as the receiver; with SBX daughter-board attached to side-B as the main receive path, and LFRX daughter-board attached to side-A as an auxiliary receive path. The evaluation board of Texas Instrument's LMH2121 power-detector is used as the envelope-detector. The output of the envelope-detector is input to LFRX on the receive USRP. Because the strong non-linearity characteristics of SBX daughter-board is not fully characterized, an external RF limiter with a known P_{sat} (P_{sat}=0 dBm) is used at the input of the main path. A picture of the actual experiment set-up is shown in Figure 7.12.

The desired signal is generated by another USRP1 at 900 MHz. A signal-generator is used to generate a pulsed interferer at 850 MHz. The desired signal is a 16-QAM signal with raised-cosine pulse shaping. The transmitted signal includes a preamble containing a constant signal and a Zadoff-Chu sequence [121]. The preamble is added to the transmitted signal to facilitate frequency and timing synchronization at the receiver. The received signal is captured using GNURadio file-sink and post-processed in Matlab. The signal is received at high SNR to minimize the effects of synchronization error in results of the experiment.

To obtain the desired level of SNR in the received signal, noise is added in Matlab after synchronization and matched filtering stages.

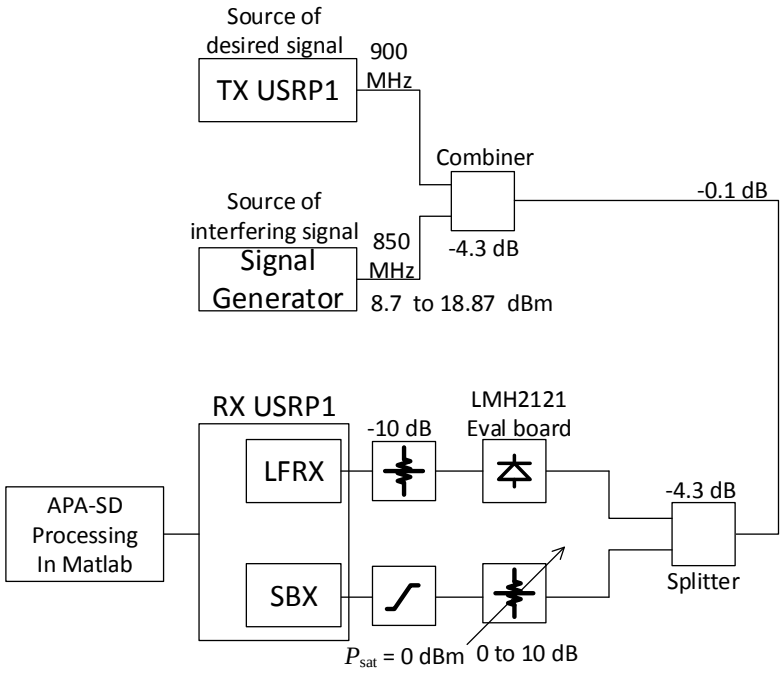

Figure 7.11 Experiment set-up for APA-SD.

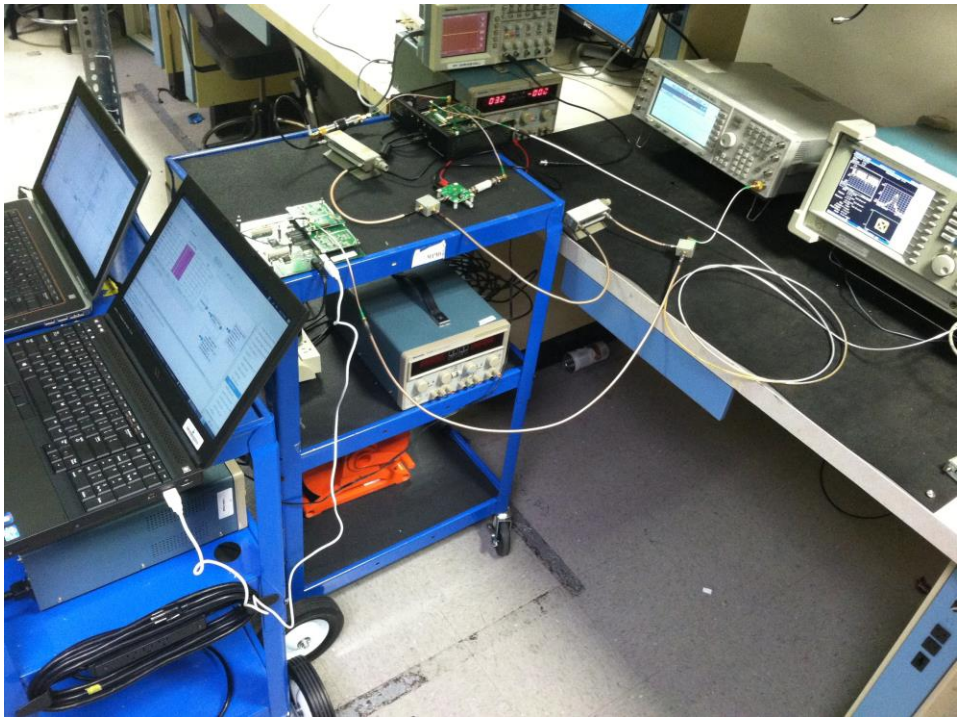

Figure 7.12 Picture of the APA-SD experimentation set-up.

The hardware experiment also uses QPSK and 16-QAM based desired signals. The desired signal is packetized, and each packet contains 1000 bits. The transmitted signal is coded using a 4/5-rate convolutional code. A 1/2-rate convolutional encoder is punctured to set the rate of the actual code to 4/5. Before the convolutional encoding, the transmit bits encoded using a 24 bit Cyclic-Redundancy-Checker (CRC). In the receiver, a soft-Viterbi-decoder is employed.

A pulsed (radar) signal is used as interferer. The pulse-width of the interferer is set to be equal to a single symbol duration. Similarly, the period of the interferer is set to be 50 times the symbol duration of the desired signal.

To compensate for the cumulative loss of the combiner, the splitter and the cables (which is equal to -8.7 dB), the peak power of the interferer is varied

between 8.7 dBm and 18.7 dBm. Hence, if the gain of the variable attenuator is set to 0 dB, the peak power of the interferer at the input of the RF limiter varies between 0 and 10 dBm.

The variable attenuator block is inserted to emulate the effect of AGCs. In AGC mode, the gain of this block is set such that the power level at the input of the limiter does not exceed 0 dBm (P_{sat}). In APA-SD and no-AGC-no-auxiliary-path mode, the gain is set to 0 dB.

The throughput performance of APA-SD is measured while the peak-power of the interferer signal is varying from 8.7 dBm to 18.7 dBm (0 dBm to 10 dBm at the input of the limiter). This corresponds to varying C in (7.14) from 0 to 10 dB. For comparison purposes, the measured result is compared against what is obtained using simulation. The simulation uses (7.10) to model the non-linearity of the RF front-end.

The throughput performance of APA-SD is measured while the peak-power of the interferer signal is varying from 8.7 dBm to 18.7 dBm (0 dBm to 10 dBm at the input of the limiter). This corresponds to varying C in (7.14) from 0 to 10 dB. For comparison purposes, the measured result is compared against what is obtained using simulation. The simulation uses (7.10) to model the non-linearity of the RF front-end.

In this simulation, throughput is calculated as,

$$Througput = M\,R\,(1 - P_e) \tag{7.15}$$

where M is the modulation index; R is the coding rate, and P_e is the packet error rate. M is 2 for QPSK and 4 for 16-QAM. A 4/5-rate code is used in the desired signal (R = 4/5). A received packet is stated to be “error” if it fails CRC check.

The results of the experiment are presented in Figure 7.13 and Figure 7.14. Figure 7.13 presents the result for 16-QAM signal, and Figure 7.14 presents the result for QPSK signal. The hardware-based results are compared with that of simulation-based results. The simulation uses (7.10) to model the receiver RF front-end.

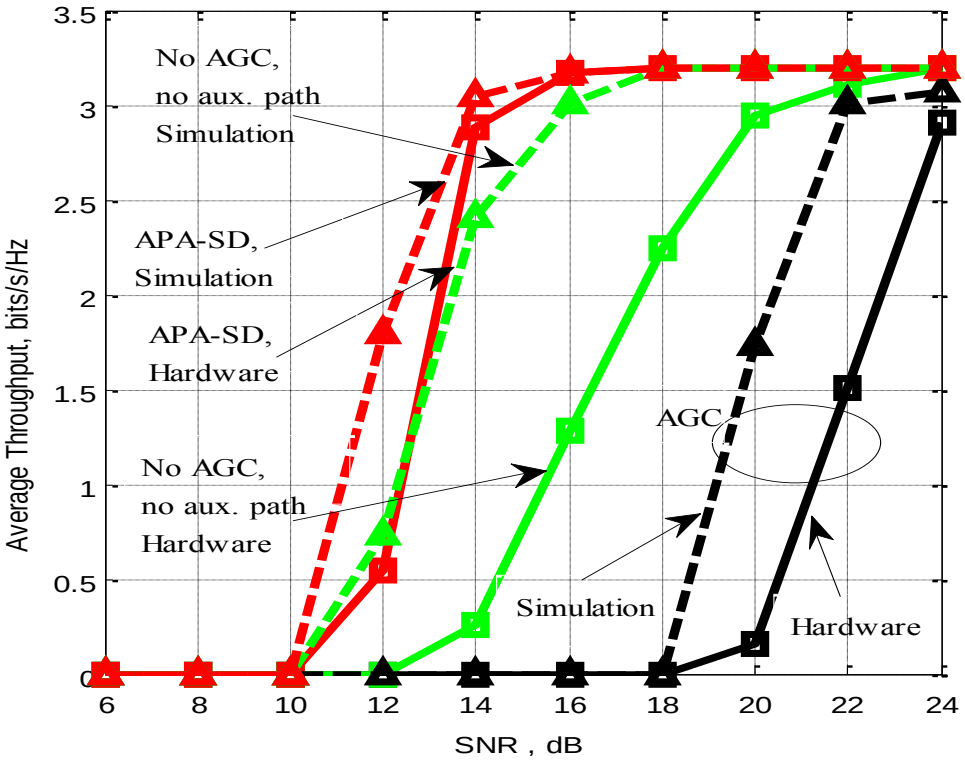

Figure 7.13 Throughput versus SNR for 16-QAM signal, measured through simulation and hardware-based experiment (C = 8 dB)

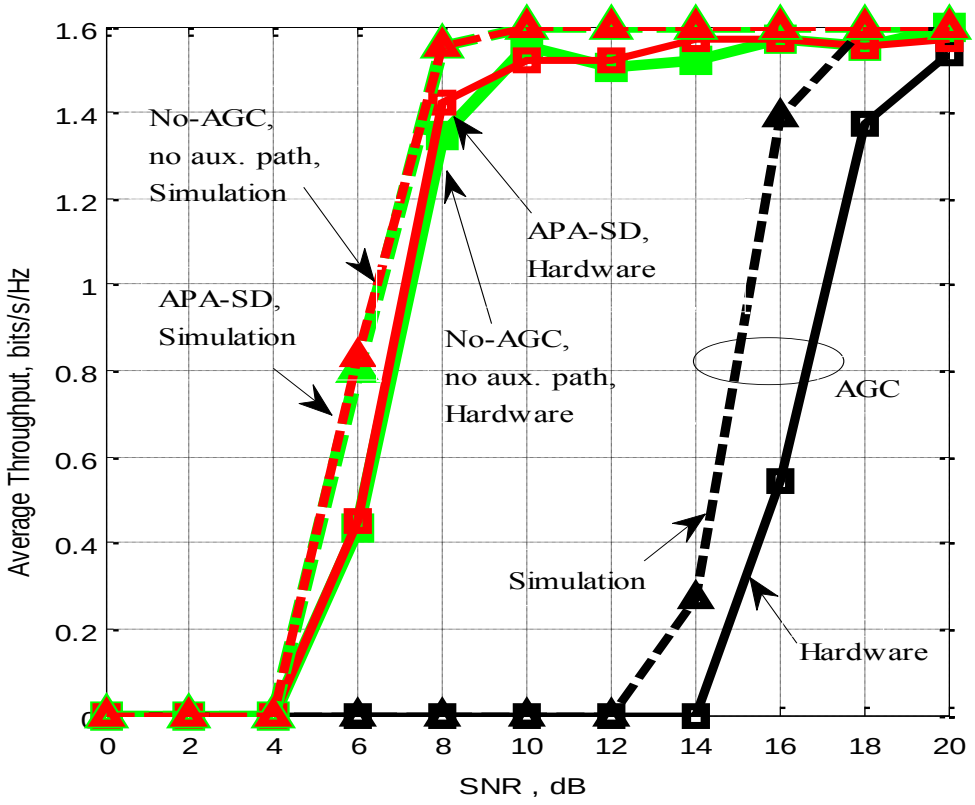

Figure 7.14 Throughput versus SNR for QPSK signal, measured through simulation and hardware-based experiment (C = 8 dB)

The above results confirm the observations that were obtained using simulation-based experiments in the previous section. APA-SD is shown to have more than 8 dB advantage over AGC. In addition, for 16-QAM signal, APA-SD is shown to have about 3 dB advantage over the no-AGC-no-auxiliary path receiver. But the performance of the two is the same for QPSK receiver. As it was described previously, this is because amplitude compression does not cause flipping of bits in QPSK signals.

The performance obtained using simulation is also shown to be slightly better than the performance obtained from hardware. This is because the model that is

used in the simulation considers the effect of strong non-linearity only. The characteristics of the RF limiter is assumed to be purely linear between the clipping rails in the simulation. In other words, weak non-linearity is ignored in the simulation. Note that the desired signal also experiences some level of non-linearity by itself in addition to the distortion caused by the strong interferer. However, such effect also is not accounted for in the simulation. The discrepancy between simulation and hardware-based results is slightly smaller for QPSK because QPSK is more tolerant to non-linearity than 16-QAM.

The effect un-modeled non-linearity can also be observed in the throughput versus compression plot presented in Figure 7.15. The discrepancy between simulation and hardware at lower C is attributed to the fact that the actual compression level is higher than C due to the contribution of weak non-linearity (note that the simulation does not account for weak non-linearity). In other words, there is some level of compression for interference levels that do not exceed V_o. However, such compressions are unaccounted for in the soft-decoder because the threshold in (7.13) is set considering only strong non-linearity. For higher C values, however, the performance of APA-SD is comparable between simulation and hardware. This is because at high C levels, the contribution of weak non-linearity disappears.

Nevertheless, the result clearly shows the benefit of APA-SD over AGC. The result shows that APA-SD allows the receiver to behave indifferent to the presence of the neighboring-channel interferer.

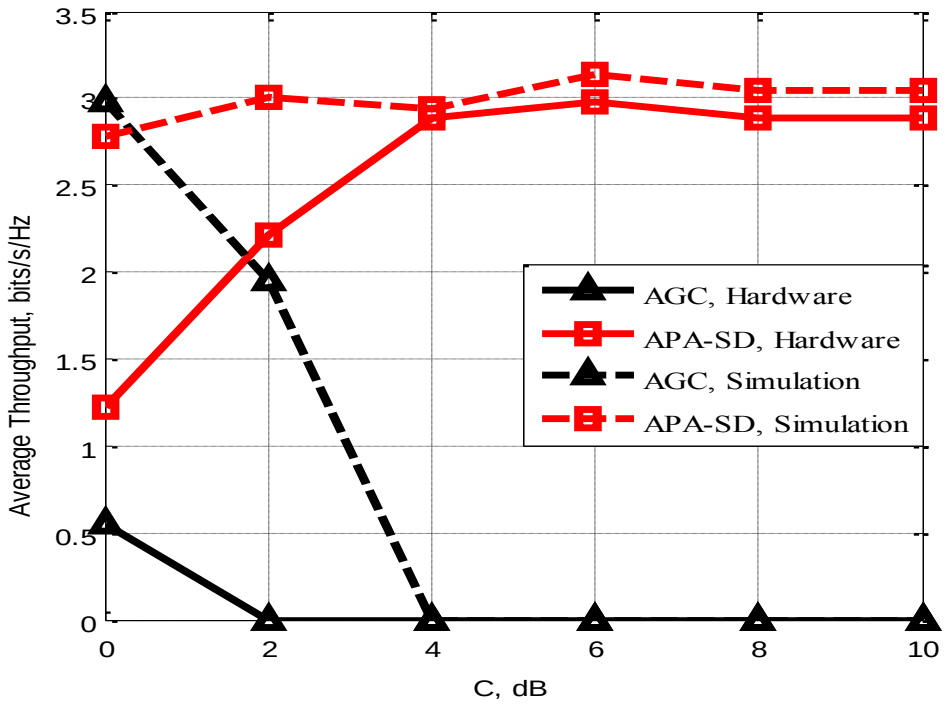

Figure 7.15 Throughput versus compression for 16-QAM signal (SNR = 14 dB)

7.6 Implications for Spectrum Sharing

One major concern against spectrum sharing between commercial wireless services and military radars is that the commercial wireless devices may not be functional due to the interference from the radar signal. The findings in this chapter partly address this concern.

The type of anomaly that is caused by a strong neighboring-channel signal depends on its power level. As it is discussed in this chapter, a moderately powered neighboring-channel interferer can cause some cross-modulation distortion due to the weak non-linearity of the receiver. Stronger signals can also cause significant amplitude-distortion due to strong non-linearity. If the power-

level of the interferer is even higher, it can lead to physical damage on the receiver's circuitry.

The contribution in this paper addresses the first two concerns (distortions caused by strong and weak receiver non-linearities). In doing so, the proposed techniques virtually extend the headroom in the receiver by up to 10 dB (or more). The proposed technique were shown to allow the receiver to be indifferent to the presence of a very strong signal in the received spectrum. If the techniques proposed in this paper are employed, the allowed distance between a radar transmitter and a communication receiver will be limited only by the power handling capability of the receiver, not the non-linearity behavior of the receiver.

Considering a free-space path-loss model, a 10 dB improvement in the receiver's headroom reduces the radius of *receiver*-exclusion-zone around a radar transmitter by more than three times. This benefit can have significant impact on the wireless industry because it expands the geographical area and the market in which shared spectrum can be exploited.

7.7 Chapter Summary

This chapter investigates a scenario in which a weak desired signal is received with a strong radar signal. Traditionally, this scenario is addressed by automatically controlling the gain of the receiver. However, reducing the gain of the receiver may lead to desensitization. This is because the desired signal is pushed into the noise floor while gain is reduced to fit the radar signal into the dynamic range of the receiver.

This paper proposes an architecture that relies on auxiliary paths to address strong signals. The proposed approach is investigated through theoretical analysis, simulation, and hardware-based experiments. From the results of the experiments, the following lessons can be drawn. First; careful investigation on the strong non-linearity characteristics of receivers reveals that a strong neighboring-channel interferer does not cause distortion at every symbol. This is particularly true if the signal has low duty cycle like radar signals. Some symbols of the desired signal are not affected by distortion. Second; this chapter shows that the redundancy in the desired signal (that is provided by coding) can be leveraged to estimate the overall information content of the signal using the information provided by the undistorted symbols. This is not possible in AGC based receiver where the SNR of all symbols, including those that would not be distorted, is indiscriminately reduced. This paper shows the performance of the receiver can be enhanced if gain is not reduced, the signal is allowed to clip, and the redundancy provided by the coding in the desired signal is leveraged to estimate the transmitted information. Third; this chapter shows that the performance of the receiver can further be improved if an auxiliary receive path is employed to sample the envelope of the radar signal, and inform the decoder which bits are distorted and which are not distorted. Compared to non-AGC receiver that rely solely on coding, the use of auxiliary path is shown to provide up to 3 dB improvement in performance if the desired signal is employing multi-level modulation. It is also shown that the auxiliary path has no benefit over non-AGC receiver if the desired signal is employing single-level modulation like QPSK.

The validity of the proposed schemes is verified using hardware-based measurements. Reasonable match is also obtained between simulation and hardware measurement.

Chapter 8

Conclusions

8.1 Summary

This research shows the possibility of improving the performance of poorly-selective receivers using cognitive control over the local-oscillator and sampling frequencies of the RF front-end. CogRF is shown to lower the rate of communication outage from 16% to less than 1% in a poorly-selective receiver. The communication outage performance of CogRF based poorly-selective receiver is actually shown to be slightly better than a highly-selective receiver that does not employ CogRF.

It is pointed out in Chapter 1 that poor-selectivity is going to be a limiting factor in Dynamic-Spectrum-Access (DSA) and mmWave technologies – two of the core technologies that are being vetted to address the current spectrum-deficit problem. The result in this dissertation imply that the reliability of DSA and mmWave radios can be greatly improved by incorporating CogRF to control the frequency-plan of the receiver. Accordingly, the results in this research are expected to help in expediting the adoption of these technologies.

In this research, CogRF refers to a mechanism that intelligently controls only the LO and sampling frequencies of receivers. Chapter 2 shows that CogRF can actually have a broader meaning. Examples of CogRF mechanisms that control various knobs including LNA gain, LNA bias, sampling frequency, Local-Oscillator (LO) frequency, and power amplifier bias, are discussed in Chapter 2. Chapter 2 presents a discussion on the differentiation between traditional cognitive radio systems and CogRF. Chapter 2 shows that CogRF in general can provide various benefits including reduction of power consumption, and increase in Signal-to-Interference-and-Noise-Ration (SINR) of the signal at the output of the Analog-to-Digital-Convertor (ADC) or at the input of the modem.

Chapter 3 presents a theoretical development of a receiver RF front-end modeling technique called Channelized Spectrum Representation (CSR). This model is developed because existing RF front-end models fail to capture the energy re-distribution process in receivers. Chapter 3 shows that mixers, filters, and ADC can be represented linearly using a CSR matrix. These CSR matrix can be used to track the frequency and power-level of signals that are propagating through poorly-selective receivers. The model is extensively used in this research to design a cognitive engine in Chapter 4, and a spectrum sensing mechanism in

Chapter 5. Chapter 3 also presented a new stochastic spectrum occupancy model. This model is used in this research to measure the performance of CogRF.

Chapter 4 presents the formulation and theoretical design of a Cognitive Engine (CE) that controls the LO and sampling frequency of receiver RF front-ends. The CE is implemented using a simple brute-force searching based algorithm. Chapter 4 also presents a theoretical analysis to justify the use of brute-force based CE. The result shows that the CE can find its solutions in millisecond time frame even for receivers whose reception bandwidth is in the order of 100 MHz or more. Simulation-based results presented in Chapter 4 show that the performances of a poorly-selective receiver can be improved by employing the designed CE to control the frequency-plan of the receiver. In other words, the CE allows a poorly-selective receiver to perform similar to a highly-selective receiver without using an actual filter. A 100 step CE is shown to allow a pre-selector-less RF front-end to have a capacity performance within 1 bit of a perfectly-selective RF front-end. A 5 step CE is also shown to improve the rate of outage from 65% to 31% for a poorly selective receiver. This rate lowers just to 54% if the actual selectivity is of the receiver is increased by a factor of 30 without incorporating the CE. It is also shown that the CE can enhance the performance of a highly-selective receiver as well.

Chapter 5 presents a spectrum sensing mechanism that can address the effects of IQ imbalance and aliasing in multi-band spectrum sensing. The developed sensing mechanism is called Robust Serial Multi-band Spectrum Sensing (RS-MSS). RS-MSS is designed to measure the occupancy of the spectrum for the cognitive engine in CogRF. RS-MSS estimates the true state of the spectrum at the receiver input by removing the effects of receiver imperfections from the spectrum sensing data measured at the output of the ADC. To achieve this, RS-MSS uses

the CSR-based modeling to track how energy is re-distributed inside the receiver due to IQ imbalance and aliasing. RS-MSS estimates the state of the spectrum at the receiver input by applying the ADC output to the reverse CSR model of the receiver. A simulation-based evaluation shows that the RS-MSS significantly improves the accuracy of spectrum sensing. It is shown that RS-MSS provides up to 2.5 dB improvement in spectrum accuracy for poorly-selective receivers. In addition, Chapter 5 shows that RS-MSS can also be applied in DSA to improve the opportunity detection performance of secondary users significantly. The results show that RS-MSS improves the opportunity detection performance of a secondary user by up to 74-percentage points – from 26% to about 100%.

Chapter 6 documents the implementation of CogRF. CogRF is implemented on Wireless @ Virginia Tech's PicoRF platform. The details of the software and hardware subsystems of this implementation are presented in this chapter. Chapter 6 also presents the results obtained from four experiments that are carried out using the CogRF implementation. The first experiment measures the CSR matrix of PicoRF. The measurement result show that the CSR matrix of PicoRF exhibits the signatures of IQ imbalance and aliasing. The second experiment measures the practical performance of RS-MSS. The measurement shows that RS-MSS provides up to 20 dB improvement in accuracy compared to a spectrum sensing mechanism that does not correct for the effects of receiver impairments. The second experiment investigates the operation of the cognitive engine that is designed in Chapter 4. The experiment clearly shows that the cognitive engine enables the receiver to "dodge" interference spikes that are caused by the appearance of a strong neighboring-channel signals in the spectrum. The last experiment measures the practical benefits of the CogRF in terms of improving the performance of poorly-selective receivers. The experiment shows that CogRF improves the communication outage performance of poorly-selective receivers.

CogRF is shown to reduce the rate of communication outage from 16% to less than 1% in a pre-selector-less receiver. Under the same spectrum scenario, a selective receiver presented a communication outage performance of about 1.5%. This result confirms that CogRF indeed enables a poorly-selective receiver to behave similar to a highly-selective receiver.

Majority of this research is carried out under the assumption that all the received signals are within the dynamic range of the receiver. Chapter 7 removes this assumption and investigates the characteristics of the receiver in the presence of strong received signals. Particularly, this chapter investigates the scenario in which a weak desired signal reaches the receiver along with a strong radar signal. Traditionally, this scenario is addressed using an Automatic-Gain-Control (AGC) to fit the strong signal into the dynamic range of the receiver. However, this method is not optimal because it sacrifices the precious SNR on the weak desired signal and desensitizes the receiver. Chapter 7 proposes another technique called Auxiliary-Path-Assisted Soft-Decoding (APA-SD). In this method, the strong undesired signal is allowed to clip and distort the desired signal. However, it is shown that only a sub-set of the symbols contained in the desired signal will be distorted. Hence, by leveraging the redundancy on the desired signal, un-distorted symbols can be used to estimate the information content of the desired signal. The auxiliary path "sniffs" the envelope of the strong neighboring-channel signal and informs the decoder which symbols are clipped (or "bad"), and which symbols are not clipped (or "good"). This additional information is shown to improve the estimation performance of the decoder. Hardware and software based experiments are carried out to verify APA-SD. In both experiments, the strong neighboring-channel signal is assumed to be a pulsed-radar signal. According to the results of the hardware-based experiment, APA-SD can expand the dynamic range of the

receiver by more than 8 dB. Hence, this technique allows a receiver to operate in close proximity to a strong radar transmitter both in terms of frequency and space.

8.2 Core Contributions

This research contributes a comprehensive knowledge on cognitive RF front-end control over the frequency plan of a radio receiver. The contributions of this research include; a new receiver modeling technique that allows a tractable design and implementation of cognitive RF front-end control, a theoretical development of the actual control mechanism, and results of the mechanism's practical characterization. The core contributions of this research are further described below.

The first core contribution of this research is that we now know the possibility of linearly modeling an inherently non-linear RF front-end using the channelized spectrum representation (CSR) (see Chapter 3). This model channelizes a signal to equal-sized sub-bands; and it represents the signal by using a vector whose elements denote the power level within each sub-band. CSR is based on existing time-domain models of RF front-end elements; but it leverages the stochastic characteristics of signals in the frequency-domain to convert a rather non-linear time-domain model of an RF front-end element to a matrix that translates the CSR of the input signal to the CSR of the output signal. It is also possible to obtain the CSR model of the overall RF front-end by multiplying the CSR of individual elements in cascade. This research extensively uses this model to efficiently design and implement cognitive RF front-end control over the frequency plan of a receiver. This research also illuminates the fact that CSR can be applied in areas

outside the direct scope of this research. For example, it is shown that the modeling technique has potential application in receiver standardization because it allows quantifying the quality of a receiver using a single number.

The second core contribution of this research is that we now know the possibility of transforming an RF filtering problem to a DSP filtering problem using cognitive control over the local-oscillator and sampling frequencies of receivers. Traditionally, pre-selector is used at the input of a receiver to reject undesired signals such that the amount of distortion they produce on a desired signal is minimized. In poorly selective receivers – where pre-selectors have very wide reception bandwidth, however, undesired neighboring-channel signals can distort the desired signal due to receiver non-idealities such as IQ imbalance and aliasing. In this research, this phenomenon is referred as receiver's energy re-distribution. It is shown that the energy re-distribution is controllable through the local-oscillator and sampling frequencies (see Section 1.3.2). By adjusting the local-oscillator and sampling frequencies, the effects of undesired signals can be positioned away from the desired channel. In such a manner, undistorted desired signal can reach DSP where it can be extracted using highly-selective digital filters. Accordingly, it is pointed that cognitive control over the frequency plan (the local-oscillator and sampling frequencies) of a receiver can be used to obtain selectivity without using highly selective pre-selectors. This dissertation points out that this mechanism can be used to implement reliable radio receivers for dynamic-spectrum-access and mmWave cellular networks where poorly selective pre-selectors are expected.

The third core contribution of this research is a receiver-impairment tolerant spectrum sensing mechanism. It is shown that the CSR of the analog-to-digital converter output is not a correct depiction of the CSR of the spectrum at the

receiver input. This is due to receiver impairments such as IQ imbalance and aliasing. Through this research, we now know that it is possible to jointly reject the effects of IQ imbalance and aliasing by using the inverse of the receiver's CSR matrix. An accurate spectrum sensing result can be obtained by pre-multiplying the CSR of the analog-to-digital-converter's output with the inverse of the receiver's CSR matrix.

The first three contributions apply when the received signal is within the dynamic range of the receiver. The last part of this research developed a mitigation scheme for distortions caused by neighboring-channel signals extending outside the dynamic range of the receiver. Analyzing a receiver scenario in which a weak desired signal is received along with an undesired strong signal, it is shown that the effect of the strong signal can be summarized as a time-varying compression. It is also shown that the compression is a function of strong the signal's envelope. The fourth core contribution of this research is a new technique that uses a soft-decoder along with an auxiliary-receive paths to "sniff" the envelope of the strong neighboring-channel signal and determine the information quality each symbol. Bits at which the instantaneous value of the envelope is high are considered to be "bad" or "liar" bits while those at which the envelope is low are considered to be "good" bits. The decoder is shown to perform better because it can correctly weight the contribution of each bit during the soft-decoding process. It is also shown that this decoding mechanism performs significantly better than traditional automatic-gain-control based system in addressing the effects of strong signals.

Part of this research is published at a peer-reviewed journal [13] and a conference paper [89]. One more manuscript is currently under peer-review [122]. Two other journal paper about the topic discussed in Chapter 7 and Section 3.4 are

under preparation. One provisional patent and one patent disclosure are also filled based on parts of this research.

Appendix A

CSR Model of a Mixer

A quadrature-mixer-pair is considered. Let $f_{LO} = l\Delta + \Delta'$, where where l is a positive integer and Δ' is a fraction of Δ. Then, the relation in (3.5), can be expressed in frequency domain as;

$$V(f) = \left\{W\left(l\Delta + \Delta' + f\right) + \gamma W\left(l\Delta + \Delta' - f\right)\right\} \cdot \left(1 + \left(1+\alpha\right)e^{j\phi}\right) \tag{A.1}$$

where $V(f)$ is the output of the mixer (is a baseband signal), and $V(f) = \Im\{v(t)\}$. The signal $W(f)$ in the input of the mixer (is an RF signal) and $W(f) = \Im\{w(t)\}$. The operator $\Im$ represents Fourier-transform. The term γ is given by,

$$\gamma = \frac{1 - \left(1+\alpha\right)e^{j\phi}}{1 + \left(1+\alpha\right)e^{j\phi}} \tag{A.2}$$

For an RF signal $f_i = i\Delta + \Delta' + \Delta/2$ in (3.2), where i is an integer and Δ' is a fraction of Δ. Because the fractional component (Δ') disappears during down-conversion by f_{LO}, for baseband signal, $f_i = i\Delta + \Delta/2$. Then, $V(f)$ and $W(f)$ in the channel containing f_i are given by,

$$\tilde{V}_i(f) = V(f)\Pi\left(\frac{f - i\Delta - \Delta/2}{\Delta}\right) \tag{A.3}$$

$$\tilde{W}_i(f) = W(f)\Pi\left(\frac{f - i\Delta - \Delta' - \Delta/2}{\Delta}\right) \tag{A.4}$$

Then, dropping the common multiplier in (A.1), and substituting (A.1) into (A.3), we have,

$$\tilde{V}_i(f) = W(l\Delta + \Delta' + f)\Pi\left(\frac{f - i\Delta - \Delta/2}{\Delta}\right) + \gamma W(\Delta l + \Delta' - f)\Pi\left(\frac{f - i\Delta - \Delta/2}{\Delta}\right) \tag{A.5}$$

From (A.4), it can be noted that,

$$\begin{aligned} W(l\Delta + \Delta' + f)\Pi\left(\frac{f - i\Delta - \Delta/2}{\Delta}\right) &= W(f)\Pi\left(\frac{f - (i+l)\Delta - \Delta' - \Delta/2}{\Delta}\right) \\ &= \tilde{W}_{i+l}(f) \end{aligned} \tag{A.6}$$

Similarily,

$$\begin{aligned} W(\Delta l + \Delta' - f)\Pi\left(\frac{f - i\Delta - \Delta/2}{\Delta}\right) &= W(f)\Pi\left(-\frac{f - (i-l)\Delta - \Delta' - \Delta/2}{\Delta}\right) \\ &= W(f)\Pi\left(\frac{f - (i-l)\Delta - \Delta' - \Delta/2}{\Delta}\right) \\ &= \tilde{W}_{i-l}(f) \end{aligned} \tag{A.7}$$

The second equality stems from the even-symmetry of the Π function. Accordingly, from (A.5), (A.6) and (A.7),

$$\tilde{V}_i(f) = \tilde{W}_{l+i}(f) + \gamma \tilde{W}_{-l+i}(f) \tag{A.8}$$

This can be written in time domain as,

$$\tilde{v}_i(t) = \tilde{w}_{l+i}(t) + \gamma \tilde{w}_{-l+i}(t) \tag{A.9}$$

where $\tilde{x}_i(t) = x(t) * \Im^{-1}\left\{\Pi\left(\frac{f - f_i}{\Delta}\right)\right\}$ and $\Im^{-1}$ is inverse-Fourier operator

Assuming $\tilde{w}_{l+i}(t)$ and $\tilde{w}_{l+i}(t)$ are statistically uncorrelated, then, it can be shown that,

$$E\left\{\left|\tilde{v}_i(t)\right|^2\right\} = E\left\{\left|\tilde{w}_{l+i}(t)\right|^2\right\} + |\gamma|^2 E\left\{\left|\tilde{w}_{-l+i}(t)\right|^2\right\} \quad \text{(A.10)}$$

Since $w(t)$ is real valued RF signal, it can also be noted that $E\left\{\left|\tilde{w}_{-l+i}(t)\right|^2\right\} = E\left\{\left|\tilde{w}_{l-i}(t)\right|^2\right\}$. And, using (3.3) and (3.7),

$$p_V[i] = p_W[l+i] + \beta p_W[l-i] \quad \text{(A.11)}$$

where $\beta = |\gamma|^2$, $p_X[i] = E\left\{\left|\tilde{x}_i(t)\right|^2\right\}$ and E is expectation operator.

Appendix B

CSR Model of an ADC

A quadrature-ADC-pair is considered. Let $f_s = s\Delta$, where s is a positive integer. The relation in (3.14) can be expressed in the analog frequency domain as;

$$D(f) = (s\Delta)^2 \sum_{k=-\infty}^{\infty} Z(f - s\Delta k) \tag{B.1}$$

where $D(f)$ is the output of the ADC sampler, and $D(f) = \Im\{d(t)\}$. The input of the ADC is $Z(f)$ and $Z(f) = \Im\{z(t)\}$. The operator $\Im$ represents Fourier-transform.

Let,

$$\tilde{D}_i(f) = D(f)\Pi\left(\frac{f - i\Delta + \Delta/2}{\Delta}\right) \tag{B.2}$$

$$\tilde{Z}_i(f) = Z(f)\Pi\left(\frac{f - i\Delta + \Delta/2}{\Delta}\right) \tag{B.3}$$

Substituting (B.1) into (B.2),

$$\tilde{D}_i(f) = (s\Delta)^2 \sum_{k=-\infty}^{\infty} Z(f - s\Delta k)\Pi\left(\frac{f - i\Delta + \Delta/2}{\Delta}\right) \tag{B.4}$$

and noting that,

$$\begin{aligned} Z(f - s\Delta k)\Pi\left(\frac{f - i\Delta + \Delta/2}{\Delta}\right) &= Z(f)\Pi\left(\frac{f - (i - sk)\Delta + \Delta/2}{\Delta}\right) \\ &= \tilde{Z}_{i-sk}(f) \end{aligned} \tag{B.5}$$

Then,

$$\tilde{D}_i(f) = (s\Delta)^2 \sum_{k=-\infty}^{\infty} \tilde{Z}_{i-sk}(f) \tag{B.6}$$

This can be expressed in time domain as,

$$\tilde{d}_i(t) = (s\Delta)^2 \sum_{k=-\infty}^{\infty} \tilde{z}_{i-sk}(t) \tag{B.7}$$

where $\tilde{x}_i(t) = x(t) * \Im^{-1}\left\{\prod\left(\frac{f - f_i}{\Delta}\right)\right\}$ and $\Im^{-1}$ is inverse-Fourier operator.

Assuming signals in different sub-bands are uncorrelated to each other, it can be shown that,

$$p_d[i] = (s\Delta)^2 \sum_{k=-\infty}^{\infty} p_Z[i - ks] \tag{B.8}$$

where $p_X[i] = E\left\{|\tilde{x}_i(t)|^2\right\}$ and E is expectation operator

Appendix C

Probability Density Function of Average Received Power

According to the free-space path-loss model, the power of the signal received from a transmitter located a distance of r from the receiver is given by,

$$P = \frac{K \cdot p_{TX}}{r^{n_{pl}}} \quad \text{(C. 1)},$$

where K is a constant that is a function of frequency, n_{pl} is the path-loss exponent and p_{TX} is the transmission power.

The maximum separation distance, r_{max}, corresponds to the minimum power of a detectable signal. Hence, it can be shown that,

$$p = \frac{p_m}{\sigma^{n_{pl}}} \quad \text{(C. 2)},$$

where $\sigma = r/r_{max}$. A transmitter can be located anywhere around the receiver except within radius of $r_m = \sigma_m r_{max}$. Assuming that the received power equals p_{TX} when $r = r_m$, it can be shown that,

$$p_{TX} = \frac{p_m}{\sigma_m^{n_{pl}}} \quad \text{(C. 3)}.$$

The probability that a transmitter is located within radius of r from a receiver which has detected the transmitted signal is given by $(\pi r^2 - \pi r_m^2)/(\pi r_{max}^2 - \pi r_m^2)$. This is assuming that the distance between the transmitter and the receiver is uniformly distributed between r_m and r_{max}.Therefore, the cumulative distribution function of σ can be expressed as,

$$F_\rho(\rho) = \begin{cases} 0, & \sigma < \sigma_m \\ \frac{\sigma^2 - \sigma_m^2}{1 - \sigma_m^2}, & \sigma_m \le \sigma \le 1 \\ 1, & \sigma > 1 \end{cases} \qquad \text{(C.4).}$$

From (C.2) it can be shown that the cumulative distribution function of p is given by $F_p(p) = 1 - F_\rho\left(\sqrt{p_m/p}\right)$. Substituting in (C.4) it can be shown that,

$$F_p(p) = \begin{cases} 0\,, & p < p_m \\ \frac{1 - \left(\frac{p_m}{p}\right)^{2/n_{pl}}}{1 - \left(\frac{p_m}{p_{TX}}\right)^{2/n_{pl}}}\,, & p_m \le p \le p_{TX} \\ 1\,, & p > p_{TX} \end{cases} \qquad \text{(C.5).}$$

Finally, the probability density function of p which is obtained by differentiating F_p in (C.5) is given by,

$$f_p(p) = \begin{cases} \left(\frac{p_m^{2/n_{pl}}/n_{pl}}{1 - \left(\frac{p_m}{p_{TX}}\right)^{2/n_{pl}}} \right) \frac{2}{p^{1 + \frac{2}{n_{pl}}}}\,, & p_m \le p \le p_{TX} \\ 0\,, & otherwise \end{cases} \qquad \text{(C.6).}$$

Appendix D

Probability Density Function of CSR Measurement Error

Let the signal contained in a channel at the output of the ADC be given by

$$s_n = r_{i,n} + jr_{q,n}\,, \tag{D.1}$$

where $r_{i,n}$ and $r_{q,n}$ are the real and imaginary components obtained in the n^{th} periodogram, respectively. Assume that they are uncorrelated to each other, $E\{r_{i,n}\} = 0$, and $E\{r_{i,n}^2\} = p_t/2$, where p_t is the true power in the channel. Similarly, we assume that $E\{r_{q,n}\} = 0$ and $E\{r_{q,n}^2\} = p_t/2$. In addition, assume the higher order moments of $r_{i,n}$ and $r_{q,n}$ are equal to zero. In addition, note that $E\{|s|^2\} = p_t$.

The objective of CSR measurement is to estimate for $\hat{p}_t$ given by,

$$\hat{p}_t = \frac{1}{N_p}\sum_{i=1}^{N_p}|s_n|^2 \tag{D.2}$$

It can be shown that $E\{\hat{p}_t\} = p_t$ and $VAR\{\hat{p}_t\} = p_t^2/(2N_p)$, where *VAR* is variance operator. Because $|s_n|$ has finite first- and second-order moments, the central-limit theorem can be applied. Hence, we can approximate the distribution of $\hat{p}_t$ by the normal distribution. Therefore, the measurement error (residue), which is given

by $e = p_t - \hat{p}_t$, is also normally distributed with zero mean and variance equal to $p_t^2 / \left(2N_p\right)$.

Appendix E

Types of Receiver Non-Linearities

There are two types of non-linearity distortions in receiver RF front-end as shown in Figure D.1. These are inherent non-linearity and undesired non-linearity. Undesired non-linearity can further be classified to weak non-linearity and strong non-linearity.

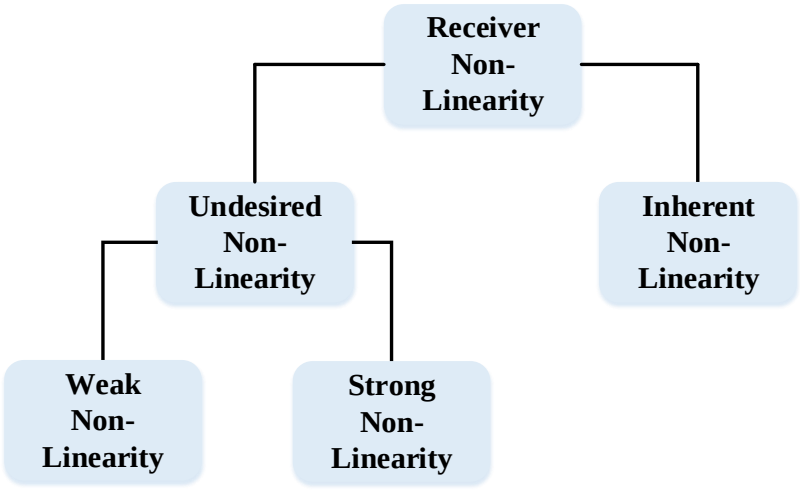

Figure E.1 Classification of receiver non-linearity

Inherent non-linearity refers to the desired non-linear operation in receivers. For example, mixers have to be non-linear in order to down-convert the received signal. Similarly, the sampling process in the ADC has to be non-linear to discretize the analog signal. However, inherent non-linearity may also have undesirable side-effects. Neighboring-channel signals at the input of an inherently

non-linear element may map to the same channel at the output. The set of frequencies at the input, which map to the same frequency at the output of the element, are referred as images. When a signal passes through a mixer and an ADC, it is potentially corrupted by undesired image signals [12, 45].

Weak non-linearity is the most widely studied type of RF front-end non-linearity [109]. Weak non-linearity distortion is a small signal characteristic. The effects of weak non-linearity include odd and even order intermodulation distortions. Intermodulation distortions occur when two strong signals produce an intermodulation product at frequency band of the desired signal. The other type of weak non-linearity distortion occurs when a weak desired signal arrives at the input of the receiver along with an undesired strong signal. The envelope of the strong signal distorts the desired signal by modulating the gain of the receiver RF front-end[12]. This effect is called cross-modulation. Weak non-linearity is typically quantified using parameters such as third order input referred intercept point (IIP3) and second order input referred intercept point (IIP2)[12],[45].

The other type of undesired non-linearity is strong non-linearity or clipping. It is a large signal characteristic which is determined by the voltage and current supply of the elements of the RF front-end. For this reason, strong non-linearity is generally independent of the small signal attributes of the RF front-end. Strong non-linearity can be quantified using the input referred saturation power (P_{sat}) of the RF front-end element. The term P_{sat} represents the maximum power of a continuous wave input signal that passes through the element without clipping. Typically, the effect of strong non-linearity is observed when an undesired strong signal, with power level greater than P_{sat}, reaches the input accompanying a desired weak signal. Due to strong non-linearity, the envelope of the strong

undesired signal distorts the desired signal by modulating the gain of the strongly non-linear element.

Appendix F

Copyright Permissions

SPRINGER LICENSE
TERMS AND CONDITIONS

Oct 13, 2014

This is a License Agreement between Eyosias Yoseph Imana ("You") and Springer ("Springer") provided by Copyright Clearance Center ("CCC"). The license consists of your order details, the terms and conditions provided by Springer, and the payment terms and conditions.

All payments must be made in full to CCC. For payment instructions, please see information listed at the bottom of this form.

License Number	3480030053115
License date	Oct 01, 2014
Licensed content publisher	Springer
Licensed content publication	Analog Integrated Circuits and Signal Processing
Licensed content title	Relaxing pre-selector filter selectivity requirements using cognitive RF front-end control
Licensed content author	Eyosias Yoseph Imana
Licensed content date	Jan 1, 2013
Volume number	78
Issue number	3
Type of Use	Thesis/Dissertation
Portion	Figures
Author of this Springer article	Yes and you are the sole author of the new work
Order reference number	None
Original figure numbers	Fig. 3, Fig. 4, Fig. 5
Title of your thesis /	Cognitive RF Front-end Control

dissertation	
Expected completion date	Oct 2014
Estimated size(pages)	200
Total	0.00 USD

References

[1] CISCO, "Cisco Visual Networking Index: Global Mobile Data Traffic Forecast Update, 2013–2018," 2013.

[2] FCC, "Mobile broadband: The benefits of additional spectrum," 2010.

[3] S. Haykin, "Cognitive radio: brain-empowered wireless communications," *Selected Areas in Communications, IEEE Journal on*, vol. 23, pp. 201-220, 2005.

[4] J. Mitola, "Cognitive radio for flexible mobile multimedia communications," in *Mobile Multimedia Communications, 1999. (MoMuC '99) 1999 IEEE International Workshop on*, 1999, pp. 3-10.

[5] S. W. Ellingson, "Spectral occupancy at VHF: implications for frequency-agile cognitive radios," in *Vehicular Technology Conference, 2005. VTC-2005-Fall. 2005 IEEE 62nd*, 2005, pp. 1379-1382.

[6] M. A. McHenry, P. A. Tenhula, D. McCloskey, D. A. Roberson, and C. S. Hood, "Chicago spectrum occupancy measurements & analysis and a long-term studies proposal," presented at the Proceedings of the first international workshop on Technology and policy for accessing spectrum, Boston, Massachusetts, 2006.

[7] M. H. Islam, C. L. Koh, O. Ser Wah, Q. Xianming, Y. Y. Lai, W. Cavin, *et al.*, "Spectrum Survey in Singapore: Occupancy Measurements and Analyses," in *Cognitive Radio Oriented Wireless Networks and Communications, 2008. CrownCom 2008. 3rd International Conference on*, 2008, pp. 1-7.

[8] T. S. Rappaport, Q. Yijun, J. I. Tamir, J. N. Murdock, and E. Ben-Dor, "Cellular broadband millimeter wave propagation and angle of arrival for adaptive beam steering systems (invited paper)," in *Radio and Wireless Symposium (RWS), 2012 IEEE*, 2012, pp. 151-154.

[9] T. S. Rappaport, S. Shu, R. Mayzus, Z. Hang, Y. Azar, K. Wang, *et al.*, "Millimeter Wave Mobile Communications for 5G Cellular: It Will Work!," *Access, IEEE*, vol. 1, pp. 335-349, 2013.

[10] V. T. Nguyen, F. Villain, and Y. Le Guillou, "Cognitive Radio RF: Overview and Challenges," *VLSI Design*, vol. 2012, p. 13, 2012.

[11] D. M. Pozar, *Microwave and RF design of wireless systems*: John Wiley & Sons, Inc., 2001.

[12] B. Razavi, *RF Microelectronics, Second Edition*: Prentice Hall, 2011.

[13] E. Imana, T. Yang, and J. Reed, "Relaxing pre-selector filter selectivity requirements using cognitive RF front-end control," *Analog Integrated Circuits and Signal Processing*, vol. 78, pp. 705-716, 2014/03/01 2014.

[14] P. B. Kenington, *RF and baseband techniques for software defined radio*. Boston: Atech House, 2005.

[15] Qualcomm. (2013, Qualcomm RF360 front end solution. Available: https://www.qualcomm.com/media/documents/files/qualcomm-rf360-front-end-solution-product-brief.pdf

[16] J. Uher and W. J. R. Hoefer, "Tunable microwave and millimeter-wave band-pass filters," *IEEE Transactions on Microwave Theory and Techniques,* vol. 39, pp. 643-653, 1991.

[17] G. M. Rebeiz, K. Entesari, I. C. Reines, S. J. Park, M. A. El-Tanani, and A. R. Brown, "RF MEMS Tunable Filters," *IEEE Microwave Magazine,* pp. 55-72, 2009.

[18] A. Coon, "SAW filters and competitive technologies: a comparative review," *Proceedings of Ultrasonics Symposium, 1991,* pp. 155-160, 1991.

[19] J. Bouchaud, R. Sorrentino, B. Knoblich, H. A. C. Tilmans, and F. Coccetti, "Industry roadmap for RF MEMS, ed. Stephan Lucyszyn," in *Advanced RF MEMS*, ed: Cambridge university press, 2010, pp. 359-403.

[20] M. K. Roy and J. Richter, "Tunable Ferroelectric Filters for Software Defined Tactical Radios," in *15th ieee international symposium on the Applications of ferroelectrics 2006,* 2006.

[21] A. Tombak, J.-P. Maria, F. T. Ayguavives, Z. Jin, G. T. Stauf, A. I. Kingon, *et al.*, "Voltage-controlled RF filters employing thin-film barium-strontium-titanate tunable capacitors," *IEEE transactions on Microwave Theory and Techniques,* vol. 51, pp. 462-467, 2003.

[22] M.-T. Nguyen, W. D. Yan, and E. Horne, "Broadband tunable filters using high Q passive tunable ICs," in *2008 IEEE MTT-S International Microwave Symposium Digest*, Atlanta, 2008.

[23] A. R. Brown and G. M. Rebeiz, "A Varactor Tuned RF Filter," *IEEE Transactions on Microwave Theory and Techniques,* vol. 48, pp. 1157-1160, 2000.

[24] M. A. El-Tanani and G. M. Rebeiz, "High-Performance 1.5–2.5-GHz RF-MEMS Tunable Filters for Wireless Applications," *IEEE Transactions on Microwave Theory and Techniques,* vol. 58, pp. 1629-1637, 2010.

[25] T.-C. Lee, S.-J. Cheon, and J.-Y. Park, "Ultracompact UHF Tunable Filter Embedded into Multilayered Organic Packaging Substrate," *IEEE Transactions on Components, Packaging and Manufacturing Technology,* 2011.

[26] M. A. El-Tanani and G. M. Rebeiz, "A Two-Pole Two-Zero Tunable Filter With Improved Linearity," *IEEE Transactions on MIcrowave Theory and Techniques,* vol. 57, pp. 830-839, 2009.

[27] X. Liu, L. P. B. Katehi, W. J. Chappell, and D. Peroulis, "High-Q Tunable Microwave Cavity Resonators and Filters Using SOI-Based RF MEMS Tuners," *Journal of Microelectromechanical Systems,* vol. 19, pp. 774-784, 2010.

[28] S.-J. Park, I. Reines, and G. Rebeiz, "High-Q RF-MEMS tunable evanescent-mode cavity filter," in *IEEE MTT-S Microwave Symposium Digest, MTT'09*, 2009, pp. 1145-1148.

[29] T. Nishino, Y. Kitsukawa, M. Hangai, S.-s. Lee, S.-n. Soda, M. Miyazaki, *et al.*, "Tunable MEMS hybrid coupler and L-band tunable filter," in *IEEE MTT-S International Microwave Symposium Digest, 2009. MTT '09,* 2009.

[30] A. Malczewski, B. Pillans, F. Morris, and R. Newstrom, "A family of MEMS tunable filters for advanced RF applications," in *IEEE MTT-S International Microwave Symposium Digest (MTT), 2011* 2011.
[31] X. Y. Zhang and Q. Xue, "High-Selectivity Tunable Bandpass Filters With Harmonic Suppression," *IEEE Transactions on Microwave Theory and Techniques,* vol. 58, pp. 964-969, 2010.
[32] P. Pawelczak, K. Nolan, L. Doyle, S. W. Oh, and D. Cabric, "Cognitive radio: Ten years of experimentation and development," *IEEE Communications Magazine,* vol. 49, pp. 90-100, 2011.
[33] P. F. Marshall, "Extending the Reach of Cognitive Radio," *Proceedings of the IEEE* vol. 97, pp. 612-625, 2009.
[34] P. F. Marshall, "Cognitive radio as a mechanism to manage front-end linearity and dynamic range," *Communications Magazine, IEEE,* vol. 7, pp. 81-87, 2009.
[35] D. S. Yu, C. F. Cheng, K. T. Chan, A. Chin, S. P. McAlister, C. Zhu, *et al.*, "Narrow-band band-pass filters on silicon substrates at 30 GHz," in *Microwave Symposium Digest, 2004 IEEE MTT-S International*, 2004, pp. 1467-1470 Vol.3.
[36] L. Chien-Chih, H. Chao-Zong, and C. Chu-Yu, "Compact and highly selective millimeter-wave meandered bandpass filter using 0.18-µm CMOS technology," in *Microwave Conference Proceedings (APMC), 2011 Asia-Pacific*, 2011, pp. 49-52.
[37] K. Kupfmuller and E. Nachrichtentechnik. (1928, September, 2014). On the dynamics of automatic gain controllers. *English translation*. Available: http://ict.open.ac.uk/classics/2.pdf
[38] A. Bezoonijen, R. Mahmoudi, and A. Roermund, *Adaptive RF front-ends for hand-held applications*: Springer, 2011.
[39] D. Banerjee, S. Sen, A. Banerjee, and A. Chatterjee, "Low-power adaptive RF system design using real-time fuzzy noise-distortion control," presented at the Proceedings of the 2012 ACM/IEEE international symposium on Low power electronics and design, Redondo Beach, California, USA, 2012.
[40] R. Senguttuvan, S. Sen, and A. Chatterjee, "Multidimensional Adaptive Power Management for Low-Power Operation of Wireless Devices," *Circuits and Systems II: Express Briefs, IEEE Transactions on,* vol. 55, pp. 867-871, 2008.
[41] S. Sen, R. Senguttuvan, and A. Chatterjee, "Environment-Adaptive Concurrent Companding and Bias Control for Efficient Power-Amplifier Operation," *Circuits and Systems I: Regular Papers, IEEE Transactions on,* vol. 58, pp. 607-618, 2011.
[42] S. Ciccarelli, "Dynamically programmable receiver," USA Patent, 2002.
[43] A. Tasic, L. Su-Tarn, W. A. Serdijn, and J. R. Long, "Design of Adaptive Multimode RF Front-End Circuits," *Solid-State Circuits, IEEE Journal of,* vol. 42, pp. 313-322, 2007.
[44] G. Hueber, J. Zipper, R. Stuhlberger, and A. Holm, "An adaptive multi-mode RF front-end for cellular terminals," in *Radio Frequency Integrated Circuits Symposium, 2008. RFIC 2008. IEEE,* 2008, pp. 25-28.

[45] M. D. Pozar, *Microwave and RF design of wireless systems*. Newyork: John Wiley & SONS, INC., 2001.
[46] S. C. Cripps, *RF Power Amplifiers for Wireless Communications, Second Edition* Artech House Microwave Library, 2006.
[47] J. Tao and W. Yiyan, "An Overview: Peak-to-Average Power Ratio Reduction Techniques for OFDM Signals," *Broadcasting, IEEE Transactions on*, vol. 54, pp. 257-268, 2008.
[48] L. Ding, G. T. Zhou, D. R. Morgan, M. Zhengxiang, J. S. Kenney, K. Jaehyeong, *et al.*, "A robust digital baseband predistorter constructed using memory polynomials," *Communications, IEEE Transactions on*, vol. 52, pp. 159-165, 2004.
[49] J. Mitola, "Cognitive Radio: An integrated agent architecture for software defined radio," Doctor of Technology Dissertation, Teleinformatics, Royal Institute of Technology (KTH), 2000.
[50] T. W. Rondeau, "Application of artificial intelligence to wireless communication," Ph.D. Dissertation, Electrical and Computer Engineering Department, Virginia Tech.
[51] R. T. Newman, "Multiple objective fitness functions for cognitive radio adaptation," Dissertation, Electrical and computer engineering, University of Kansas, 2008.
[52] A. He, J. Gaeddert, K. K. Bae, T. R. Newman, J. H. Reed, L. Morales, *et al.*, "Development of a case-based reasoning cognitive engine for IEEE 802.22 WRAN applications," *SIGMOBILE Mob. Comput. Commun. Rev.*, vol. 13, pp. 37-48, 2009.
[53] H. I. Volos, "Cognitive radio engine design for link adaptation," Ph.D. disseration at Electrical and Computer Engineering Deparment, Virginia Polytechnic Institute and State University, Blacksburg2010.
[54] T. H. Lee, *The Design of CMOS Radio-Frequency Integrated Circuits*, 2nd ed.: Cambridge University Press, 2004.
[55] T. H. Lee, "From Oxymoron to Mainstream: The Evolution and Future of RF CMOS," in *IEEE International Workshop on Radio-Frequency Integration Technology, 2007.*, Singapore, 2007.
[56] V. Giannini, J. Craninckx, S. D'Amico, and A. Baschirotto, "Flexible Baseband Analog Circuits for Software-Defined Radio Front-Ends," *IEEE Journal of Solid-State Circuits*, vol. 42, pp. 1501-1512, 2007.
[57] J. Craninckx, M. Liu, D. Hauspie, V. Giannini, T. Kim, J. Lee, *et al.*, "A Fully Reconfigurable Software-Defined Radio Transceiver in 0.13μm CMOS," in *IEEE International Solid-State Circuits Conference Digest of Technical Papers, pp.346-607*, 2007.
[58] M. Ingels, C. Soens, J. Craninckx, V. Giannini, T. Kim, B. Debaillie, *et al.*, "A CMOS 100 MHz to 6 GHz software defined radio analog front-end with integrated pre-power amplifier," in *in Proc. 33rd European Solid State Circuits Conference, pp.436-439*, 2007.

[59] G. Cafaro, T. Gradishar, J. Heck, S. Machan, G. Nagaraj, S. Olson, *et al.*, "A 100 MHz 2.5 GHz Direct Conversion CMOS Transceiver for SDR Applications," in *Radio Frequency Integrated Circuits (RFIC) Symposium, 2007 IEEE*, 2007, pp. 189-192.

[60] "LMS6002D configurable broadband transceiver IC," ed: Lime Microsystems, 2011.

[61] A. D. Inc. (Sept.). *AD9361 datasheet and product info| 2 x 2 RF Agile Transceiver* Available: http://www.analog.com/en/rfif-components/rfif-transceivers/ad9361/products/product.html

[63] S. M. Dudley, W. C. Headley, M. Lichtman, E. Y. Imana, M. Xiaofu, M. Abdelbar, *et al.*, "Practical Issues for Spectrum Management With Cognitive Radios," *Proceedings of the IEEE*, vol. 102, pp. 242-264, 2014.

[64] V. Gianni and J. Craninckx, *Baseband analog circuits for software defined radio*. Dordrecht, The Netherlands: Springer, 2008.

[65] (2011). *Board Agency Annoucement, Radio Frequency-Field Programmable Gate Arrays (RF-FPGA) [DARPA-BAA-12-13]*.

[66] A. Fukuda, H. Okazaki, and S. Narahashi, "A novel reconfigurable quad-band power amplifier with reconfigurable biasing network and LTCC substrates," in *Microwave Symposium Digest, 2008 IEEE MTT-S International*, 2008, pp. 867-870.

[67] K. Unha, K. Kyutae, K. Junghyun, and K. Youngwoo, "A multi-band reconfigurable power amplifier for UMTS handset applications," in *Radio Frequency Integrated Circuits Symposium (RFIC), 2010 IEEE*, 2010, pp. 175-178.

[68] K. S. Chen, N. T. Hsu, K. C. Lu, T. S. Horng, and J. M. Wu, "A variable gain low-noise amplifier with noise and nonlinearity cancellation for DVB applications," in *Microwave Conference, 2009. APMC 2009. Asia Pacific*, 2009, pp. 1144-1147.

[69] M. Perin, O. Aymard, S. Darfeuille, P. Gamand, and C. Berland, "Low-power digitally-controlled variable gain LNA with high isolation for sub-GHz ISM bands," in *Electronics, Circuits, and Systems, 2009. ICECS 2009. 16th IEEE International Conference on*, 2009, pp. 623-626.

[70] S.-t. Li, J.-c. Li, J.-z. Wang, and Q. Yang, "Design of 900∼2250MHz broad-band differential LNA with variable gain," in *Computer Application and System Modeling (ICCASM), 2010 International Conference on*, 2010, pp. V12-581-V12-587.

[71] H. Zhang, Z. Li, and Z. Wang, "A wideband variable gain differential CMOS LNA for multi-standard wireless LAN," in *Microwave and Millimeter Wave Technology, 2008. ICMMT 2008. International Conference on*, 2008, pp. 1334-1337.

[72] J. H. Reed, *Software Radio: A Modern Approach to Radio Engineering*. Upper Saddle River, New Jersey: Prentice Hall, 2002.

[73] S. M. S. Hasan, "New concepts in front-end design for receivers with large, multiband tuning ranges," Ph.D., Electrical and Computer Engineering, Virginia Tech, 2009.
[74] P. G. M. Baltus, "Minimum power design of RF Front-ends," Ph.D., Technishe University, 2004.
[75] J. G. Proakis and D. G. Manalakis, *Digital signal processing: Principles, algorithms, and applications*. Delhi, India: Dorling Kindersley, 2007.
[76] J. G. Proakis and M. Salehi, *Digital communication*: McGraw-Hill, 2008.
[77] J. C. Pedro and N. B. Carvalho, *Intermodulation distortion in microwave and wireless circuits*: Artech house, Inc., 2003.
[78] J. Crols and M. S. J. Steyaert, "Low-IF topologies for high-performance analog front ends of fully integrated receivers," *Circuits and Systems II: Analog and Digital Signal Processing, IEEE Transactions on*, vol. 45, pp. 269-282, 1998.
[79] M. Mailand, R. Richter, and H.-J. Jentschel, "IQ-imbalance and its compensation for non-ideal analog receivers comprising frequency-selective components," *Advanced Radio Science*, vol. 5, pp. 189-195, 2006.
[80] D. Scerhneid, "GPS-interference controversy comes to a boil," *Spectrum, IEEE*, vol. 49, pp. 13-14, 2012.
[81] PCAST. (2012, Realizing the full potential of government-held spectrum to spur economic growth.
[82] A. V. Padaki and J. H. Reed, "Impact of intermodulation distortion on spectrum preclusion for DSA: A new figure of merit," in *Dynamic Spectrum Access Networks (DYSPAN), 2014 IEEE International Symposium on*, 2014, pp. 358-361.
[83] M. Lopez-Benitez and F. Casadevall, "Discrete-time spectrum occupancy model based on Markov Chain and duty cycle models," in *in the proceedings of 2011 IEEE Dynamic Spectrum Access Networks (DySPAN) Symposium*, 2011.
[84] A. Gorcin, H. Celebi, K. A. Qaraqe, and H. Arslan, "An autoregressive approach for spectrum occupancy modeling and prediction based on synchronous measurements," in *in the proceedings of 2011 IEEE 22nd International Symposium on Personal Indoor and Mobile Radio Communications*, 2011.
[85] C. Ghosh, S. Pagadarai, D. Agrawal, and A. Wyglinski, "A framework for statistical wireless spectrum occupancy modeling," *Wireless Communications, IEEE Transactions on*, vol. 9, pp. 38-44, 2010.
[86] T. S. Rappaport, *Wireless Communications; Principles and Practice*: Prentice Hall, 1996.
[87] L. Zaninetti and M. Ferraro, "On the truncated Pareto distribution with applications," *Central European Journal of Physics*, vol. 6, pp. 1-6, 2008.
[88] S. Ross, *First Course in Probability, 8th edition*: Prentice Hall, 2009.
[89] E. Imana and J. Reed, "Cognitive RF front-end control," in *2012's SDR Forum*, Washington DC, January, 2013.
[90] T. Zhi and G. B. Giannakis, "Compressed Sensing for Wideband Cognitive Radios," in *Acoustics, Speech and Signal Processing, 2007. ICASSP 2007. IEEE International Conference on*, 2007, pp. IV-1357-IV-1360.

[91] Q. Zhi, C. Shuguang, A. H. Sayed, and H. V. Poor, "Optimal Multiband Joint Detection for Spectrum Sensing in Cognitive Radio Networks," *Signal Processing, IEEE Transactions on*, vol. 57, pp. 1128-1140, 2009.

[92] J. Verlant-Chenet, J. Renard, J. M. Dricot, P. De Doncker, and F. Horlin, "Sensitivity of Spectrum Sensing Techniques to RF Impairments," in *Vehicular Technology Conference (VTC 2010-Spring), 2010 IEEE 71st*, 2010, pp. 1-5.

[93] E. Rebeiz, A. S. H. Ghadam, M. Valkama, and D. Cabric, "Suppressing RF front-end nonlinearities in wideband spectrum sensing," in *Cognitive Radio Oriented Wireless Networks (CROWNCOM), 2013 8th International Conference on*, 2013, pp. 87-92.

[94] Y. L. Polo, W. Ying, A. Pandharipande, and G. Leus, "Compressive wide-band spectrum sensing," in *Acoustics, Speech and Signal Processing, 2009. ICASSP 2009. IEEE International Conference on*, 2009, pp. 2337-2340.

[95] P. Paysarvi-Hoseini and N. C. Beaulieu, "Optimal Wideband Spectrum Sensing Framework for Cognitive Radio Systems," *Signal Processing, IEEE Transactions on*, vol. 59, pp. 1170-1182, 2011.

[96] S. Hongjian, A. Nallanathan, W. Cheng-Xiang, and C. Yunfei, "Wideband spectrum sensing for cognitive radio networks: a survey," *Wireless Communications, IEEE*, vol. 20, 2013.

[97] G. Hattab and M. Ibnkahla, "Multiband Spectrum Access: Great Promises for Future Cognitive Radio Networks," *Proceedings of the IEEE*, vol. 102, pp. 282-306, 2014.

[98] A. Gokceoglu, S. Dikmese, M. Valkama, and M. Renfors, "Enhanced energy detection for multi-band spectrum sensing under RF imperfections," in *Cognitive Radio Oriented Wireless Networks (CROWNCOM), 2013 8th International Conference on*, 2013, pp. 55-60.

[99] B. Farhang-Boroujeny, "Filter Bank Spectrum Sensing for Cognitive Radios," *Signal Processing, IEEE Transactions on*, vol. 56, pp. 1801-1811, 2008.

[100] M. Grimm, M. Allen, J. Marttila, M. Valkama, and R. Thoma, "Joint Mitigation of Nonlinear RF and Baseband Distortions in Wideband Direct-Conversion Receivers," *Microwave Theory and Techniques, IEEE Transactions on*, vol. 62, pp. 166-182, 2014.

[101] S. C. Narula and J. F. Wellington, "Prediction, Linear Regression and the Minimum Sum of Relative Errors," *Technometrics*, vol. 19, pp. 185-190, 1977/05/01 1977.

[102] V. Franc, V. Hlaváč, and M. Navara, "Sequential Coordinate-Wise Algorithm for the Non-negative Least Squares Problem," in *Computer Analysis of Images and Patterns*. vol. 3691, A. Gagalowicz and W. Philips, Eds., ed: Springer Berlin Heidelberg, 2005, pp. 407-414.

[103] D. Chen and R. J. Plemmons, "Nonnegativity constraints in numerical analysis," in *Symposium on the Birth of Numerical Analysis*, 2009, pp. 109-140.

[104] T. C. I. Clancy, "Dynamic specrum access in cognitive radio, Ph.D. Dissertation," University of Maryland, College Park2006.

[105] K. A. Said, "PicoRF: A PC-based SDR Platform using a High Performance PCIe Plug-in Card Extension.," Master's Thesis, Electrical and Computer Engineering, Virginia Tech, 2012.
[106] I. Foundation. *SCPI*. Available: http://www.ivifoundation.org/scpi/default.aspx
[107] P. Express, "PCI Express Base Specification Revisions 3.0," 2010.
[108] J. Cobert, A. Rubini, and G. Kroah-Hartman, *Linux device drivers*, 3rd ed.: O'Reilley, 2005.
[109] H. Zhang and E. Sánchez-Sinencio, "Linearization Techniques for CMOS Low Noise Amplifiers: A Tutorial," *IEEE Transactions on Circuits and Systems I*, vol. 58, pp. 22-36, 2011.
[110] V. Aparin, G. Brown, and L. E. Larson, "Linearization of CMOS LNA's via optimum gate biasing," in *Circuits and Systems, 2004. ISCAS '04. Proceedings of the 2004 International Symposium on , vol.4, ,* 2004.
[111] Y. Ding and R. Harjani, "A +18 dBm IIP3 LNA in 0.35 μm CMOS," in *Solid-State Circuits Conference, 2001. Digest of Technical Papers. ISSCC. 2001 IEEE International , pp.162-163*, 2001.
[112] H. Zhang, X. Fan, and E. S. Sinencio, "A Low-Power, Linearized, Ultra-Wideband LNA Design Technique," *IEEE Journal of Solid-State Circuits*, vol. 44, pp. 320-330, 2009.
[113] W.-H. Chen, G. Liu, B. Zdravko, and A. M. Niknejad, "A Highly Linear Broadband CMOS LNA Employing Noise and Distortion Cancellation," *IEEE Journal of Solid-State Circuits*, vol. 43, pp. 1164-1176, 2008.
[114] P. Marshall. (2008, April 23). What is beyond dynamic spectrum access for cognitive radio. Available: http://ntrg.cs.tcd.ie/en/TCD_VT_Course_Cognitive_Radios_and_Networks/Week%2013/Marshall%20VT-TCD%20CourseV2.pdf
[115] "3.5 GHz spectrum access system workshop," ed: FCC, January 14, 2014.
[116] J. H. Reed, T. C. I. Clancy, C. Dietrich, R. Nealy, M. Fowler, M. Mearns, *et al.* (2014, Measurement result for radar and wireless system coexistence at 3.5 GHz. Available: http://wireless.fcc.gov/workshops/sas_01-14-2014/end/Reed-VA_TECH.pdf
[117] R. Dinis and P. Silva, "Iterative Detection of Multicode DS-CDMA Signals with Strongly Nonlinear Transmitters," in *in the Proceedings of 18th Internatonal Conference on Computer Communications and Networks*, 2009.
[118] H. Nikopour, A. K. Khandani, and S. H. Jamali, "Turbo-Coded OFDM Transmission Over a Nonlinear Channel," *IEEE Transactions on Vehicular Technology*, vol. 54, pp. 1361-1371, 2005.
[119] J. Cha, J. Yi, J. Kim, and B. Kim, "Optimum design of a predistortion RF power amplifier for multicarrier WCDMA applications," *IEEE Transactions on Microwave Theory and Techniques*, vol. 52, pp. 655-663, 2004.
[120] E. research. (2014, October 10). *Ettus Research-Product Detail: USRP1*. Available: https://www.ettus.com/product/details/USRPPKG

[121] M. M. U. Gul, L. Sungeun, and M. Xiaoli, "Robust synchronization for OFDM employing Zadoff-Chu sequence," in *Information Sciences and Systems (CISS), 2012 46th Annual Conference on*, 2012, pp. 1-6.
[122] E. Imana, T. Yang, and J. Reed, "Mitigating the effect of receiver impariments in multi-band spectrum sensing," *submitted to IEEE Transactions on Microwave Theory and Techniques,* 2014.